

USER's Manual

written by Valeri Petkov

E-mail: petkov@phy.cmich.edu
url: <http://www.phy.cmich.edu/people/petkov/>

Document created: February 2011

Disclaimer:

RAD is distributed as is: i.e. without any warranty, assumed or implied. The entire risk as to the quality and performance of the program is with the User. *The use of RAD for any commercial purpose is prohibited.*

Acknowledging RAD:

Any publication and/or presentation of results obtained using RAD should make clear that RAD has been used and contain the following reference:

V. Petkov, “RAD, a program for analysis of X-ray diffraction data from amorphous materials for personal computers” *J. Appl. Crystallogr.* **22** (1989) 387-89.

(a copy of the paper is attached for user’s convenience).

Installing RAD:

WINDOWS XP/VISTA/7 Users:

Download & Run “**Rad Setup Application**”. Let it install the GTK-run environment and libraries, as well as the program. The set-up application will create a program folder/group associated with RAD-Gtk (see below) and place a RAD icon on the screen. A subfolder with examples of RAD usage will also be created. Click on the RAD icon to run the program. Before installing a newer version of RAD, always Un-install the current version (to do it just click on Uninstall.../see below).



Mac OSX Users:

First install the GTK working environment - **GTK_Framework** then install RAD for **Mac OSX "Intel" 10.4** or **Mac OSX "Intel" 10.5** or **Mac OSX "Intel" 10.6**. RAD icon will be put in “**Applications**” folder. To run RAD just click on the icon. Examples coming with RAD will be put in folder: **usr/share/rad/examples**. Those may be moved to any other folder if the user decides so.

Note, RAD requires a screen resolution/size of at least 1000 x 800 pixels. If it is less than that some of the RAD functionalities described below may be lost. Also, occasionally RAD may not “wish” to start just after being installed. As with other applications – restart your computer and try again.

1. What is RAD ?

RAD takes x-ray diffraction (XRD) data and reduces it to an atomic pair/radial distribution function (PDF/RDF). It has been used by the author (VP) and many research groups all over the world for more than 20 years. It is based on rigorous XRD data reduction procedures established back when XRD was born. Yet RAD is under constant modification following the on-going development of XRD data collection procedures and instrumentation. **The author thanks Sebastien Le Roux for the invaluable help in developing a user friendly (GTK-based) interface for RAD.**

2. What is GTK+?

GTK+ is a toolkit for creating graphical user interfaces. GTK+ is written in C but has bindings to many other popular programming languages such as C++, Python and others.

3. What is XRD and atomic PDF/RDF analysis ?

XRD is used to determine the atomic-scale structure of materials. The technique is based on the fact that the wavelength of x-rays is comparable in size to the distances between atoms in condensed matter. So when a material exhibiting a long (i.e. at least μm)-range, periodic atomic order, such as a single crystal or polycrystalline powder, is irradiated with x-rays it acts as an extended periodic grating and produces a diffraction pattern showing numerous sharp spots, called Bragg diffraction peaks. By measuring and analyzing the positions and intensities of the Bragg peaks it is possible to determine the spatial characteristics of the grating – i.e. to determine the three-dimensional (3D) atomic arrangement in the crystalline material under study. This is the essence of the so-called “crystal structure” determination by XRD [1]. Over the years the technique has been perfected and applied successfully to a variety of crystalline materials – from simple metals to complex proteins. X-ray diffraction can also be applied to study the structure of materials where atoms are ordered only at short (i.e. less than a nm) to intermediate (tens of nm)-range distances such as liquids, glasses, fine (nano)sized powders, polymers etc. When irradiated with x-rays these materials act as quite imperfect gratings and produce

XRD patterns that are very diffuse in nature rendering traditional (Bragg-peaks based) crystallography very difficult to apply. A combination of higher-energy x-ray diffraction and atomic PDF/RDF data analysis [2] has proven to be very useful in cases like this.

The frequently used reduced atomic PDF/RDF, $G(r)$, gives the number of atoms in a spherical shell of unit thickness at a distance r from a reference atom as follows [2,3]:

$$G(r) = 4\pi r \rho_o [\rho(r)/\rho_o - 1] \quad (1)$$

where $\rho(r)$ and ρ_o are the local and average atomic number densities, respectively and r is the radial distance. As defined, **the PDF/RDF $G(r)$** is a one-dimensional function that **oscillates around zero** showing positive peaks at distances separating pairs of atoms, i.e. where the local atomic density exceeds the average one. The negative valleys in the PDF/RDF $G(r)$ correspond to real space vectors not having atoms at either of their ends. With this respect the atomic PDF resembles the so-called Patterson function that is widely applied in traditional x-ray crystallography [1]. However, while the Paterson function is discrete and peaks at interatomic distances within the unit cell of a crystal, the atomic PDF/RDF is a continuous function reflecting all interatomic distances occurring in a material. This is a great advantage when studying materials whose structure is difficult to be described in terms of extended periodic lattices. The PDF $G(r)$ is the Fourier transform of the experimentally observable total structure function, $S(Q)$, i.e.

$$G(r) = (2/\pi) \int_{q=0}^{q_{\max}} q[S(q) - 1] \sin(qr) dq, \quad (2)$$

where q is the magnitude of the wave vector ($q=4\pi\sin\theta/\lambda$), 2θ is the angle between the incoming and outgoing x-rays and λ is the wavelength of the x-rays used. X-ray diffraction usually employs the so-called Faber-Ziman type structure function, $S(q)$, related to **only(!) the coherent** part of the diffraction pattern, $I^{\text{coh.}}(q)$, as follows [2,3]:

$$S(q) = 1 + \left[I^{\text{coh.}}(q) - \sum c_i |f_i(q)|^2 \right] / \left| \sum c_i f_i(q) \right|^2, \quad (3)$$

where c_i and $f_i(q)$ are the atomic concentration and x-ray scattering factor respectively for the atomic species of type i . Note $f(q)$ is a function both of x-rays energy (E) and wave vector q , i.e. $f(q) = f_o(q) + f''(q, E) + if'(q, E)$ where f'' and f' are the so-called anomalous dispersion correction terms [1,2]. Also note, **as defined, $S(q)$ oscillates around one and $q[S(q)-1]$ – around zero.** It should also be noted that for a material comprising n

atomic species a single diffraction experiment yields a total PDF/RDF, $G(r)$, which is a weighted sum of $n(n+1)/2$ partial PDFs/RDFs, $G(r_{ij})$, i.e.

$$G(r) = \sum_{i,j} w_{ij} G_{ij}(r) \quad (4).$$

Here w_{ij} are weighting factors depending on the concentration and scattering power of the atomic species as follows:

$$w_{ij} = c_i c_j f_i(q) f_j(q) / [\sum_i c_i f_i(q)]^2 \quad (5).$$

For practical purposes w_{ij} 's are often evaluated for $q=0$ [2,3].

4. How XRD data suitable for atomic PDF/RDF analysis are collected ?

Source of radiation: The Fourier transformation (see Eq. 2) should not be terminated too early i.e. q_{max} should be at least $15-20 \text{ \AA}^{-1}$. Diffraction data at such high wave vectors can be obtained using x-rays of a shorter wavelength, i.e. of higher energy. X-rays of higher (than usual) energy can be delivered by synchrotron or laboratory sources such as sealed x-ray tubes with a Mo (energy $\sim 17 \text{ keV}$) or Ag (energy $\sim 22 \text{ keV}$) anodes. Note the energy of Cu K α radiation is only about 8 keV and, hence, q_{max} may not get higher than 8 \AA^{-1} or so. Therefore, **Cu K α radiation is not suitable** for higher-energy XRD aimed at atomic PDF/RDF data analysis.

XRD data statistics and collection time: Whatever source of higher-energy x-rays is used the XRD data should be collected with a very good statistical accuracy. That may mean having at least 10,000 counts collected at any data point/diffraction angle [4]. To achieve it XRD data may need to be collected much longer than in the case of more usual applications such as Rietveld analysis. Thus when a sealed x-ray tube source and a single point (e.g. scintillation) detector are employed the data collection may take tens of hours. More powerful sources of x-rays (rotating anode generators and synchrotrons) and/or large area detectors may reduce the XRD data collection time to minutes [5].

Experimental set-up (q -space) resolution: In general, structure studies on poorly- or completely non-periodic materials do not require experimental set-ups of very high reciprocal (q -space) space resolution because of the inherently diffuse nature of the respective XRD patterns. However, the reciprocal space resolution of the experimental

set up, including that of the detector, should not be too low either. As an example XRD patterns for polycrystalline Si (NIST powder standard) collected with two different types of detectors, a single point detector and an Image Plate (mar345) detector are shown in Fig. 1. The lower resolution of the XRD data collected with an IP detector leads to an extra broadening of the peaks in the XRD pattern and, hence, to a loss of information in the higher- r region of the corresponding atomic PDF. This loss *may be critical or not* depending on the degree of periodicity/crystallinity of the material studied.

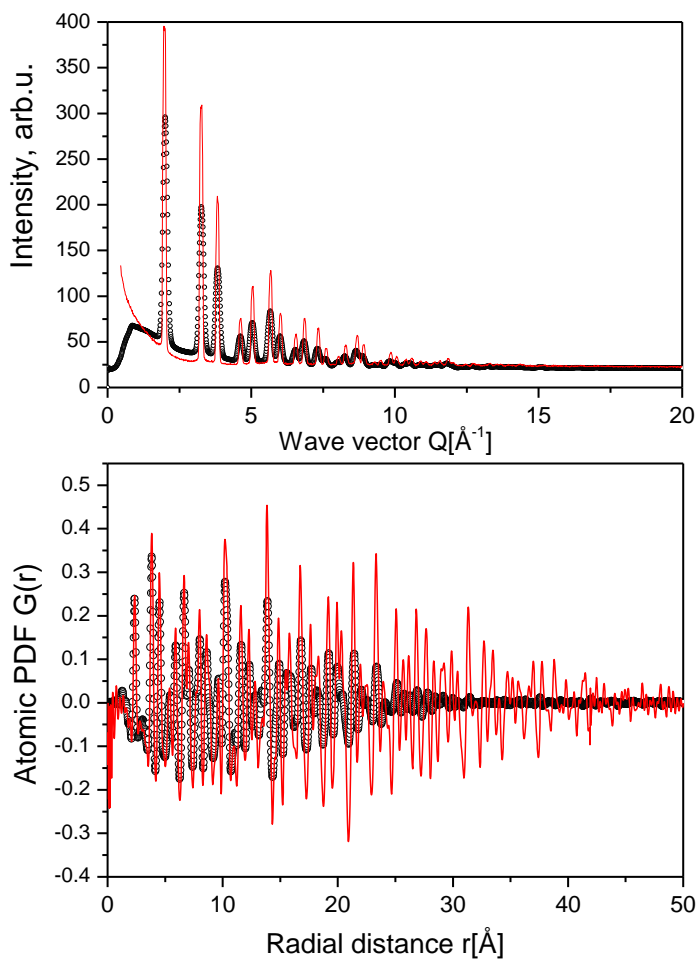


Figure 1. Experimental XRD patterns for Si powder collected with a point (solid line in red) and area IP/mar345 (symbols) detectors while the rest of the experimental set-up was kept unchanged. The corresponding atomic PDFs are shown in the lower part of the plot.

Background signal treatment: Air, sample holder etc. background-type scattering should be kept to a minimum since atomic PDFs are based on **only(!)** the coherent/elastic

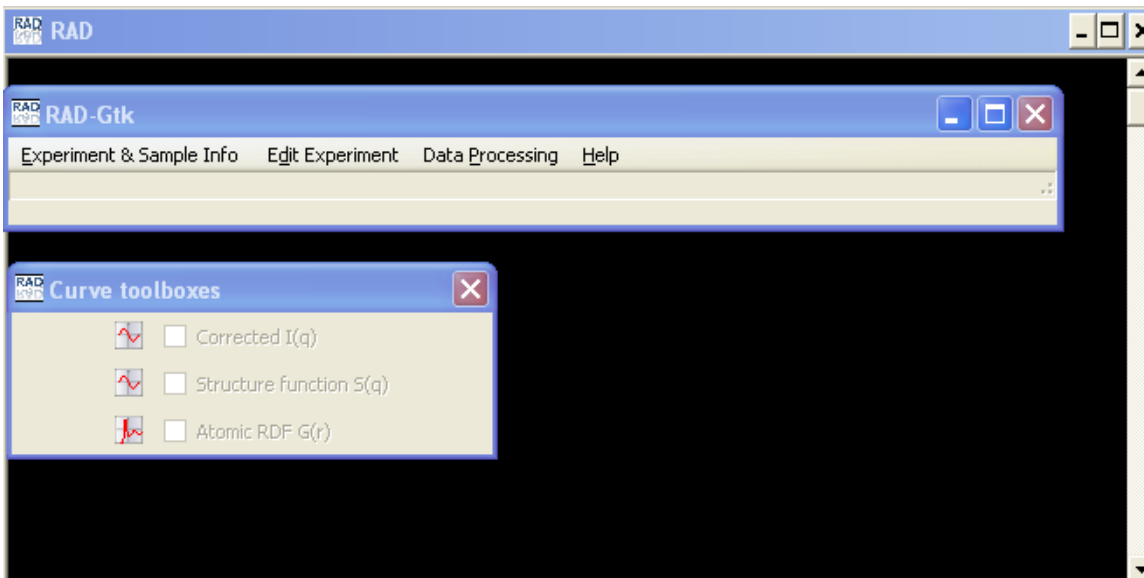
component of the XRD data (*see Eq. 3*). **Remember: weaker background signal is much easier to correct for !**

Sample related but “unwanted” signal: X-rays are both scattered from and absorbed inside materials via various processes [1,2]. The absorption of higher-energy x-rays is relatively low and usually does not pose much of a problem in the XRD data reduction process. The same is true for multiple scattering [2] of higher-energy x-rays. Inelastic (Compton) scattering, however, may be very strong, especially at high wave vectors [2]. If possible it should be eliminated from the experimental XRD data during data collection by using energy-sensitive detectors [6]. **Note analytical procedures for computing Compton scattering and subtracting it** from experimental XRD data are, inevitably(!), based on various approximations and, therefore, *may or may not work* well for every material. Fluorescent scattering from the sample should also be kept to a minimum. This could be achieved either by using an energy-sensitive detector and/or employing x-rays of energy below the absorption edge of the most strongly scattering atomic species in the material under study.

In summary, a successful atomic PDF/RDF study requires an XRD experiment done with a due care. Software like RAD can reduce virtually any XRD data set to an atomic PDF/RDF but whether this “PDF/RDF” is a physically meaningful representation of the atomic-scale structure of the material studied very much depends on the quality of experimental XRD data !

5. Using RAD :

Click on the RAD icon. The following 3 program windows will open (see below). One (labeled *RAD* in the upper left corner) is used to run/test RAD in an “expert mode”, display system/program error messages etc. The second (labeled *Curve toolboxes*) is used to display results computed by RAD, namely the corrected experimental data $I(q)$, the structure function $S(q)$ and the atomic PDF/RDF $G(r)$. Usually these two program windows have a limited usage and so may be “collapsed/minimized in size” (but still kept) active when RAD is running.

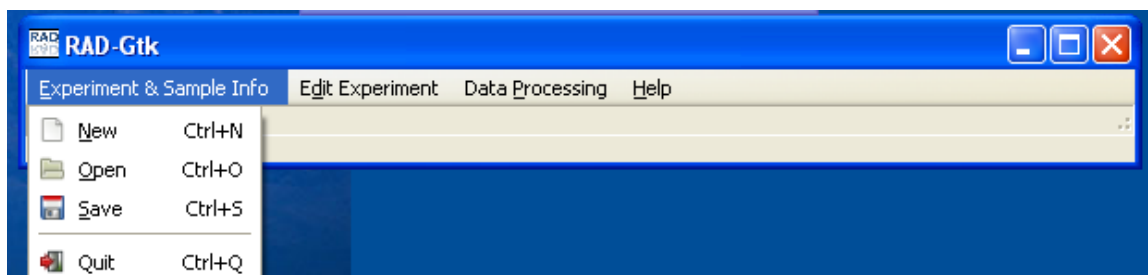


The third window (labeled *RAD-Gtk* in the upper left corner, see above) is the RAD's action control window. It too should be kept active while RAD is running.

This window allows the user to get access to the following actions/options (activated by clicking on them): *Experiment & Sample Info* Entry; *Edit Experiment* (Info); *Data Processing* and *Help*. Below we explain each of these options:

***Experiment & Sample Info* entry option of RAD-Gtk:**

When activated this option allows the user to start a new, open an existing or save a current RAD project or Quit (see below). RAD projects are text (xml format) files saved with an extension “rpf”. The files may be opened/viewed with any text editor.



RAD project files contain information about the material studied and the experimental set-up used. This information is needed to run the option *Data Processing*. Information

about the material include: the number of chemical species, the atomic number of each of the species, the species concentration and the anomalous dispersion terms (f' and f'') for that species and the radiation used. An example *Sample Description* entry is given below.

Project settings

Sample Description

Experiment Description

Sample description

Number of chemical species (max 10):

Species information:

Atomic species:

Atomic number:

Element: Al

Atomic concentration:

Parameters of the 5 Gaussian fit [1],
to the X-ray atomic scattering factors:

a1=	4.730796
b1=	3.628931
a2=	2.313951
b2=	43.051167
a3=	1.541980
b3=	0.095960
a4=	1.117564
b4=	108.932388
a5=	3.154754
b5=	1.555918
c=	0.139509

Dispersion correction f' [2,3]

Dispersion correction f'' [2,3]

[1] D. Waasmaier et al. Acta Cryst. **A51** (1995) p.416
 [2] <http://www.nist.gov/physlab/data/ffast/index.cfm>
 [3] D. Cromer Acta Cryst. **18** (1965) p.17

It features one of the first applications of RAD on in-house (Mo Ka) XRD data for Gd_4Al_3 metallic glass. Results from this study are published in: V. Petkov et al. "Radial distribution functions for RE_4Al_3 metallic glasses ($RE=Pr, Gd, Tb, Dy$)", *J. Non-Cryst. Sol.* **108** (1989) 75 (a copy of the paper is attached for user's convenience).

In this example (see above) we first enter the number of chemical species (**2** in our case) in the “Number of chemical species” data field (upper right corner; see above) and **hit Enter** ! This is the only time the user should hit the Enter key ! This tells RAD to open a “drop down list” menu button (second line from the top in the example window shown above) that lists (consecutively) the chemical species in the material studied. Then we enter the atomic number, Z , for species “**1**” – it is **13** for Al (see **Appendix 1**), and the atomic concentration of Al – 0.43. Note the chemical composition of the metallic glass in this example could be entered as: Gd_4Al_3 , $Gd_{57}Al_{43}$, $Gd_{0.57}Al_{0.43}$ etc. Here we opt for the last chemical formulation. The others would have been equally good. Users, however, should be aware that depending on the choice of the chemical formula unit the computed $q[S(q)-1]$ and PDF/RDF $G(r)$ would differ times a constant factor which scales with the total number of atoms in the respective chemical/formula unit used [2,3].

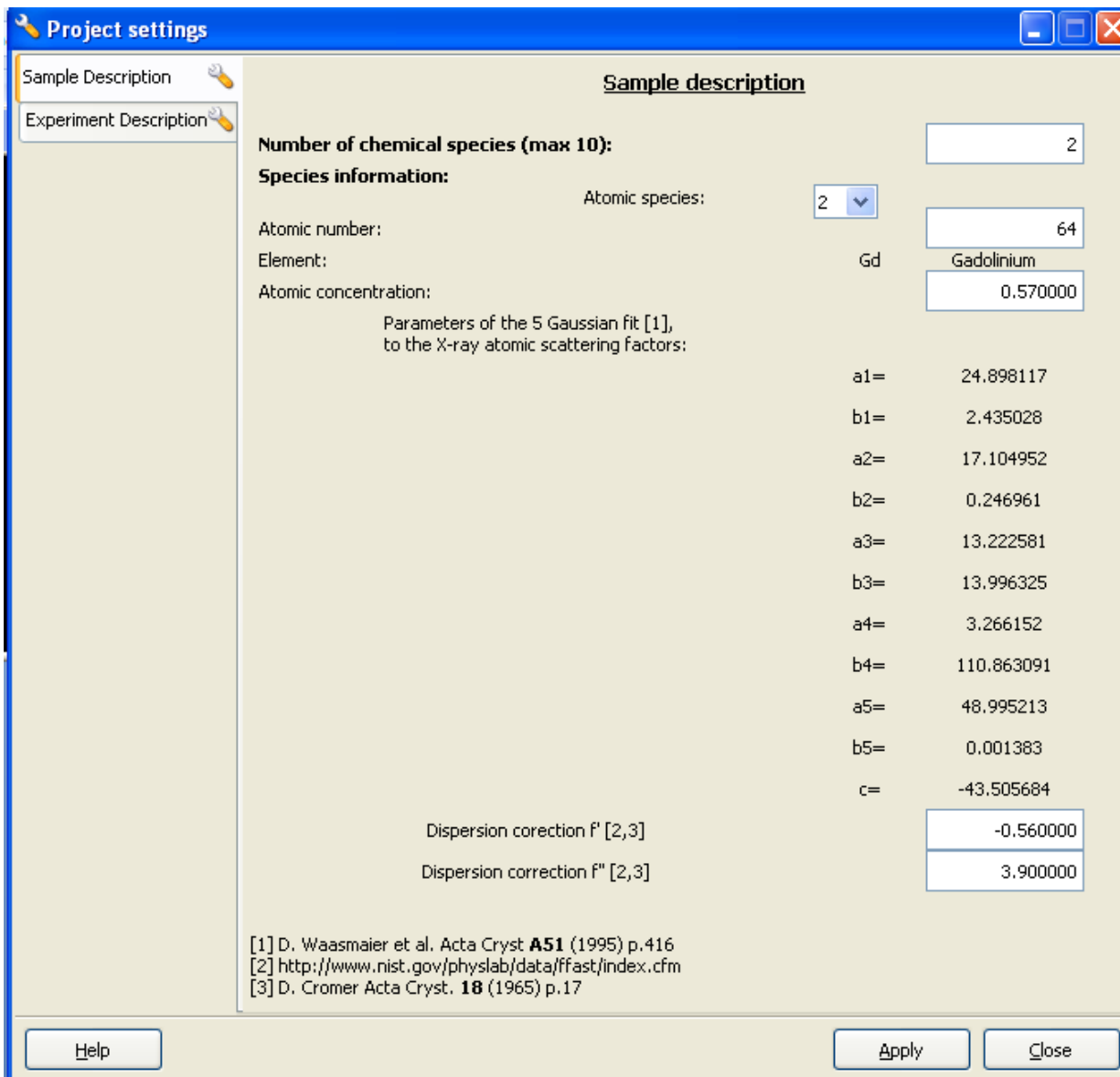
RAD users: be consistent in your choices of the chemical formula unit for the material you study! Stick to the same formula unit (e.g. $Gd_{0.57}Al_{0.43}$) when you use the respective PDF/RDF data to extract atomic coordination numbers and/or fit/compare the experimental PDF/RDFs with structure models.

In this example we/the user should also supply information about f' (=0.056) and f'' (=0.051) for Al when Mo K α radiation is used. Information for f' and f'' may be obtained from the National Institute of Standards & Technology www site

http://www.nist.gov/physlab/data/xray_gammaray.cfm

or from literature sources (e.g. the f' and f'' values for Mo and Ag radiation as computed by D. Cromer are given in **Appendix 2** for RAD users' convenience). Information about the atomic scattering factors $f_o(q)$ for atomic species with $Z=1$ to $Z=98$ comes with RAD

so the user should not worry about it. Here is the place to note that RAD can handle XRD data sets from materials composed of **up to 10** atomic species with atomic numbers, **Z**, **from 1 to 98**. Selecting “*Atomic Species*” **2** from the drop down list allows the user to supply information about Gd, as exemplified below.



Next, by clicking on the “*Experiment Description*” button (left upper corner) the user is allowed to supply information about the particular XRD experiment/set up; as shown below.

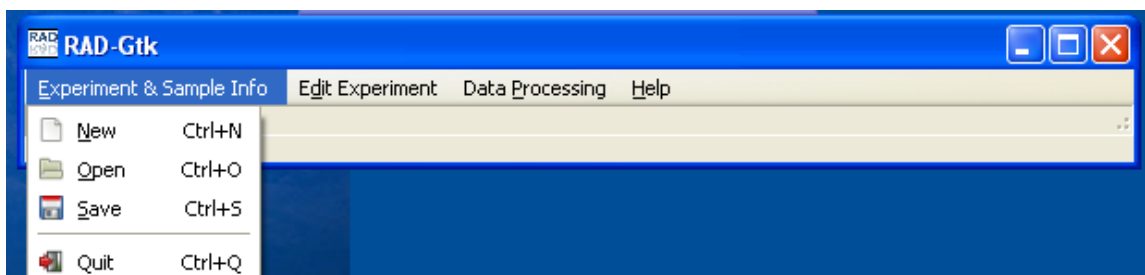
The screenshot shows a software window titled "Project settings" with a sub-tab "Experiment Description". The window contains the following parameters and their values:

Parameter	Value	Unit
X-ray wavelength:	0.709000	Å
Linear absorption (sample)	0.675000	μt
Linear absorption (substrate/cell)	0.000000	μt
Sample's density	0.039200	Atoms / Å ³
Detector's dead time:	0.000000	s
Experimental geometry	Reflection	
Polarization type	In-house/circular	
Compton scattering	All in	

At the bottom of the window are three buttons: "Help", "Apply", and "Close".

Here we specify that x-rays with a wavelength $\lambda=0.709 \text{ \AA}$ (i.e. Mo K α) has been used; the sample was measured in flat plate reflection geometry; the detector was fast enough for the signal coming from the sample (i.e. 0.2 μs dead time) and the x-ray radiation was circularly polarized (which is typical for sealed x-ray tube sources). There has been no x-ray energy discrimination during the XRD data collection and, hence, the XRD data contain a contribution coming from Compton/inelastic scattering (i.e. Compton scattering

is “*All in*” the collected XRD data). The linear absorption factor μt for the particular $\text{Gd}_{0.57}\text{Al}_{0.43}$ sample has turned out to be 0.675. Note μt can be measured (more precise approach; see Appendix 4) or estimated [1, 2] from the material’s mass absorption coefficient μ/ρ , density ρ and thickness (less precise approach). Also, here we supply information about the material’s atom number density ρ_o (in this case = 0.0392 atoms/Å³). No sample cell/substrate has been used and so the data entry for substrate’s μt is zero. Note RAD can also process data collected in flat plate transmission geometry or when the sample has been inside a capillary. Also, x-rays could have been completely linearly polarized (as with synchrotron sources) and Compton scattering could have been eliminated during data collection (option Compton scattering “*All out*”). The user can select between those options by clicking on the respective “drop down menus” in the “*Experiment description*” window. When all the necessary sample and experiment related information has been supplied, the user should click the “*Apply*” button (lower right corner; see above). RAD will perform some checks on the consistency of the *Sample & Experiment Info* provided by the user and may issue a warning message if a problem is identified. Users are advised to pay full attention to RAD’s warning/error messages. *Experiment & Sample Info* that has been entered and found error free is considered “validated” and so can be saved as a “**RAD project file**” (in xml format) with an extension “.rpf”. To save a project file the user should select the “*Save*” option (see below).



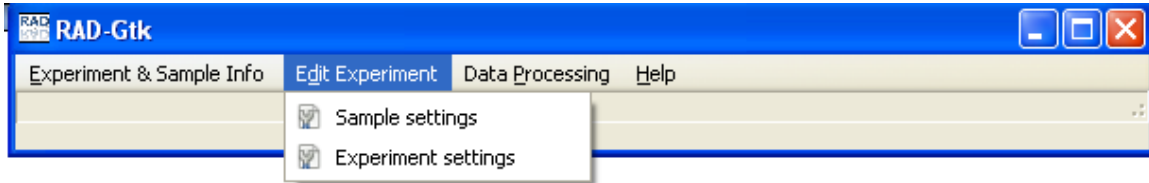
Again, RAD project files are text files; once saved on disk they may be opened/viewed with any text editor. As an example, below is a print-out of the RAD project file for $Gd_{0.57}Al_{0.43}$ we are discussing here:

```

<?xml version="1.0" encoding="UTF-8"?>
<!-- RadGTK v1.0 XML file -->
<rad-xml>
  <!-- Chemistry information -->
  <chemistry>
    <species number="2">
      <z id="0">13</z>
      <z id="1">64</z>
    </species>
    <element symbol="Al">
      <name>Aluminum    </name>
      <z>13</z>
      <concentration>0.430000</concentration>
      <fp>0.056000</fp>
      <fpp>0.051000</fpp>
    </element>
    <element symbol="Gd">
      <name>Gadolinium  </name>
      <z>64</z>
      <concentration>0.570000</concentration>
      <fp>-0.560000</fp>
      <fpp>3.900000</fpp>
    </element>
  </chemistry>
  <!-- Experiment information -->
  <experiment>
    <wavelength>0.709000</wavelength>
    <absorption-sample>0.675000</absorption-sample>
    <absorption-substrate>0.000000</absorption-substrate>
    <density>0.039200</density>
    <deadtime>0.0000002</deadtime>
    <geometry>Reflection </geometry>
    <monochromator>In-house/circular</monochromator>
    <compton>All in</compton>
  </experiment>
  <!-- Apply project -->
  <project>TRUE</project>
</rad-xml>

```

Experiment & Sample Info that has just been entered by the user or read from an old/existing project file can be modified by selecting the “*Edit Experiment*” option (see below) of the RAD-Gtk window.

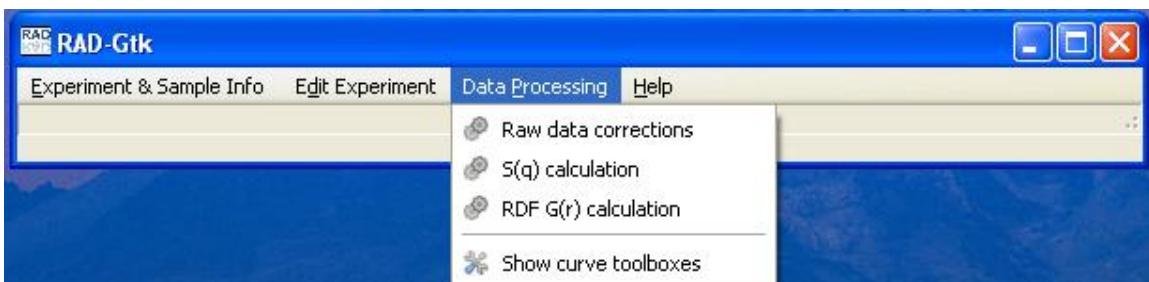


Edit Experiment option of RAD-Gtk:

When selected (see above) it will allow the user “to walk” through the “*Experiment & Sample Info*” forms, make changes, validate and eventually save the modified *Info*.

Note *Experiment & Sample Info* changes are accepted and taken into account in the XRD data processing/PDF calculations only after the “*Apply*” button has been hit and the validation procedures completed with success (i.e. no RAD error/warning messages).

Data Processing option of RAD-Gtk: can be activated only if a “RAD project file” has been created from scratch or read from disk, and validated.

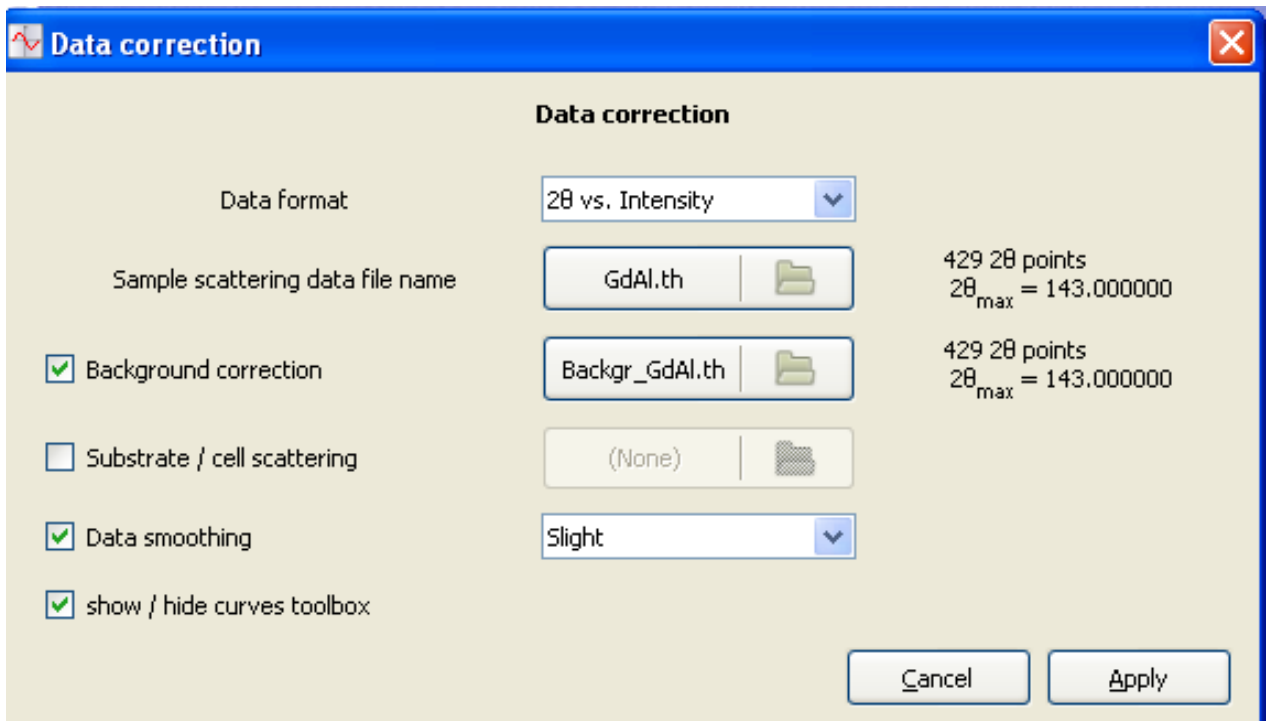


This option allows the user to:

- 1) Correct an experimental XRD data set for background (e.g. air) & sample cell (e.g. empty capillary) scattering, absorption and polarization, smooth the data (if necessary),

extend/extrapolate it (linearly) to $q=0$ wave vectors and put it in equidistant Δq steps. The result is saved as a file (in x,y ascii format) of corrected XRD data. Such a file is needed to compute the respective $S(q)$.

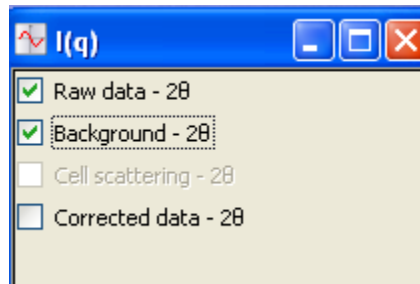
To do the correction the user activates the step “*Raw data corrections*” from the **Data processing RAD-Gtk option**” and supplies the names of the files containing the XRD intensities scattered from the sample (file **GdAl.th** in our example, see below) and background/air (**Backgr_GdAl.th** in our example, see below). Note, in this example, the sample was free standing and no support/cell scattering was present. Also, in this example we decided to smooth the XRD data (“*slightly*”). Then we hit the “*Apply*” button (lower right corner; see below). RAD will read the experimental XRD data files and report the number of data points in them as well as the value of the Bragg angle/wave vector for the last XRD data point collected (see the right hand side of the example below)



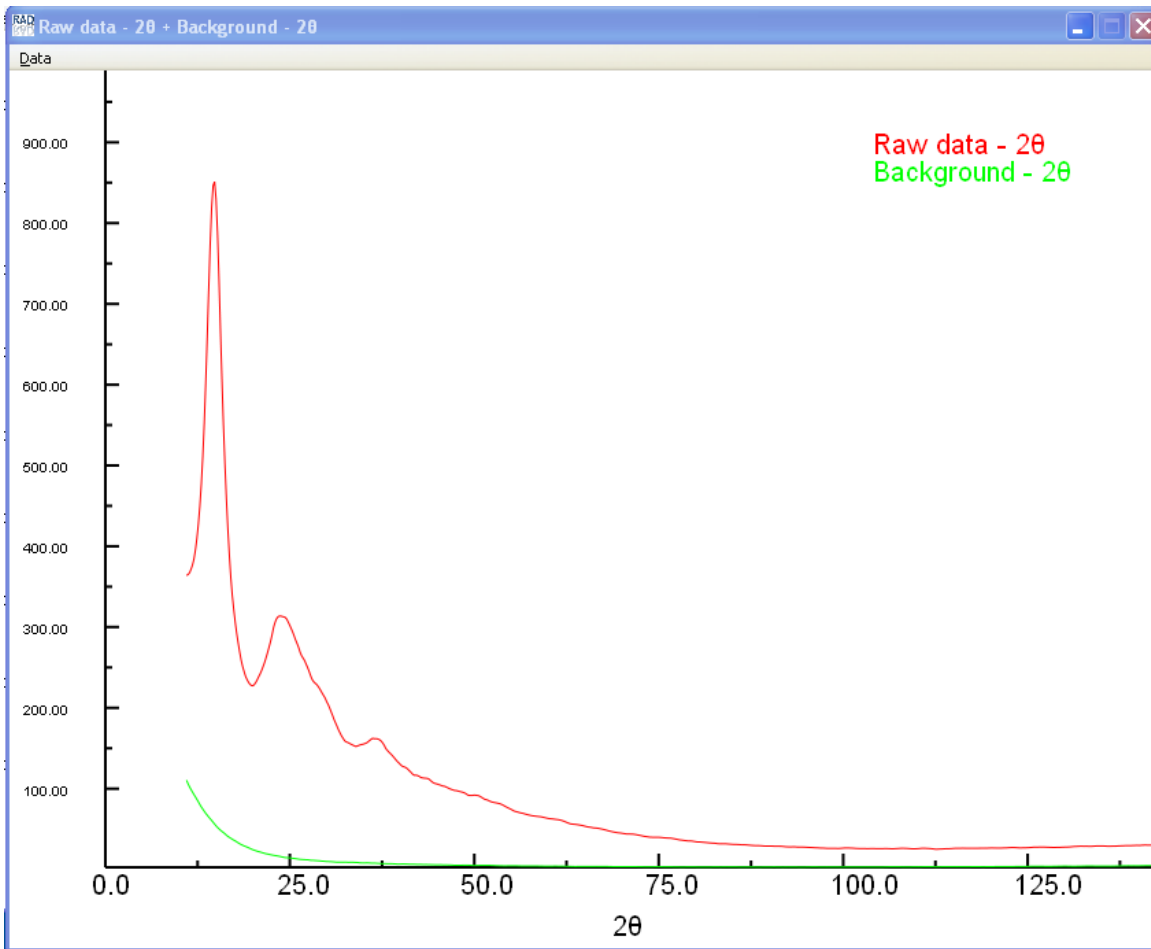
When the experimental XRD data sets are entered and corrections are done without any problem (RAD notices problems reports about them), a separate pop-up window appears (labeled **I(q)** in the up left corner; see below). It allows the user to view the experimental sample & background XRD data sets and the corrected I(q) data.

Note, occasionally this, and other smaller-size RAD program windows, may appear (pop-up) behind the main RAD program window and so remain “hidden” from the user’s sight. Users: feel free to shift RAD windows around on the computer screen to be able to see/access them in the most convenient (for you) way.

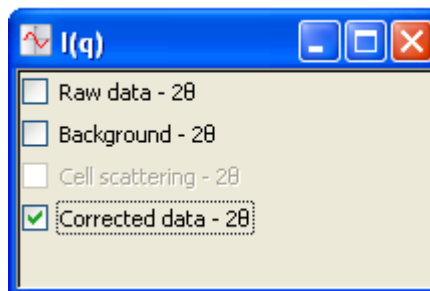
By checking the boxes “*Raw data*” and “*Background*” (see below)



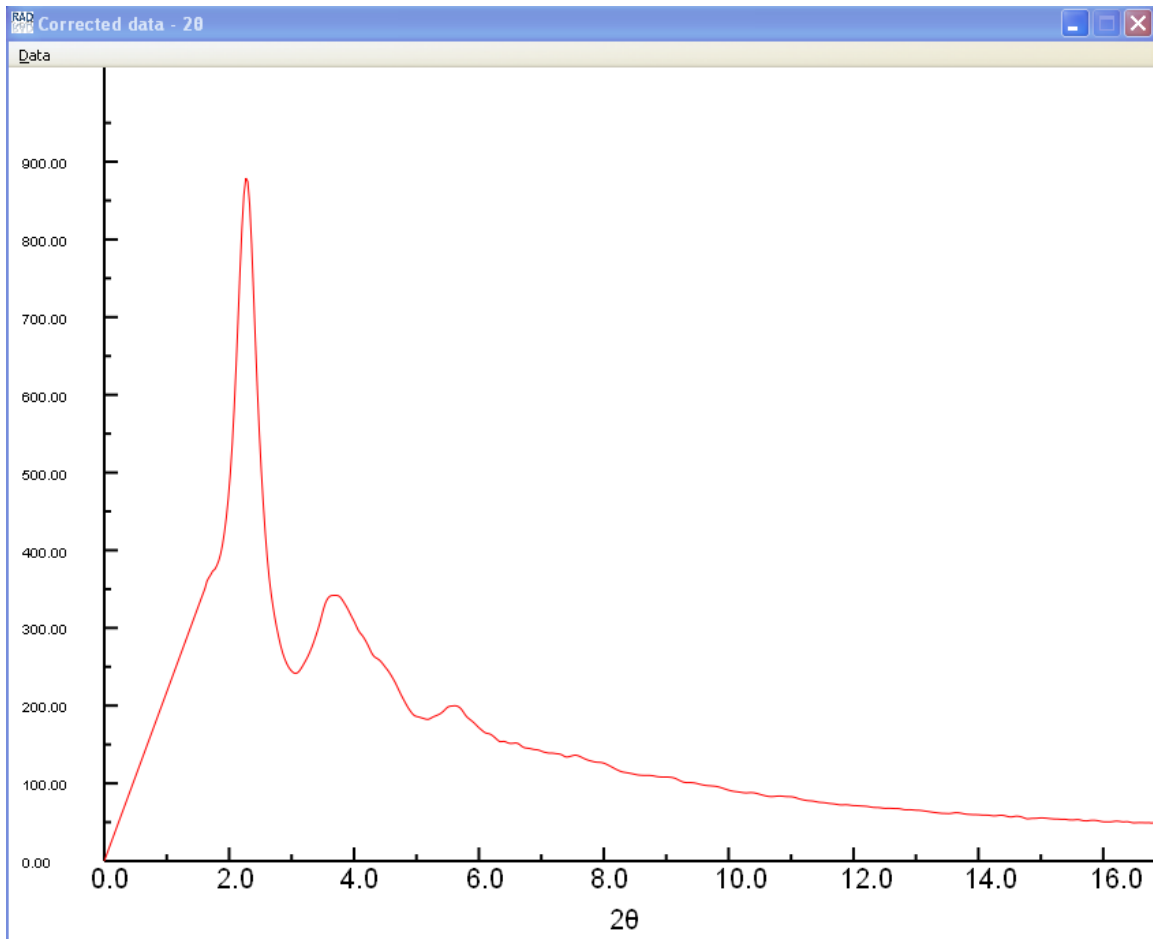
the user can plot/view the experimental data he/she is analyzing. They appear in yet another *Data plotting window* (see below).



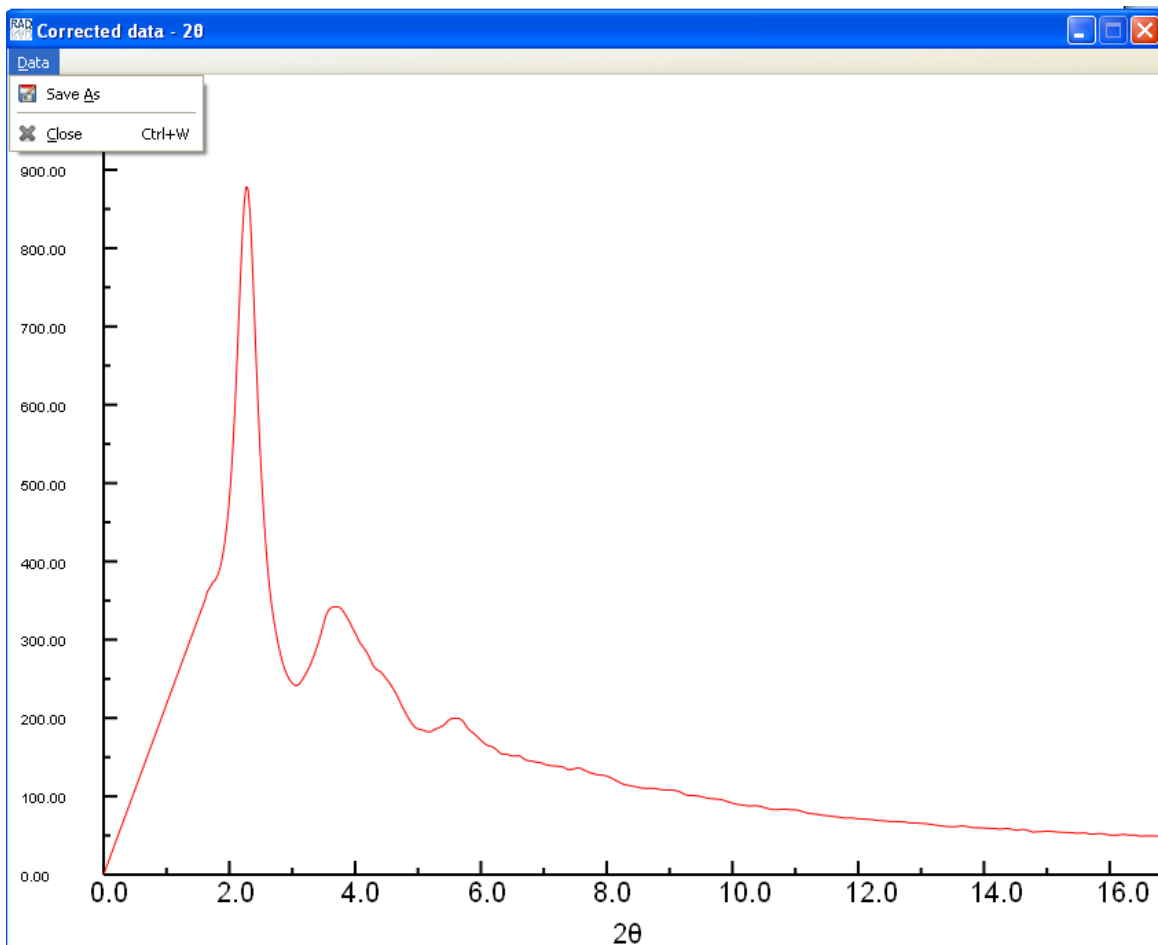
If/when the user checks the “*Corrected data*” box (see below)



he/she can plot/view the corrected and extrapolated to $q=0$ data, $I(q)$ – see below.



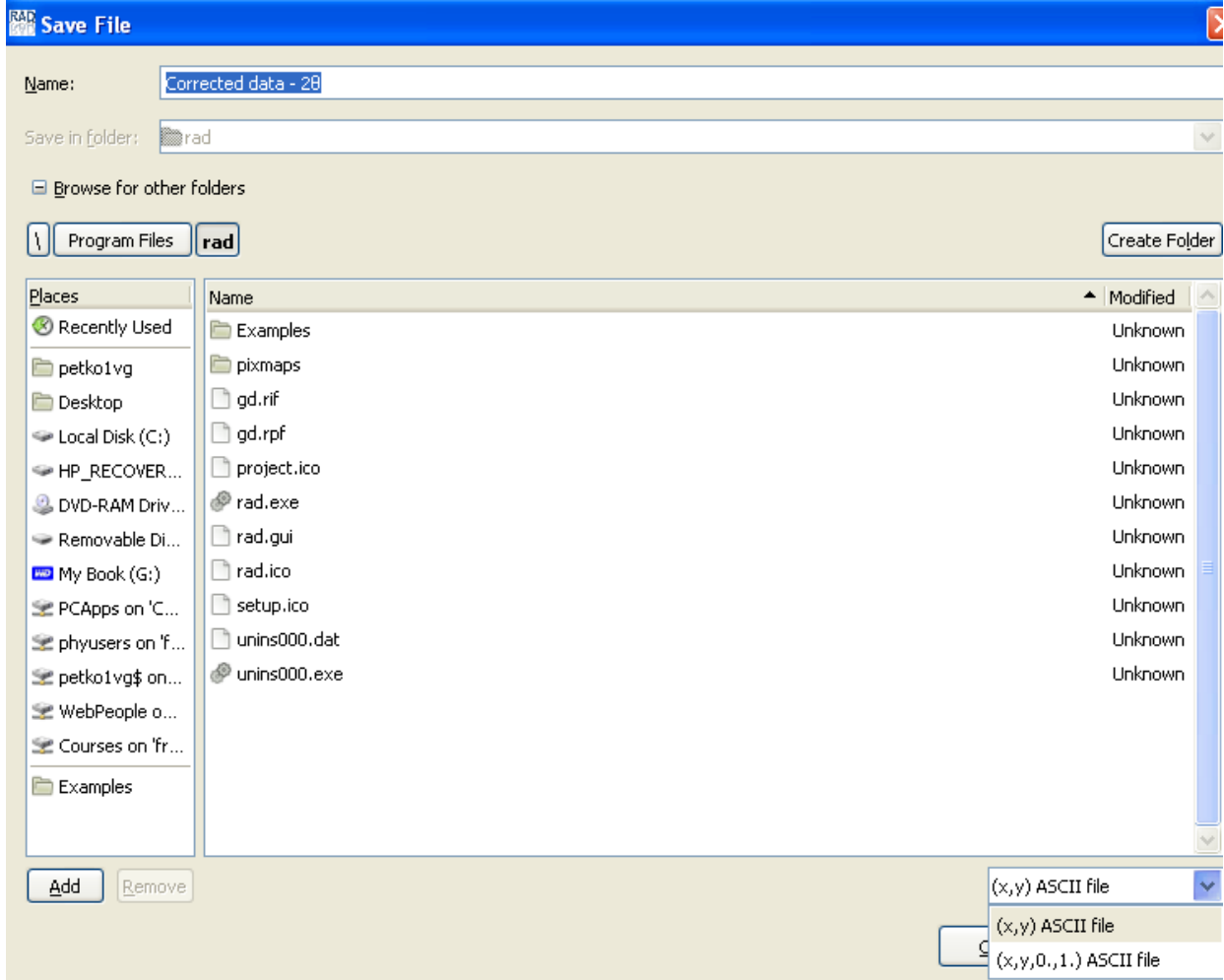
If the user is satisfied with the experimental XRD data corrections, he/she could check the “Data” option in the upper left corner of the *Data plot window* (see below).



A drop-down menu (see above) will appear allowing the user to save the corrected data $I(q)$ or close the data plot window. If the “Save As” option is selected a new window appears (see below). It allows the user to save the $I(q)$ data in **(x,y ascii format)** (see the screen-shot below). **Note this data format has been chosen to be the working format of RAD.** In this example we save the corrected XRD data in a file – “*GdAl.cor*”

The user is free to select any file name/extension for the corrected XRD data. An option is provided to save the data in **(x,y,0,1 ascii format)**. This is a 4 column ascii file where the third and fourth columns are “zeros” and “ones”. This format is not used by RAD but by other programs and is introduced just to make RAD’s output portable to third party

software applications such as DISCUS and PDFgui. So again, RAD users show save their results in the **(x,y ascii format)** when those results are to be used in other calculations to be performed by RAD. Use the **(x,y,0,1 ascii format)** if RAD's output is to be ported to DISCUS (<http://discus.sourceforge.net/>) or PDFgui (<http://www.diffpy.org/>).



Experimental XRD data format: (see files “GdAl.th” and “Backgr_GdAl.th” for example) RAD assumes that the experimental XRD data are presented as two columns

(2θ or q value vs intensity) in ascii format. RAD saves and uses the computed $I(q)$, $S(q)$ and $G(r)$ in the same (x,y ascii) format.

For example, below is what “GdAl.th” looks like when opened/viewed with any text editor: just two columns of numbers. The first is the Bragg angle (in 2θ), the second – XRD intensity (in counts per second).

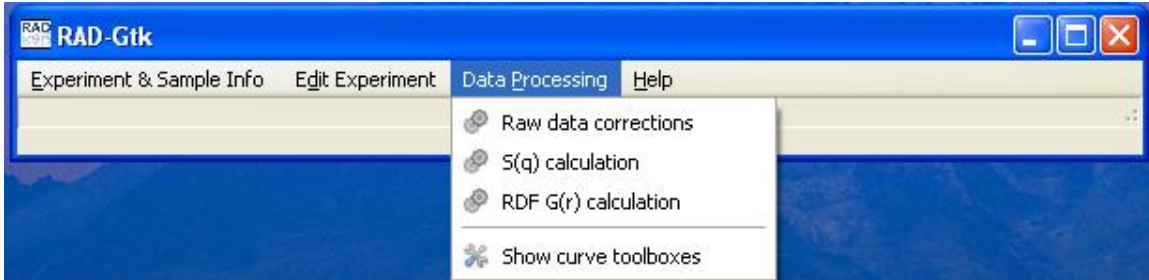
```
| 11.0000 363.7205
  11.2000 365.0381
  11.4000 366.9811
  11.6000 371.4045
  11.8000 376.6112
  12.0000 383.9672
  12.2000 395.1406
  12.4000 409.4046
  12.6000 427.4286
  12.8000 449.3842
  13.0000 476.6588
  13.2000 511.2541
  13.4000 552.3105
  13.6000 602.4041
  13.8000 658.4647
  14.0000 717.2819
  14.2000 773.2896
  14.4000 818.5352
  14.6000 846.4656
  14.8000 851.1745
  15.0000 829.6508
  15.2000 787.0467
  15.4000 729.4600
  15.6000 665.7761
  15.8000 605.8624
  16.0000 550.0443
  16.2000 501.5684
  16.4000 459.2458
  16.6000 421.5414
  16.8000 389.0881
  17.0000 361.3227
  17.2000 339.1941
  17.4000 321.6118
  17.6000 305.7858
  17.8000 292.0141
  18.0000 280.2086
```

The number of data points (per file), experimental or RAD computed, **may not be more than 30,000**. Also, a single experimental XRD intensity value and, therefore, computed

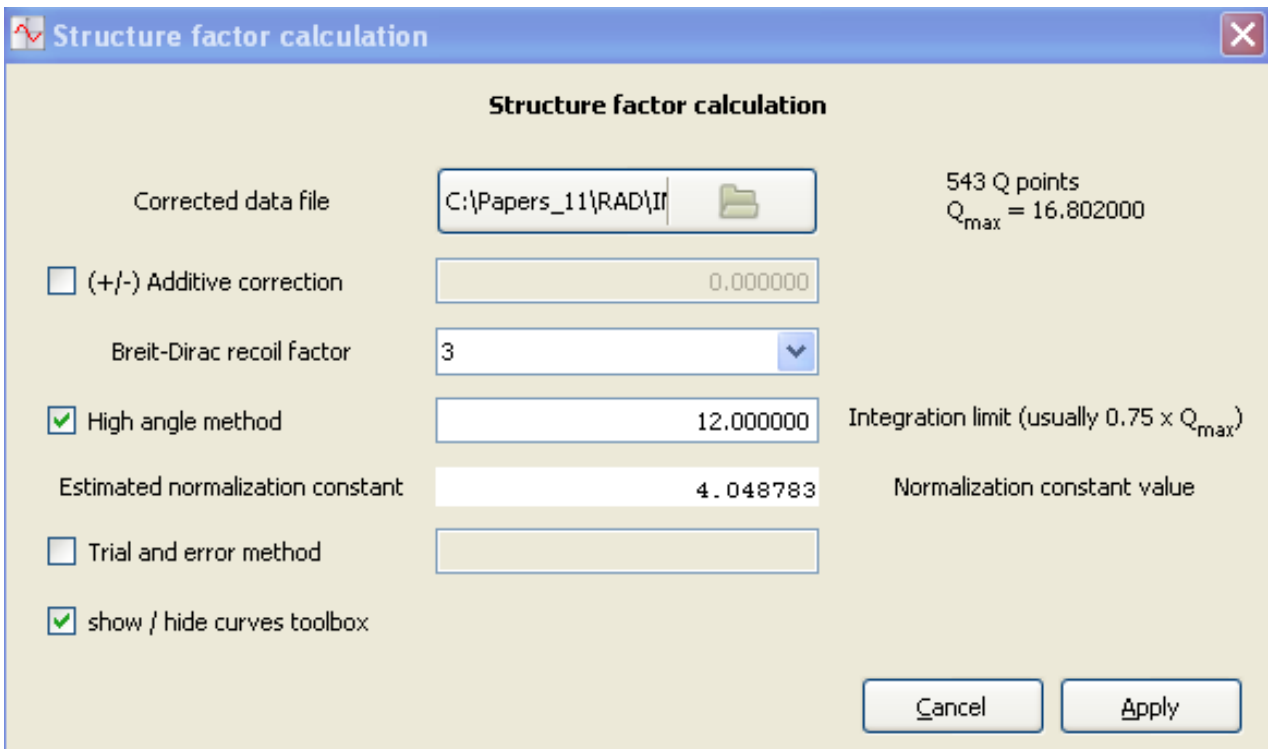
I(q), S(q) and G(r) value **should not be larger than 10^6** . Users, please, try not to exceed count rates of 10^6 cps (per single detector), do not saturate detectors and so go in the non-linear detector dead time correction regime ! Keep the number of data points (per pattern) below 30,000 and normalize the XRD intensities in your patterns per second/per the number of detectors/per the number of angular sectors of integration (if using an area detector) etc, i.e. take care that no single intensity data point in the experimental XRD files has a value greater than 10^6 . Then the XRD data corrections implemented in RAD may work. Indeed why such limitations ? Users: RAD is just like a... car. A car is designed to tow a particular load, carry a particular number of passengers, run with a particular maximum speed etc. Attempts to run a car beyond its build-in capabilities will blow its engine out. The same will happen to RAD. No good for anybody.

Also, the author (VP), after some careful thoughts, decided that it does not worth the effort to try propagating “experimental/counting/statistical etc” errors from the raw XRD data to I(q) then to S(q) and finally to PDF/RDF G(r). Error propagation via a Fourier transformation is tricky. Instead the author suggests RAD users consider that all data points of the derived S(q)s and G(r)s are with the same “random-type” (+/-) error, **i.e. assume/use uniform errors/weights in all S(Q)/PDF/RDF data**. By the way, studies [7] showed that this assumption is quite appropriate. Within this assumption each **S(Q)/PDF/RDF data** point is assigned uniform(i.e.=”1”) error. The **S(Q)/PDF/RDF data** then can be saved in the **(x,y,0,1 ascii format)** and directly used by PDFgui and DUSCUS in structure refinements. The standard deviations of the structural parameters resulted from those refinements will be based on the “**one unit**” errors in each of the **S(Q)/PDF/RDF data points** against which the structure model has been refined.

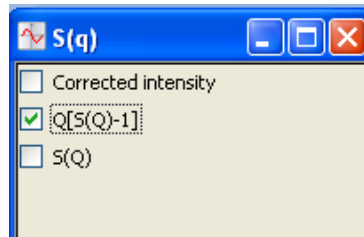
2) Compute a total structure factor $S(q)$ from corrected XRD/ $I(q)$ data



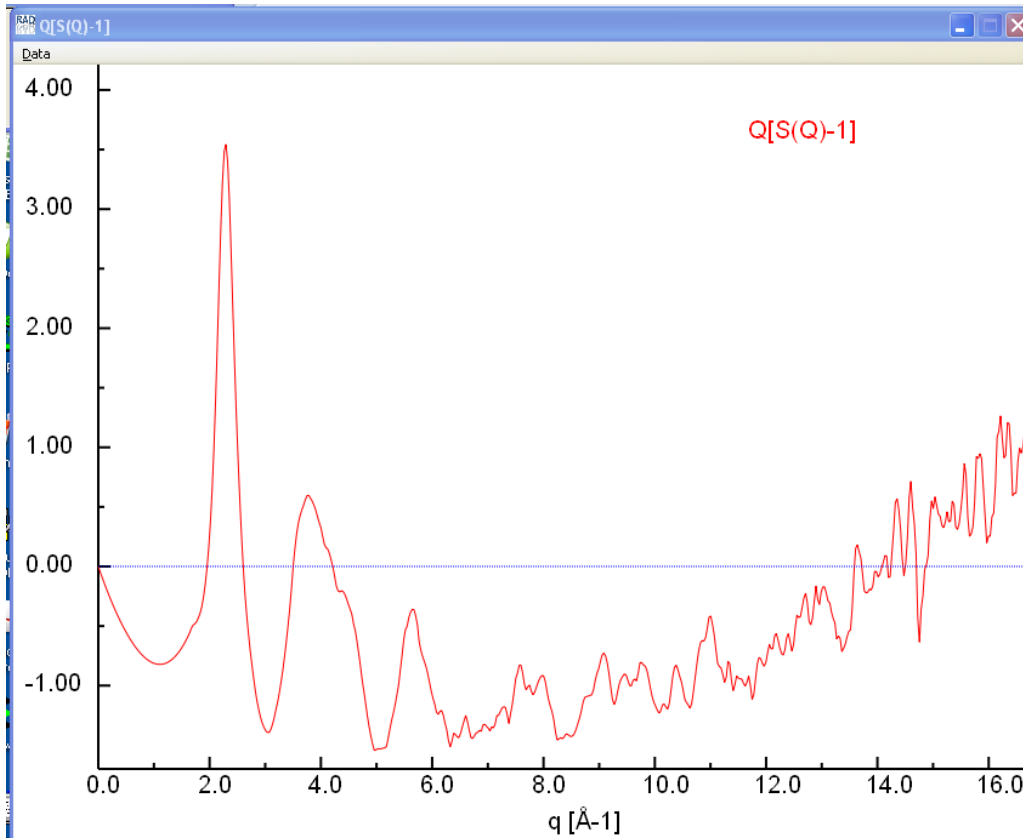
To do it the user should activate the option “ $S(q)$ calculation” from the drop-down menu list of “*Data processing*” RAD-Gtk window (see above), and enter the name of the file containing the corrected XRD data, $I(q)$: (file GdAl.cor in our example, see below). RAD reads the data file and reports that, in this case, it has 543 data points, the last one being at $Q_{\max} = 16.802 \text{ \AA}^{-1}$. Since Compton scattering is present in the XRD data



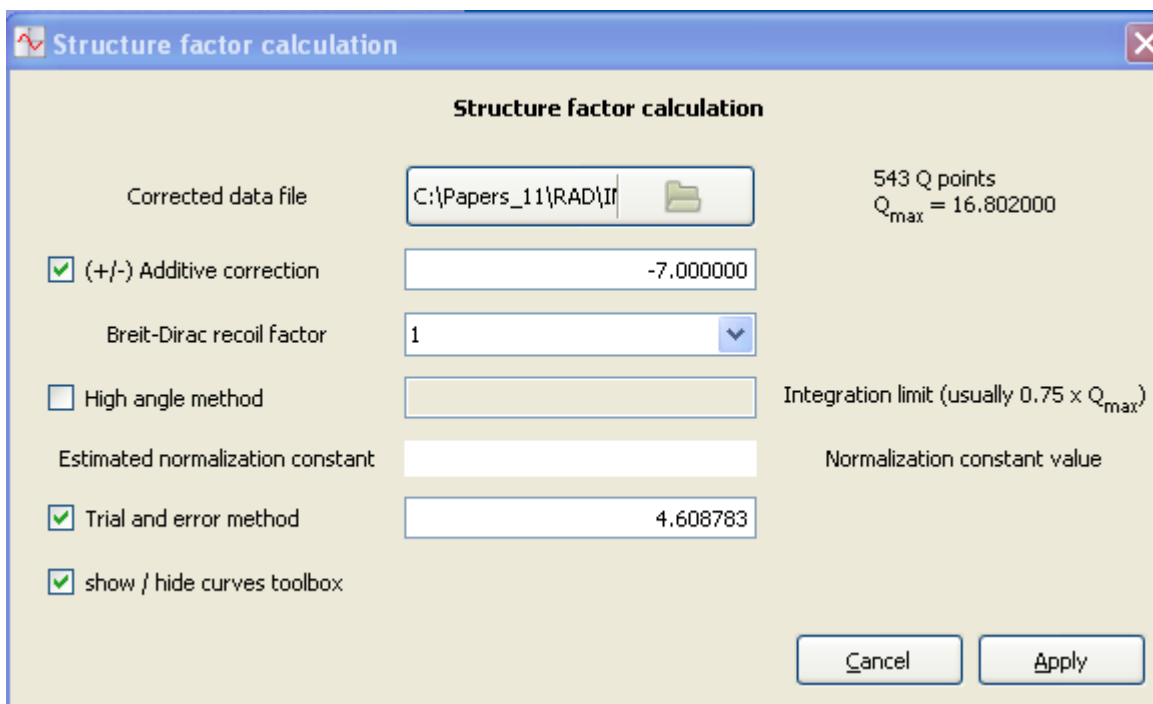
(since no x-ray energy sensitive detector has been used during data collection) the former has to be computed and subtracted from the latter. Here the user should decide about the value for the so-called Breit-Dirac recoil factor [2]. RAD offers values of 1, 2 or 3. The user selects the way the $I(q)$ data is to be normalized into absolute/electron units. At first the so-called “high-angle method” may be selected (by checking the relevant box, see above) and a value for the “limit of integration” - provided (12 \AA^{-1} in our example). The user hits “Apply”, RAD computes a normalization constant (4.048 in the example above), converts the $I(q)$ data in absolute units, subtracts the computed Compton scattering and computes the structure factor $S(q)$ and the so-called reduced structure factor $q(S(q)-1)$ [2,3] (the attached JAC paper describing RAD gives description of the normalization process/ $S(q)$ calculation in some more detail). Again, a separate pop-up window appears, this time labeled $S(q)$ in the upper left corner (see below). It allows the user to plot/view the computed $S(q)$ or $q(S(q)-1)$ data.



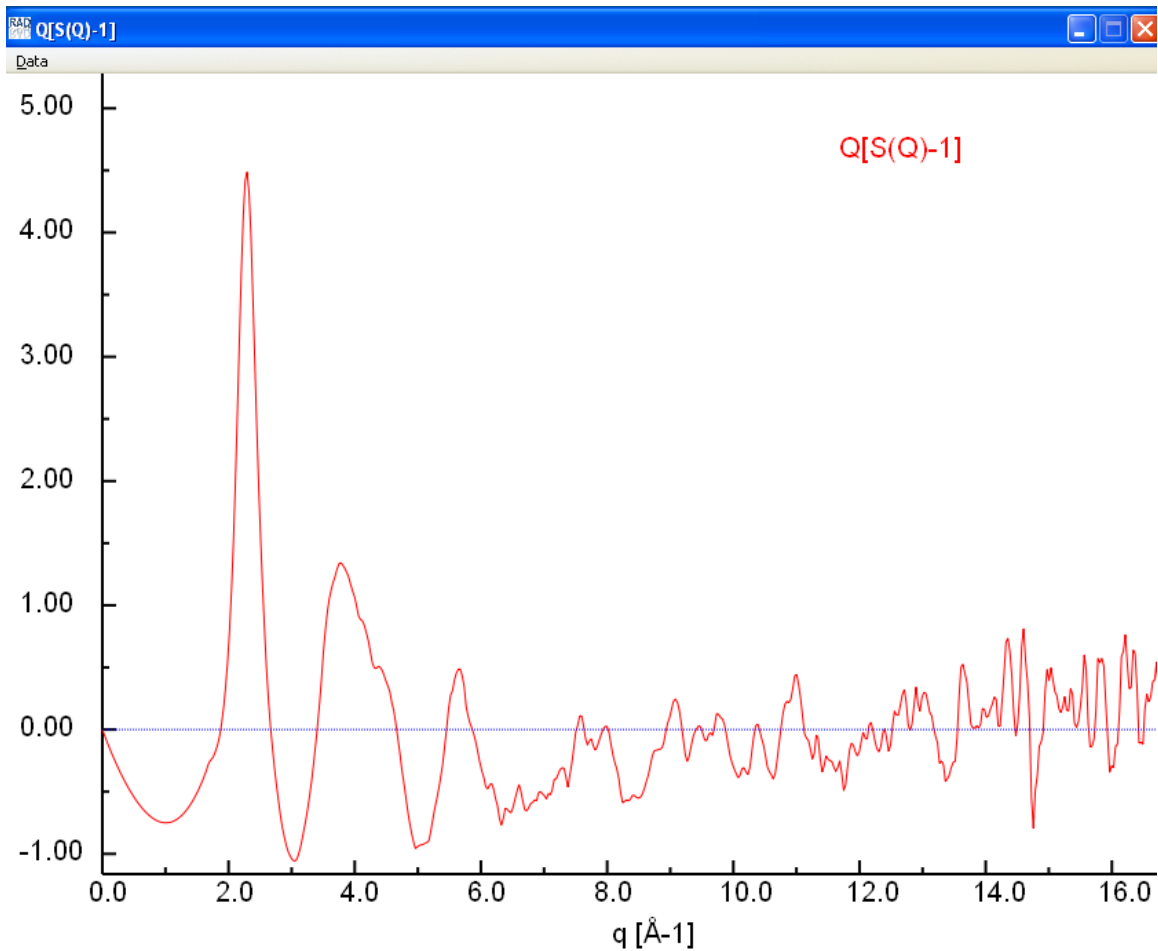
In this example we decide to plot $q(S(q)-1)$. The result is shown below.



This $q(S(q)-1)$ data is not of very good quality since it does not oscillate around zero (for user's convenience zero appears as a fine dotted line). Obviously some XRD data corrections and/or $I(q)$ data normalization have not been done in a precise enough way. RAD provides an option to "correct" for some small residual errors in the $I(q)$ data by adding/subtracting a constant.

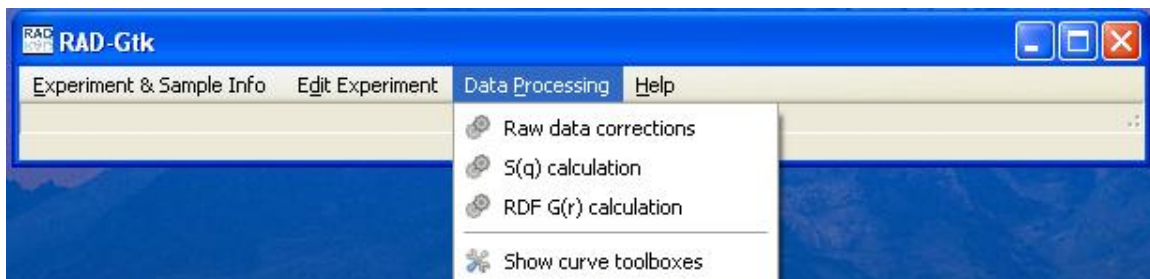


By “trial and error” (yes, human intervention is still important in PDF/RDF data analysis) we “decide” to subtract a small number (-7) from the originally corrected $I(q)$ data, and to apply a normalization constant of 4.608 (note it is close but not the same as the “high angle method” estimate of 4.048). The corresponding $q(S(q)-1)$ shows a much better behavior (see below) and we decide to save it. To do it we check the “Data” option in the $q(S(q)-1)$ data plot window (see below). A drop-down menu appears and again we use the “Save As” option.

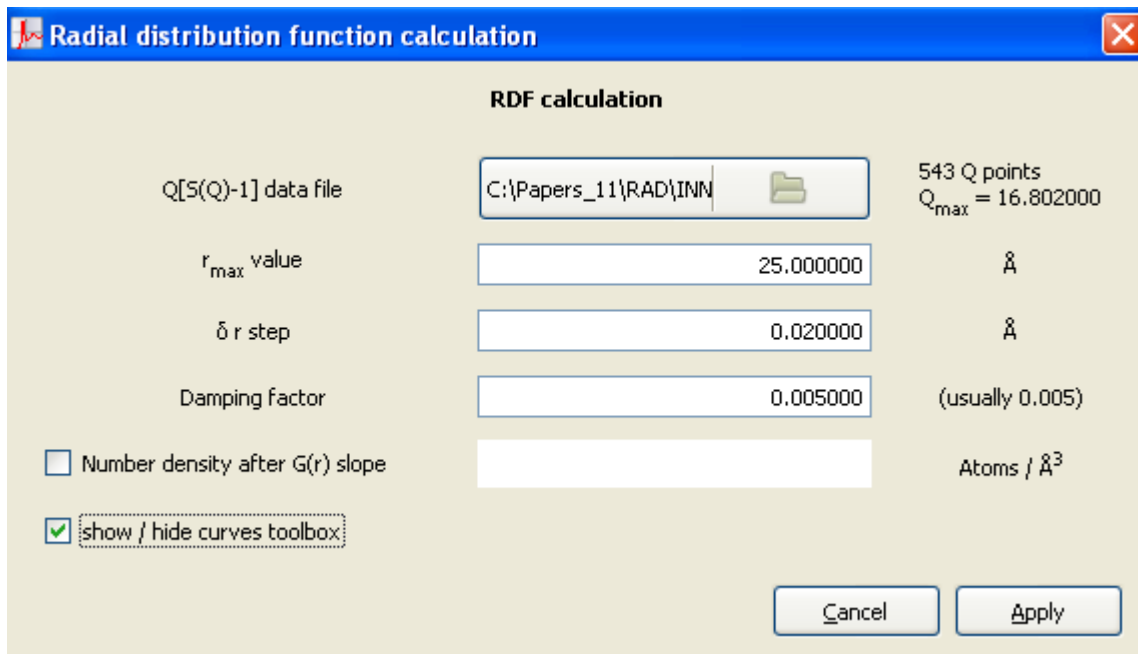


The user is free to select any file name/extension for the $q(S(q)-1)$ data. We saved it under the name “*GdAl.qsq*” in (x,y ascii) format.

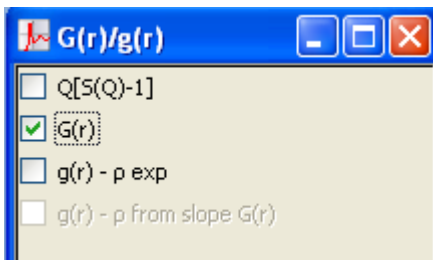
3) Compute an atomic PDF/RDF from a reduced factor $q(S(q) - 1)$



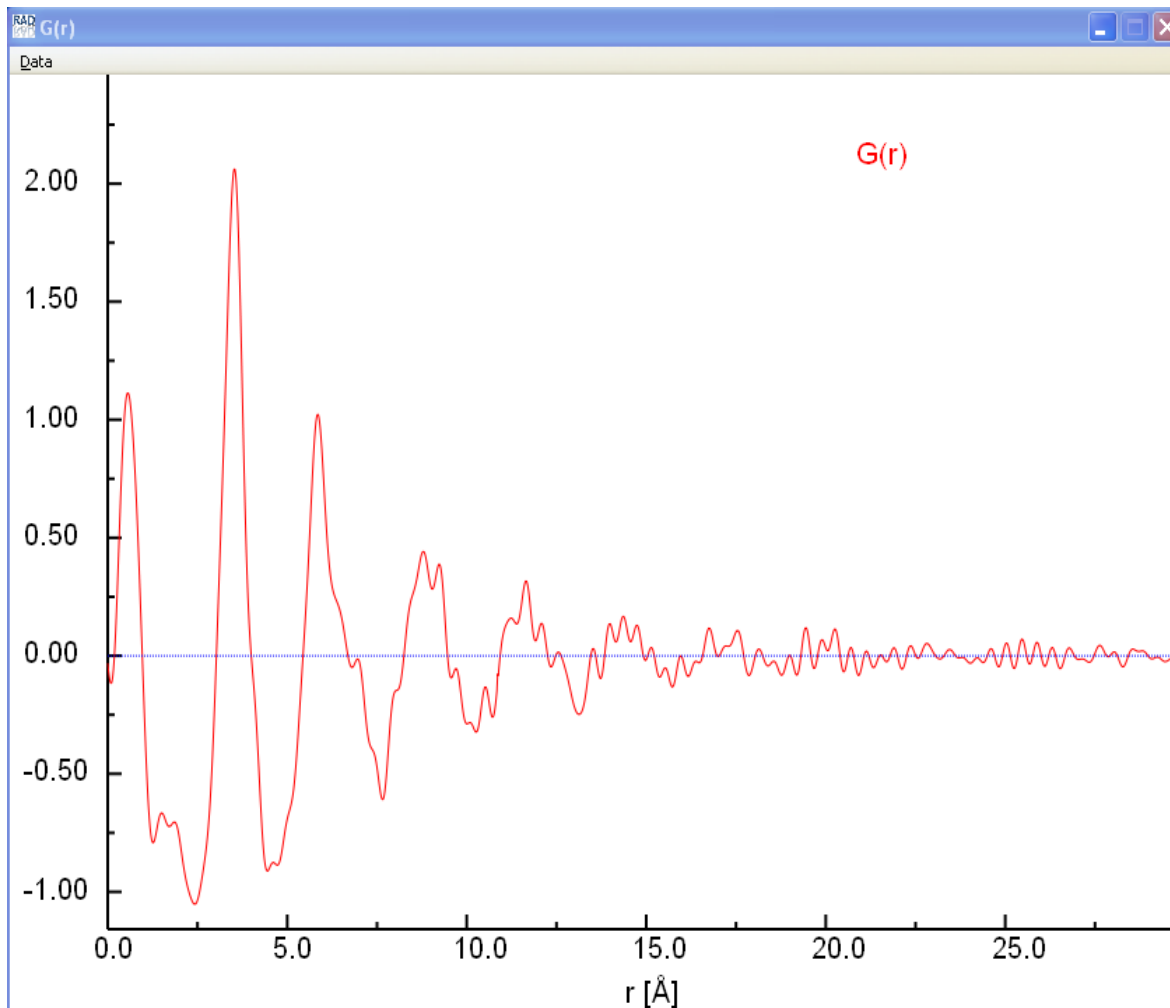
To do it the user should activate the option “*RDF G(r) calculation*” from the drop-down menu list of “*Data processing*” RAD-Gtk window (see above) and enter the name of the file containing the $q[S(q) - 1]$ data: (file *GdAl.qsq* in our example, see below).



RAD reads the data file and reports that it has 543 data points, the last one being at $Q_{\max} = 16.802 \text{ \AA}^{-1}$. Then we /the user tell(s) RAD to compute $G(r)$ up to 25 \AA in steps of 0.02 \AA and use a moderate damping factor (0.005) to outweigh higher- q data points since those are (very often) somewhat noisy. Then we/the user hit(s) “*Apply*”. A separate pop-up window appears, this time labeled $G(r)/g(r)$ in the upper left corner (see below).



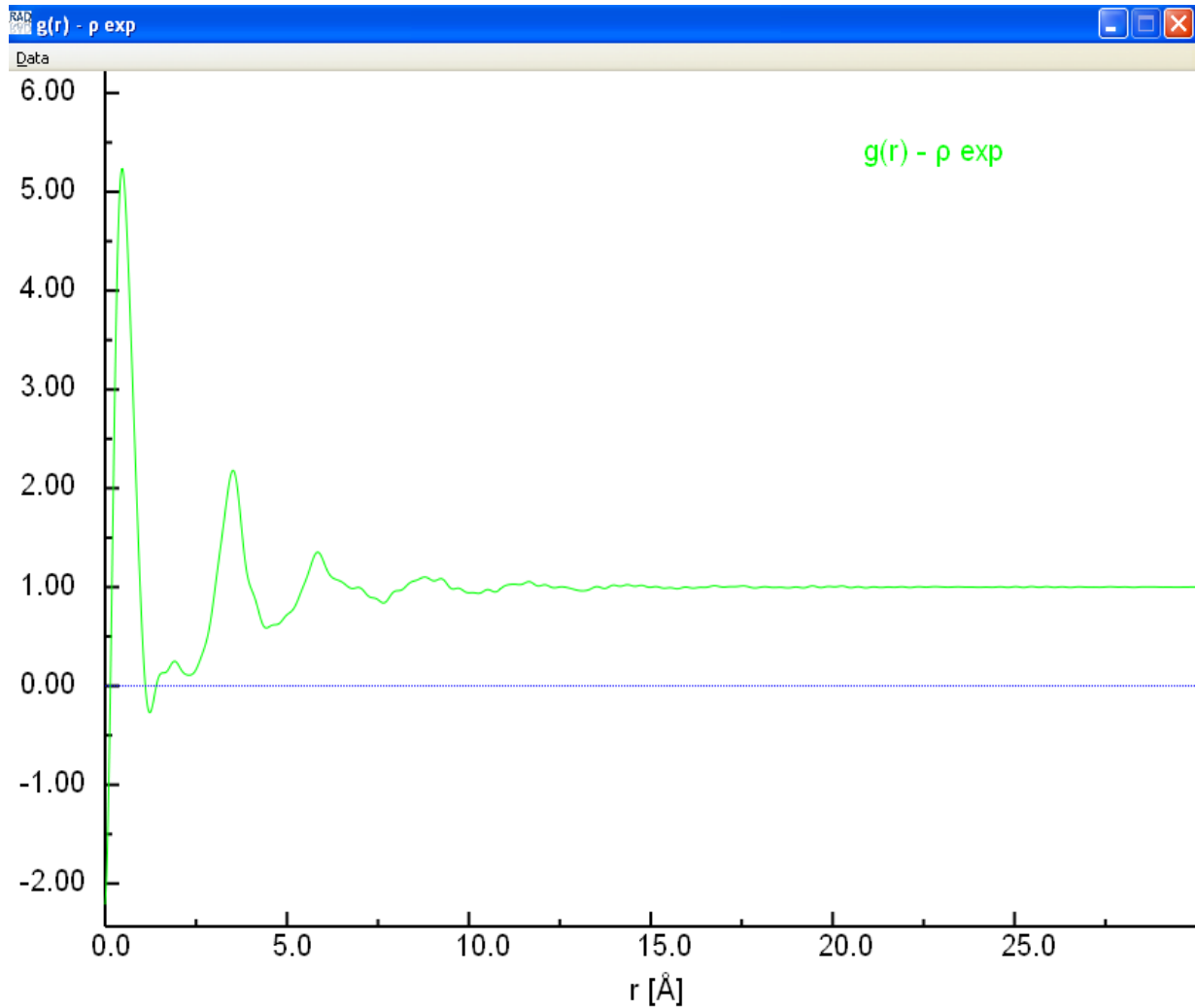
If the user decides to plot/view the computed $G(r)$ or/and $g(r)$ he/she should check the corresponding box(es) on that window. In this example we chose to plot $G(r)$ (see below).



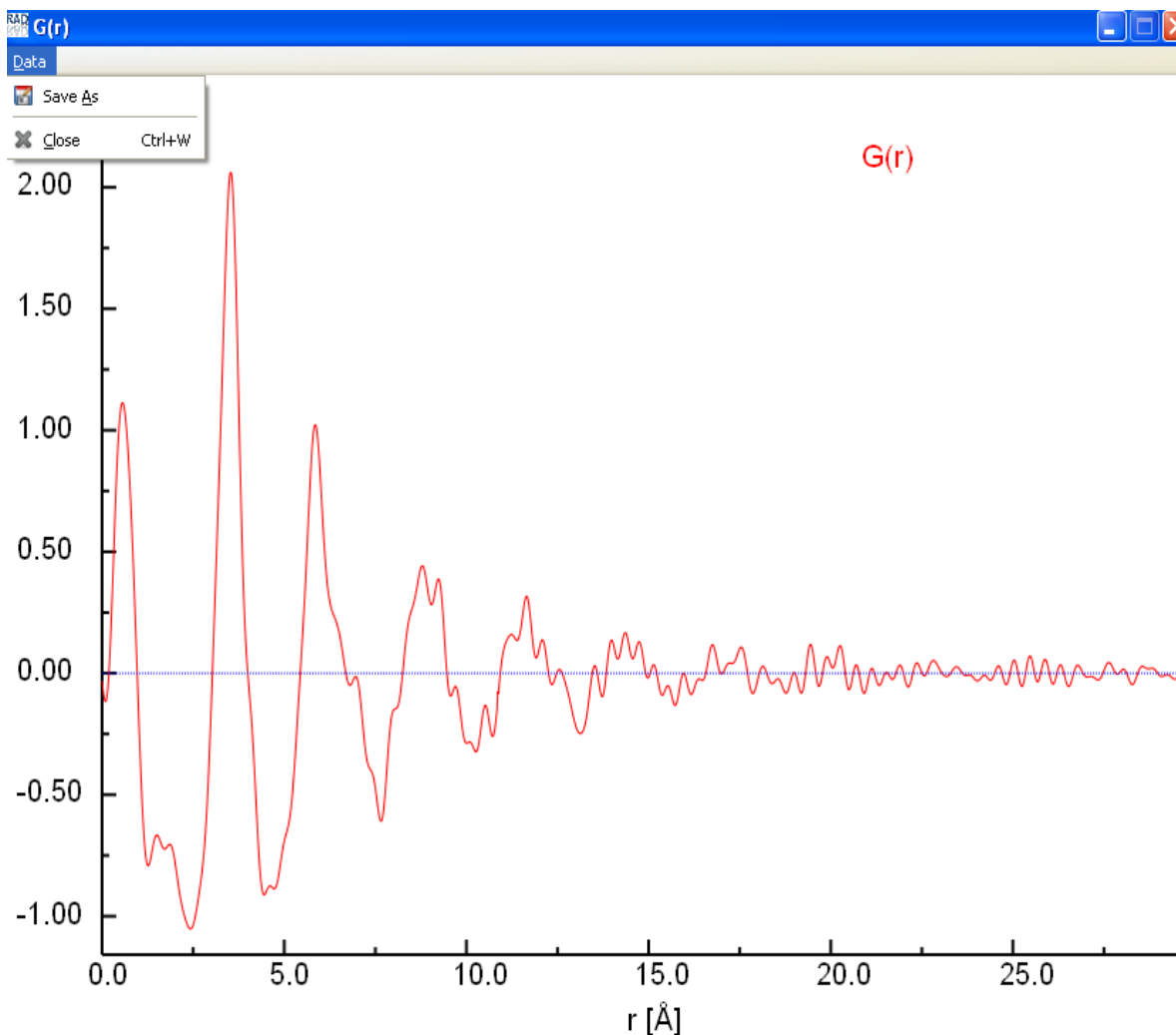
This PDF/RDF $G(r)$ shows a strong unphysical ripple close to $r \sim 0 \text{ \AA}$ but, in general, is of pretty good quality for a PDF/RDF obtained on an in-house XRD equipment back in 1988 ! The $G(r)$ has its first physically sensible peak positioned at about 3.5 \AA (Gd-Gd first atom neighbor distance) and shows physical oscillations up to about $15\text{-}20 \text{ \AA}$. This real-space distance may be viewed as a length of structural coherence in the bulk metallic glasses studied. The high-frequency ripples above 20 \AA are data noise.

Here the user has an option to compute the so-called pair correlation function $g(r)$ as well. He/she may use either the “experimental” value for the atomic number density ρ_0 stored

in the “*RAD project file*” (usually a more correct approach) or use an estimate for ρ_0 computed after the low-r slope of $G(r)$ [2,3]. The latter option is activated by checking the corresponding box in the “*Radial distribution function calculation window*”.



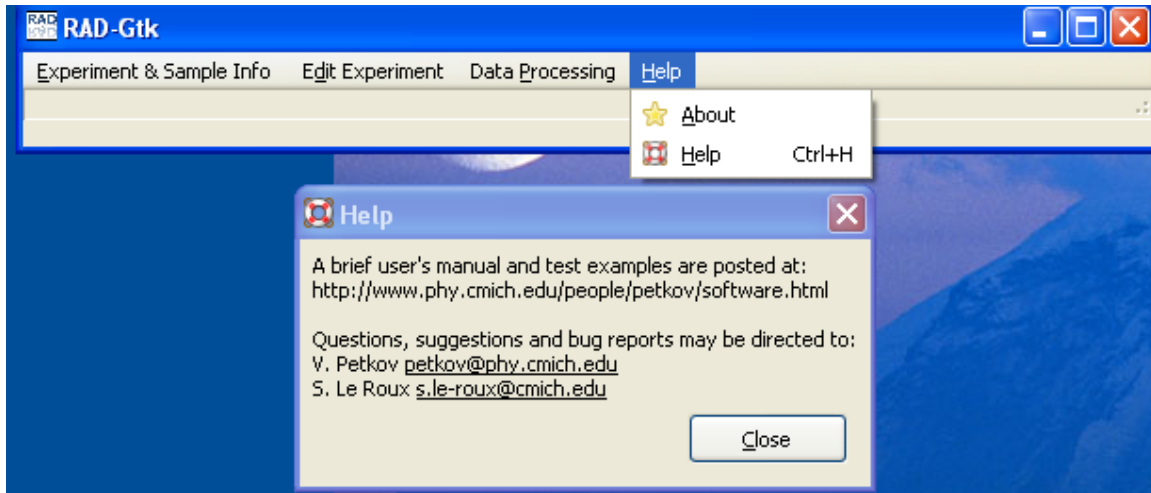
A $g(r)$ computed using the experimental value of $\rho_0 = 0.039200$ atoms/Å we entered in the *RAD project file* is shown above. This $g(r)$ shows a strong unphysical peak at distances below 1 Å but, otherwise, is of pretty good quality. Note, as it should be, $g(r)$ oscillates around one while the corresponding $G(r)$ – around zero (see the plot below)



By checking the “*Data*” option in the upper left corner in the $G(r)$ data plot window (see above) the user can save the data shown in this window in (x,y ascii) or (x,y,0,1 ascii) format. **Note, the only way to save RAD’s computed quantities (i.e. $I(q)$, $S(q)$, $q(S(q)-1)$, $G(r)$ or $g(r)$) is i) first to display the respective quantity in the *Data plotting window*, ii) view it iii) and, if satisfied, save it using the “*Save As*” option. RAD will NOT save anything unless it is “told” to do so.**

Help option of RAD-Gtk:

Provides general and contact info about RAD and its authors (see below).

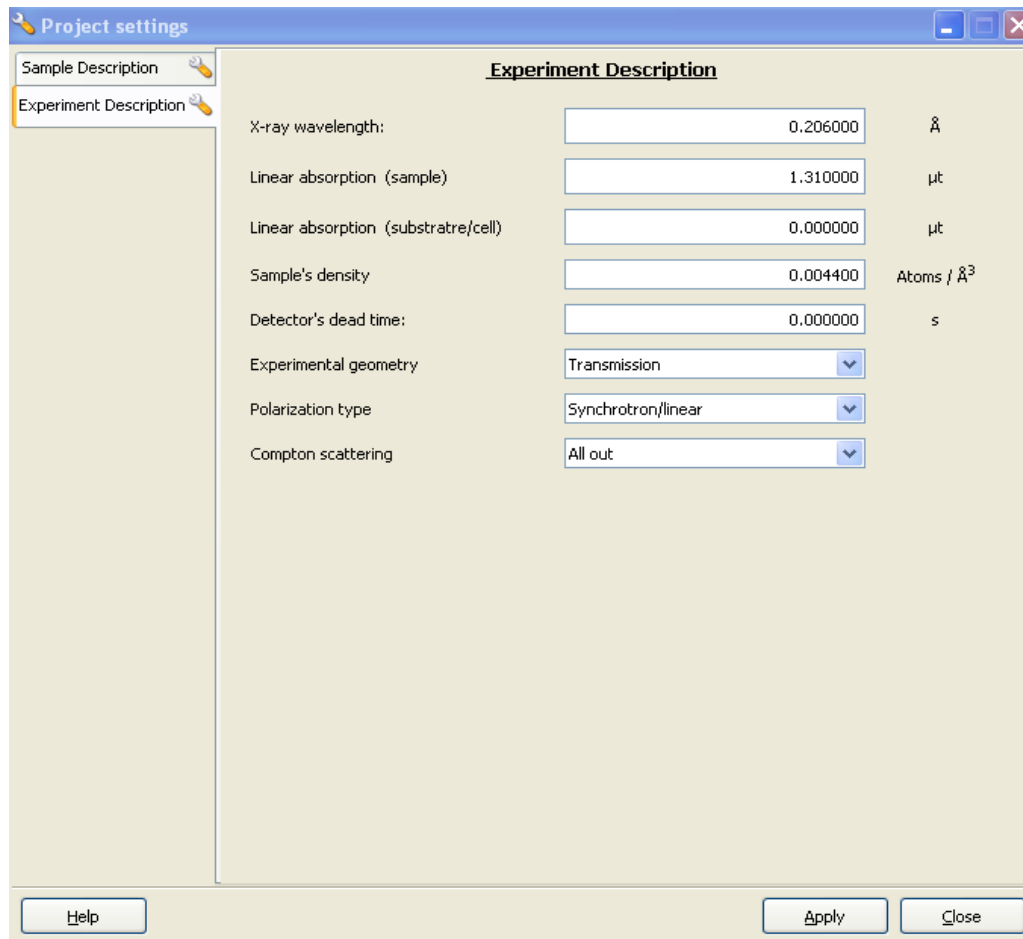


Analyzing multiple data sets (i.e. temperature, pressure etc. series):

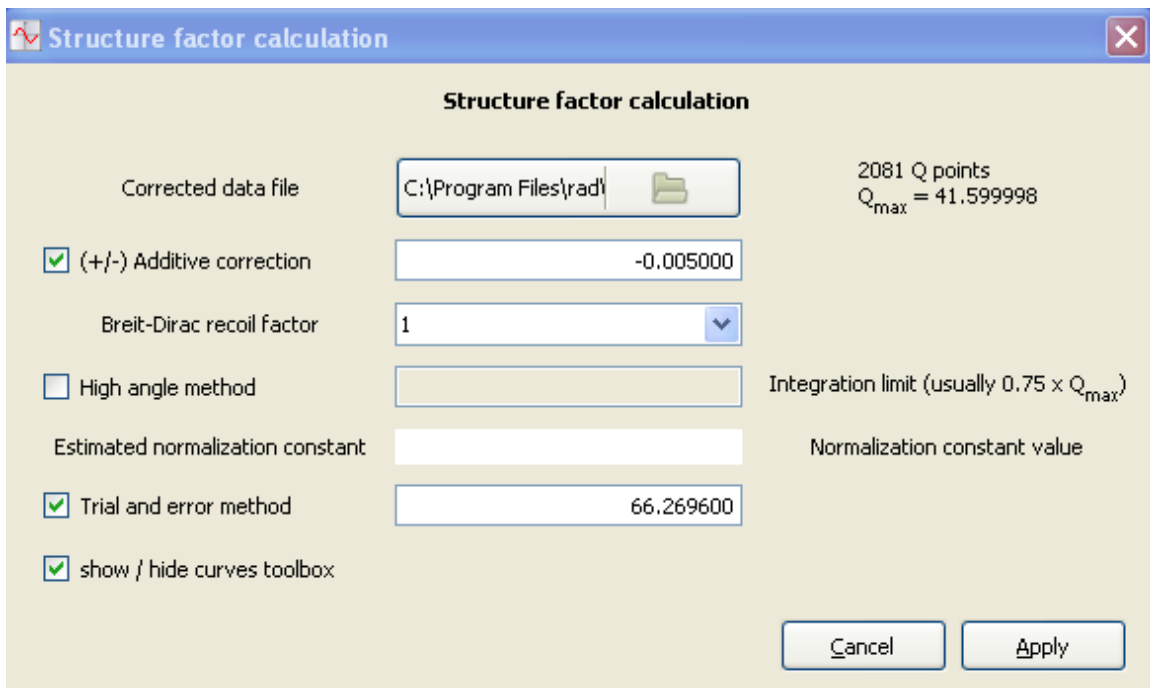
Once a RAD project file is read/created users may process, one after another, several data sets from the same sample re-using the RAD control (i.e. *Data processing*) parameters they entered/used for the first data set. Any subsequent data set (be it raw XRD data, corrected $I(q)$ data or $q(S(q)-1)$ data), however, should have the same number of data points, including the same starting and ending $2\theta/Q$ values and Δq steps as the very first data set. If not RAD may behave unpredictably.

More examples of RAD's usage:

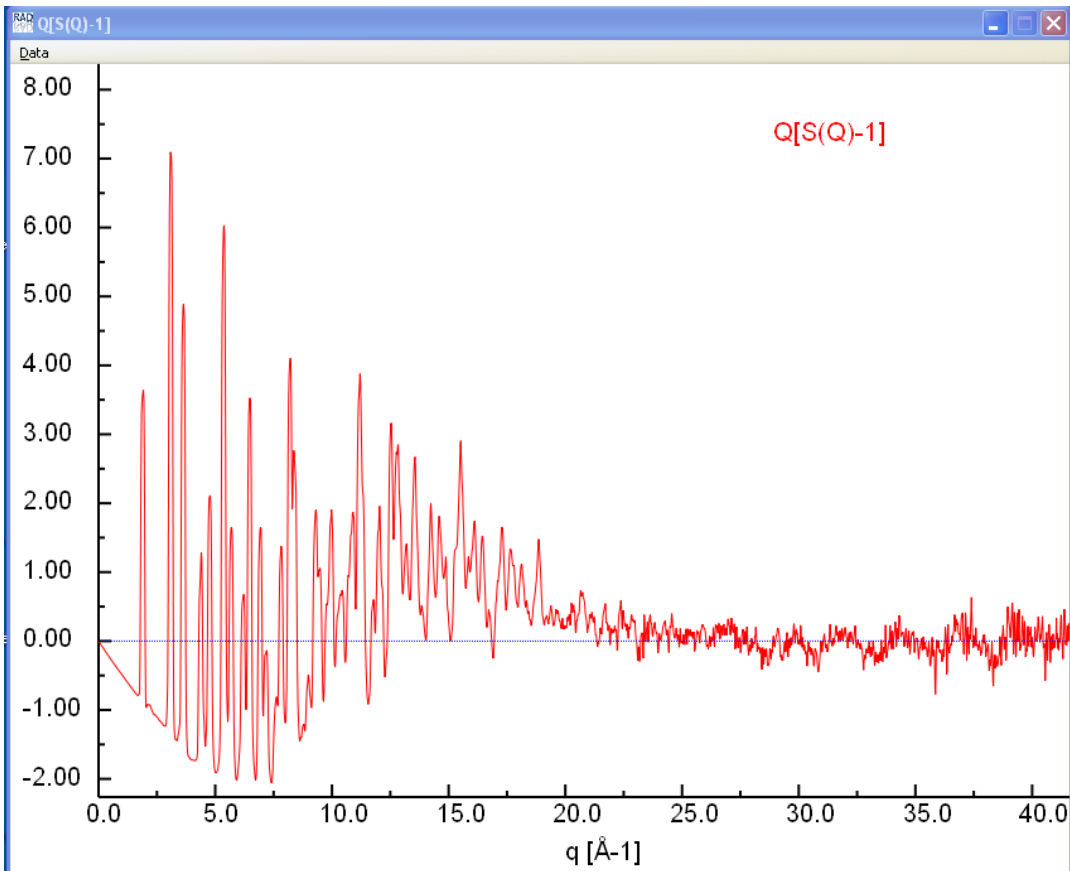
The current RAD distribution comes with two more examples. One describes processing of synchrotron XRD data for $\text{In}_{0.33}\text{Ga}_{0.67}\text{As}$ semiconductor. The study has been published in Petkov et al. *PRL* 83 (1999) p. 4089 (a copy of the paper is attached for user's convenience). Here we provide the raw experimental data: "InGaAs.th", the RAD project file: "InGaAs.rpf", the corrected XRD data: "InGaAs.cor", the reduced structure function data: "InGaAs.qsq" and the computed $G(r)$: "InGaAs.rdf". An energy sensitive (Ge solid state) detector has been used in this study which had resulted in negligible background scattering – so no data for background/air scattering are provided. Also, thanks to the usage of a Ge detector the Compton scattering has been eliminated from the



XRD data during data collection (see below that the option to be selected in such cases is Compton “*All out*”). Users may start RAD, open the existing project file: “InGaAs.rpf”, and look over the sample/experimental set-up information provide in it. Some of this info is shown in the screen-shot above. In this example the step “*Raw data corrections*” is trivial and we skip it. Here we will demonstrate the next step - the derivation of $q(S(q))$; see below. We/the user read(s) the corrected data: “InGaAs.cor” and applies a small correction to them.



The corresponding $q(S(q)-1)$ looks quite good to very high wave vectors of about 40 \AA^{-1} ; see below.



When an atomic PDF/RDF is computed from it in the way shown below:

Radial distribution function calculation

RDF calculation

Q[S(Q)-1] data file: C:\Program Files\rad\E\ [Folder icon]

2081 Q points
 $Q_{max} = 41.599998$

r_{max} value: 20.000000 Å

δr step: 0.020000 Å

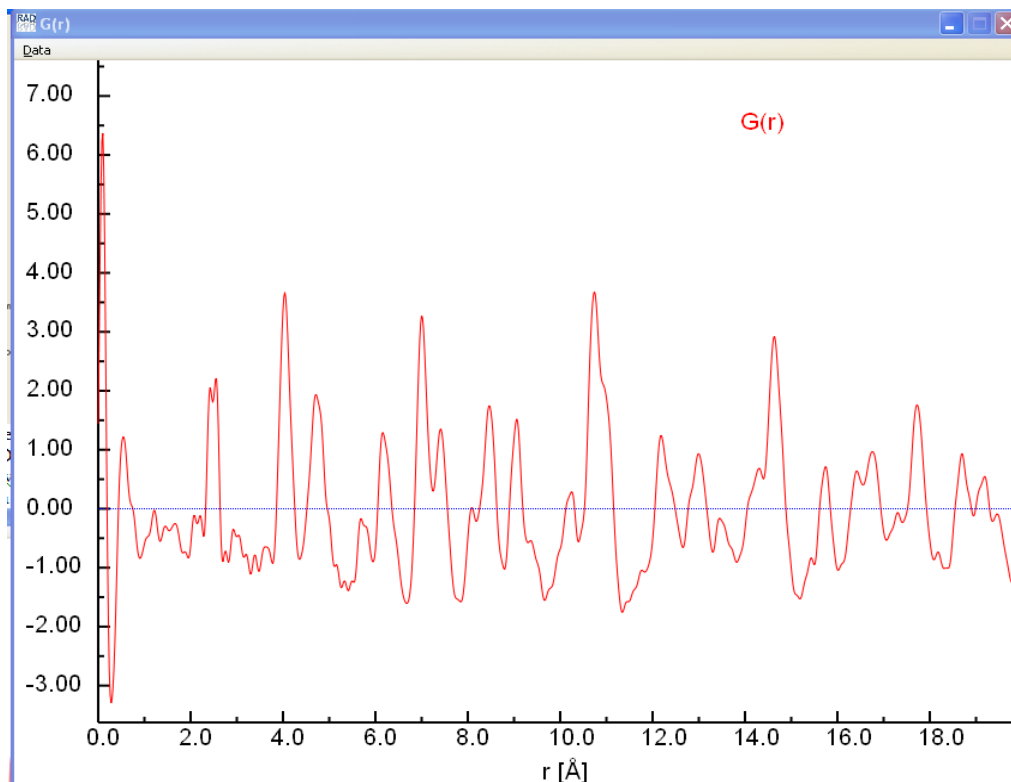
Damping factor: 0.000200 (usually 0.005)

Number density after G(r) slope [Blank field] Atoms / Å³

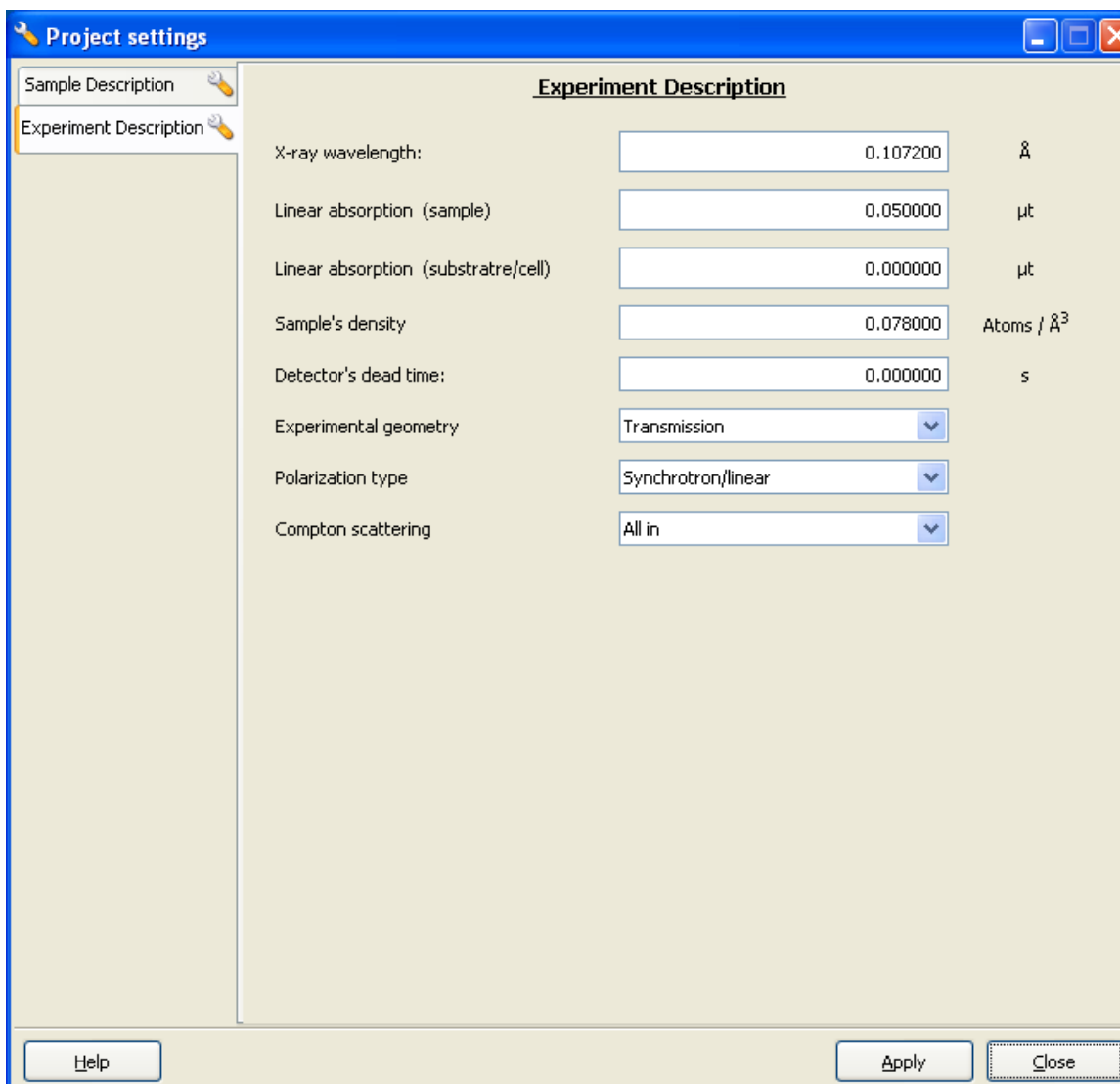
show / hide curves toolbox

Cancel Apply

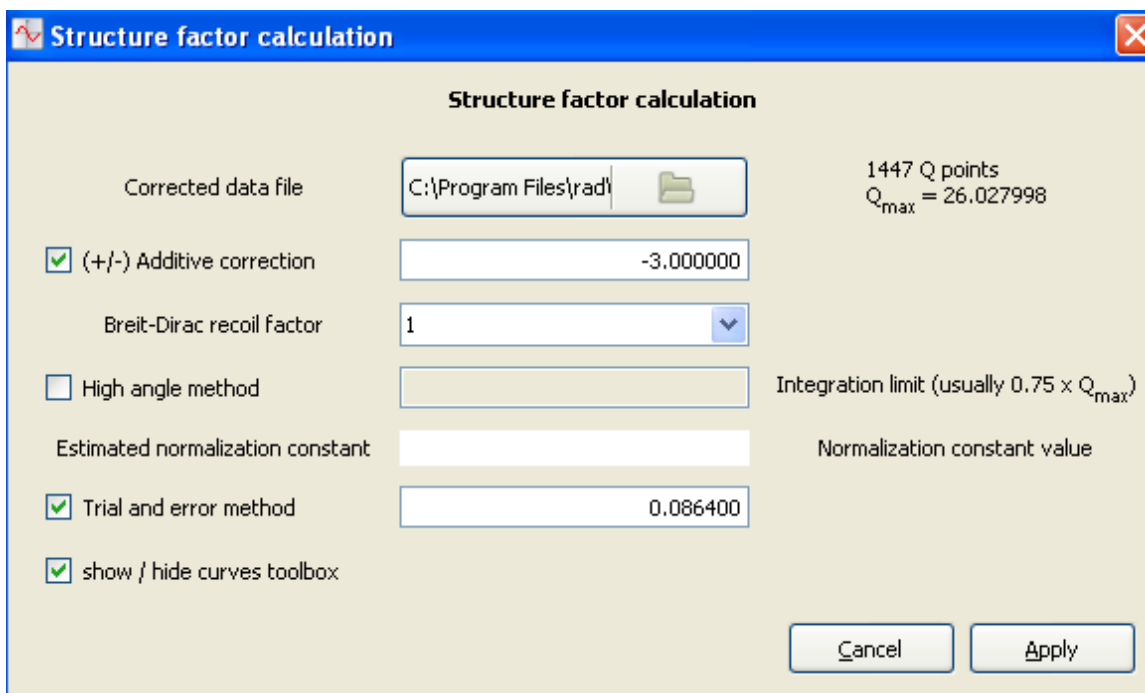
very fine structural features of $\text{In}_{0.33}\text{Ga}_{0.67}\text{As}$ can be revealed. In particular, the first PDF/RDF peak is split into two subcomponents, positioned at approx. 2.4 Å and 2.6 Å, respectively (see below). They correspond to the presence of distinct Ga-As and In-As bonds in this material.



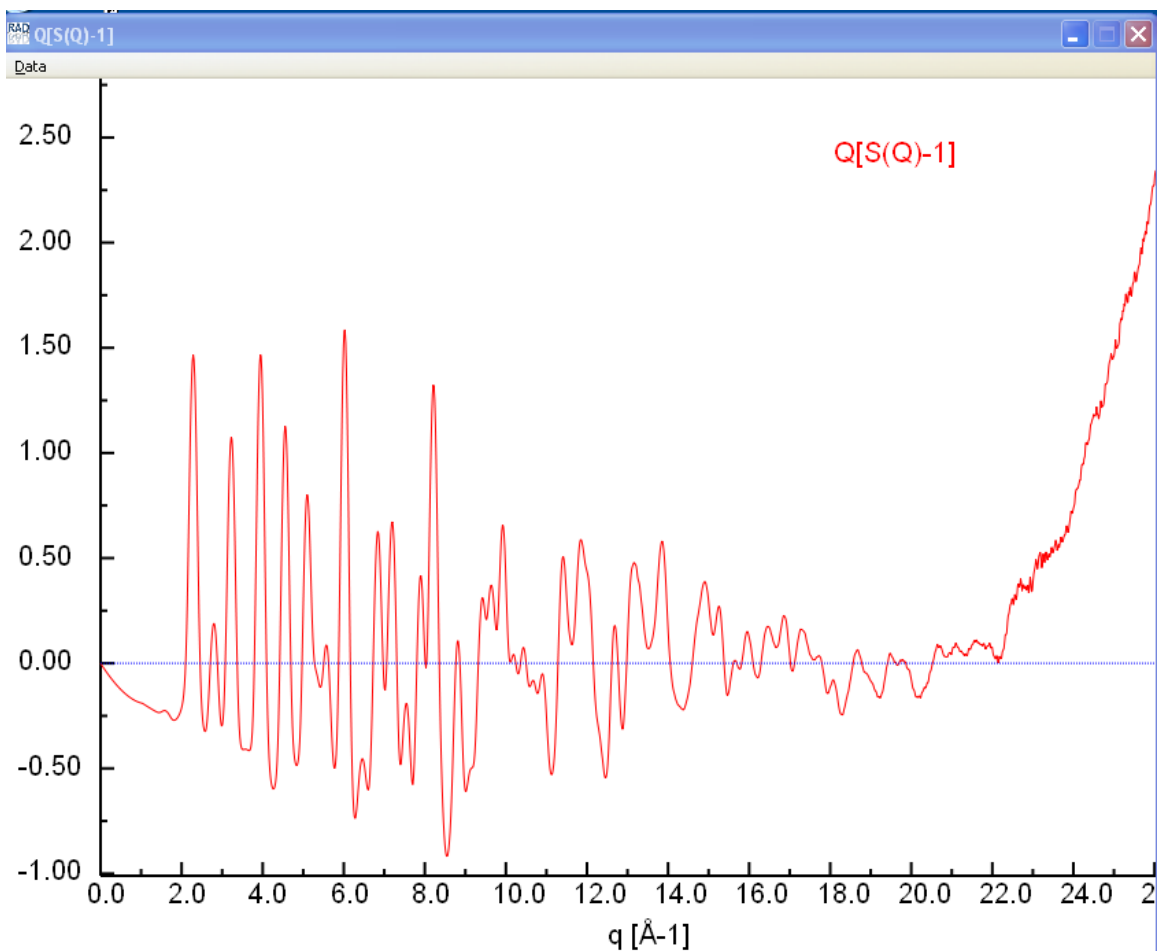
The other example highlights a processing of synchrotron XRD data for SrTiO_3 nanosized particles. The study has been published in V. Petkov et al. *Chem. Mat.* **18** (2006) p.814 (a copy of the paper is attached for user's convenience). Here we provide the raw experimental data: "SrTiO₃.th", the background scattering data: "Kapton.th", the RAD project file: "SrTiO₃.rpf", the corrected XRD data: "SrTiO₃.cor", the reduced structure function data: "SrTiO₃.qsq" and the computed G(r): "SrTiO₃.rdf". A large area (mar345) detector has been used in this study. Since large area detectors are not x-ray energy sensitive the raw XRD data contain a considerable contribution from Compton scattering (option Compton "All in"; see below).



Users may start RAD, open the existing project file: “SrTiO₃.rpf”, and look over the sample/experimental set-up information provide in it. Some of this info is shown in the screen-shot above. The step “*Raw data corrections*” is trivial and we again skip it. Here we will demonstrate the next step - the derivation of $q(S(q)-1)$; see below. We/the user read(s) the corrected data: “SrTiO₃.cor” and applies a small correction (-3) to them.



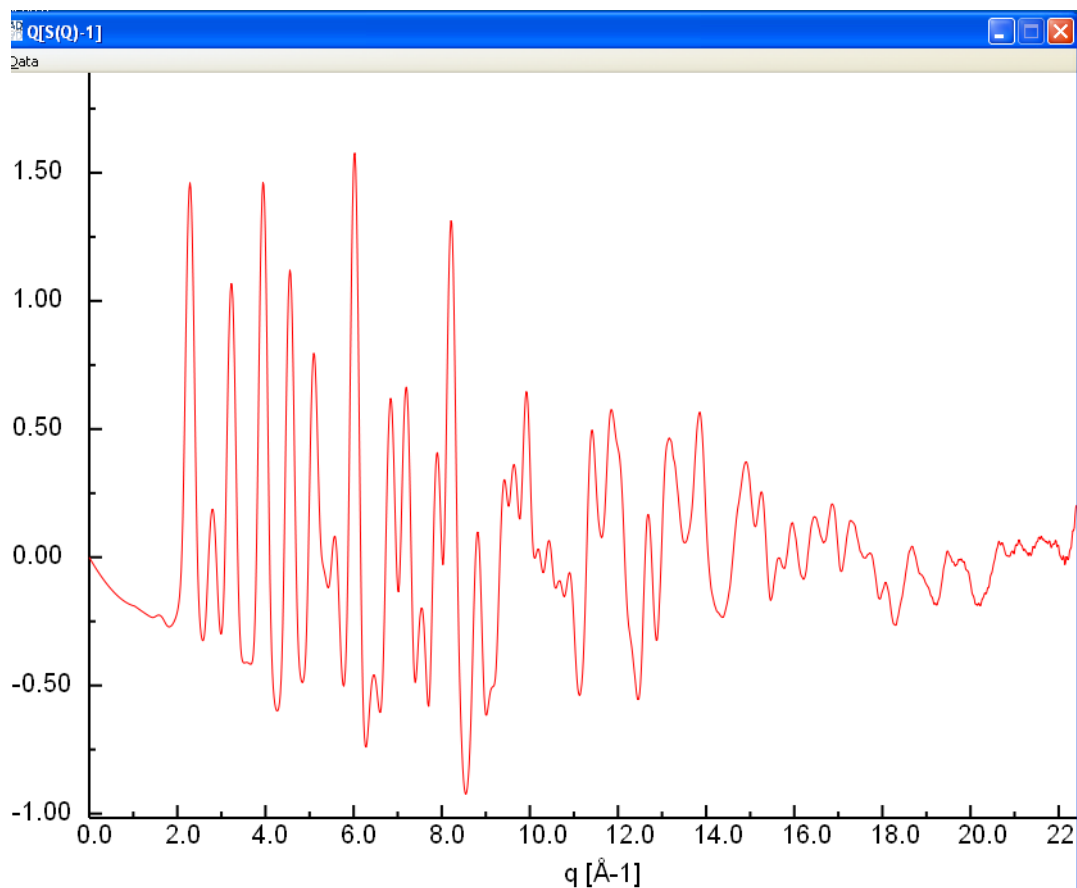
Then runs the “high-angle” normalization method first, obtains a good estimated for the normalization constant and continues in a “trial and error” mode to obtain the best normalization constant and $q(S(q)-1)$ data. Here we “find” that a small additional correction (-3) to the corrected data and a normalization constant of 0.0864 give a satisfactory result. The respective $q(S(q)-1)$ is given in the plot below. This $q(S(q)-1)$ behaves well up to q -values of about 22 \AA^{-1} but then shows an unphysical upturn, likely due to an improper Compton scattering correction. Users often may see similar unphysical behavior of their data. Possible solutions: re-do the data corrections from the very beginning, look into the sample thickness/absorption correction, background scattering, collect the data one more using another detector etc. If nothing works still save the $q(S(Q)-1)$ data.



Then open the (x,y ascii) file with any text editor and chop-off the higher-q part of the $q(S(Q)-1)$ that “misbehave”. In our case we chopped off the data above $q \sim 22.5 \text{ \AA}^{-1}$.

User’s: do NOT use distorted/misbehaving/not-oscillating around zero etc. $q(S(q)-1)$ data sets. If you still have to do it, be aware that the quality of the respective PDF/RDF data may be compromised very seriously. Do extra PDF/RDF quality checks (e.g. see [8]).

In this example we decide to use $q(S(Q)-1)$ data up to about 22.5 \AA^{-1} only; see below.



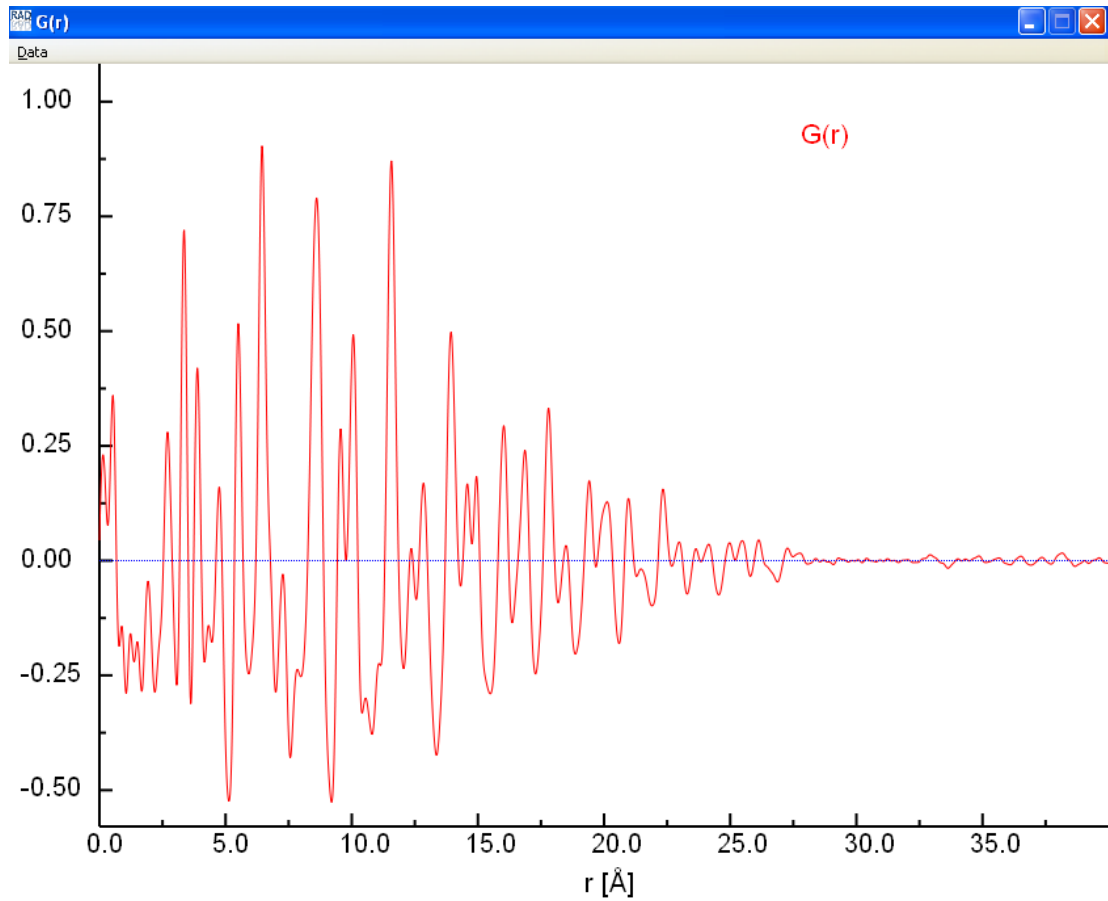
We compute the respective $G(r)$ using the parameters shown below:

The image shows a dialog box titled "Radial distribution function calculation". The main section is labeled "RDF calculation". It contains the following fields and options:

- Q[S(Q)-1] data file:** C:\Program Files\rad\E> (with a folder icon)
- r_{max} value:** 40.000000 (with unit \AA)
- δr step:** 0.020000 (with unit \AA)
- Damping factor:** 0.002500 (with note "(usually 0.005)")
- Number density after G(r) slope (with unit Atoms / \AA^3)
- show / hide curves toolbox

At the bottom right, there are "Cancel" and "Apply" buttons. The "Apply" button is highlighted.

And obtain pretty good results; see below.



The examples above are just a glimpse of what RAD users may face in real life. Indeed atomic PDF/RDF analysis is not so difficult as it looks in first sight. Sure some time and persistence are necessary to become a successful RAD user. But isn't the same with any research effort ?

Good luck !

References:

- [1] C. Giacovazzo et al., in “*Fundamentals of x-ray crystallography*”, (Oxford University Press, 1998).
- [2] H.P. Klug and L.E. Alexander, in “*X-ray diffraction procedures for polycrystalline and amorphous materials*”, (John Wiley & Sons, 1974); T. Egami and S.J.L. Billinge in “*Underneath the Bragg peaks*” (Pergamon Press, Amsterdam, **2003**); V. Petkov *Materials Today* **11** (2008) 28.
- [3] D. A. Keen *J. Appl. Cryst.* **34** (2001) 172.
- [4] B. Toby and T. Egami *Acta Cryst. A* **48** (1992) 336.
- [5] P.J. Chupas et al. *J. Appl. Cryst.* **40** (2007) 463.
- [6] V. Petkov et al. *Phys. Rev. Lett.* **83** (1999) 4089.
- [7] E. Curis and S. Benazeth, *J. Synchrotron Rad.* **7** (2000) 262.
- [8] V. Petkov and R. Danev, *J. Appl. Cryst.* **31** (1998) 609.

Appendix 2:

Dispersion corrections to the atomic scattering factors for x-rays

Definition

The history of the description of the scattering of an atom when illuminated with X-rays is that initially wavelength dependencies were ignored. This was initially referred to as 'normal scattering'. The wavelength dependencies were then corrections to the normal scattering and also called anomalous. These had to describe changes in amplitude and phase, respectively initially given the symbols $\Delta f'$ and $\Delta f''$. Thus the X-ray scattering factor of an atom is described by the equation:-

$$f = f_0 + \Delta f' + i\Delta f''$$

Below are $\Delta f'$ and $\Delta f''$ anomalous dispersion corrections for Mo K α and Ag K α radiation after D. Cromer *Acta Cryst.* **18** (1965) p. 17. Note $\Delta f'$ and $\Delta f''$ are much smaller than f_0 which is pretty close to Z, the atomic number of the respective atomic species.

Atom	CrK α_1		FeK α_1		CuK α_1		MoK α_1		AgK α_1	
	$\Delta f'$	$\Delta f''$								
NE*	0.15	0.19	0.12	0.14	0.09	0.10	0.03	0.02	0.02	0.02
NA*	0.20	0.27	0.16	0.21	0.12	0.14	0.04	0.04	0.03	0.02
MG*	0.24	0.39	0.20	0.29	0.15	0.19	0.05	0.05	0.04	0.03
AL*	0.29	0.53	0.25	0.39	0.19	0.27	0.07	0.07	0.05	0.05
SI*	0.33	0.70	0.29	0.53	0.23	0.36	0.09	0.09	0.06	0.06
P*	0.35	0.90	0.32	0.68	0.27	0.46	0.11	0.12	0.08	0.08
S*	0.36	1.15	0.35	0.86	0.31	0.58	0.13	0.16	0.09	0.10
CL*	0.32	1.42	0.36	1.07	0.33	0.72	0.15	0.19	0.11	0.13
AR*	0.27	1.76	0.36	1.32	0.36	0.89	0.18	0.24	0.13	0.16
K*	0.11	2.19	0.31	1.64	0.37	1.11	0.21	0.30	0.16	0.20
CA*	-0.16	2.64	0.21	1.98	0.36	1.34	0.24	0.36	0.18	0.24
SC*	-0.66	3.18	0.02	2.38	0.33	1.62	0.26	0.43	0.20	0.29
TI*	-1.65	3.73	-0.29	2.80	0.24	1.90	0.29	0.51	0.23	0.34
V*	-4.72	0.62	-0.84	3.29	0.10	2.23	0.31	0.60	0.25	0.40
CR	-2.28	0.71	-1.97	3.83	-0.13	2.59	0.34	0.69	0.27	0.46
MN	-1.75	0.82	-3.78	0.64	-0.50	3.00	0.36	0.80	0.30	0.54
FE	-1.47	0.94	-2.21	0.74	-1.13	3.45	0.37	0.92	0.32	0.62
CO	-1.28	1.07	-1.74	0.84	-2.51	3.95	0.37	1.06	0.34	0.71
NI	-1.15	1.19	-1.48	0.93	-3.20	0.67	0.37	1.20	0.35	0.80
CU	-1.05	1.33	-1.31	1.04	-2.15	0.75	0.36	1.36	0.36	0.91
ZN	-0.95	1.49	-1.17	1.17	-1.73	0.84	0.33	1.54	0.37	1.03
GA*	-0.84	1.74	-1.03	1.37	-1.45	0.98	0.29	1.75	0.38	1.17
GE*	-0.81	1.86	-0.97	1.46	-1.31	1.04	0.21	1.94	0.36	1.29
AS*	-0.74	2.09	-0.88	1.64	-1.17	1.17	0.12	2.17	0.35	1.45
SE*	-0.69	2.33	-0.81	1.83	-1.06	1.31	-0.02	2.42	0.32	1.61
BR*	-0.64	2.60	-0.74	2.04	-0.96	1.46	-0.21	2.68	0.27	1.79
KR*	-0.60	2.89	-0.68	2.26	-0.88	1.62	-0.47	2.96	0.21	1.98
RB	-0.58	3.23	-0.63	2.53	-0.80	1.81	-0.89	3.29	0.12	2.20
SR	-0.57	3.58	-0.59	2.80	-0.73	2.00	-1.54	3.63	-0.01	2.43
Y	-0.57	3.94	-0.56	3.08	-0.67	2.21	-2.96	4.00	-0.18	2.67
ZR	-0.60	4.31	-0.54	3.37	-0.62	2.42	-3.14	0.78	-0.41	2.93
NB	-0.66	4.78	-0.54	3.74	-0.58	2.68	-2.19	0.86	-0.73	3.22
MO	-0.72	5.16	-0.54	4.04	-0.54	2.89	-1.79	0.93	-1.22	3.51
TC*	-0.80	5.63	-0.56	4.40	-0.51	3.15	-1.55	1.02	-2.01	3.82
RU	-0.96	6.06	-0.62	4.74	-0.51	3.39	-1.37	1.09	-5.88	4.16
RH	-1.14	6.55	-0.69	5.12	-0.51	3.67	-1.24	1.18	-2.66	0.84
PD	-1.36	7.06	-0.78	5.52	-0.52	3.95	-1.13	1.27	-2.05	0.90
AG	-1.64	7.62	-0.90	5.96	-0.54	4.27	-1.03	1.37	-1.73	0.97
CD	-2.00	8.25	-1.06	6.45	-0.56	4.62	-0.95	1.49	-1.51	1.05
IN	-2.45	8.89	-1.25	6.96	-0.61	4.98	-0.88	1.60	-1.35	1.13
SN	-3.02	9.60	-1.49	7.50	-0.68	5.37	-0.81	1.73	-1.22	1.22
SB	-3.77	10.33	-1.80	8.08	-0.77	5.78	-0.75	1.86	-1.11	1.31
TE	-4.79	11.10	-2.18	8.68	-0.88	6.21	-0.69	2.00	-1.02	1.41
I	-6.35	11.94	-2.66	9.33	-1.03	6.68	-0.64	2.15	-0.94	1.52

Atom	CrK α_1		FeK α_1		CuK α_1		MoK α_1		AgK α_1	
	$\Delta f'$	$\Delta f''$								
XE*	-11.31	10.29	-3.23	9.99	-1.20	7.15	-0.59	2.30	-0.07	1.62
CS*	-10.46	11.19	-4.04	10.83	-1.40	7.75	-0.53	2.49	-0.79	1.76
BA*	-10.83	8.81	-5.14	11.60	-1.66	8.30	-0.48	2.66	-0.73	1.88
LA*	-11.76	3.55	-7.09	12.45	-2.01	8.90	-0.44	2.86	-0.67	2.02
CE	-8.96	3.82	-8.67	10.74	-2.45	9.48	-0.42	3.04	-0.62	2.15
PR*	-7.81	4.08	-10.72	8.37	-3.01	10.05	-0.40	3.22	-0.58	2.28
ND	-7.07	4.36	-10.39	8.88	-3.70	10.65	-0.39	3.42	-0.54	2.41
PM*	-6.57	4.60	-12.63	3.57	-4.55	11.22	-0.38	3.60	-0.51	2.54
SM	-6.13	4.92	-9.03	3.82	-6.02	11.92	-0.38	3.82	-0.48	2.70
EU	-5.81	5.19	-7.88	4.04	-9.89	10.17	-0.39	4.03	-0.46	2.85
GD	-5.55	5.49	-7.16	4.27	-9.18	10.72	-0.40	4.24	-0.44	3.00
TB	-5.34	5.82	-6.65	4.52	-9.31	8.27	-0.42	4.48	-0.43	3.17
DY	-5.16	6.16	-6.24	4.79	-9.83	8.73	-0.45	4.73	-0.42	3.34
HO	-5.04	6.37	-5.97	4.95	-14.04	3.51	-0.51	4.95	-0.42	3.50
ER	-4.92	6.75	-5.70	5.25	-9.27	3.73	-0.56	5.22	-0.42	3.68
TM*	-4.82	7.12	-5.49	5.54	-8.06	3.93	-0.62	5.49	-0.42	3.88
YB	-4.76	7.43	-5.33	5.78	-7.36	4.10	-0.70	5.75	-0.44	4.06
LU	-4.71	7.77	-5.18	6.04	-6.85	4.29	-0.80	6.03	-0.46	4.26
HF	-4.65	8.24	-5.04	6.40	-6.43	4.55	-0.90	6.34	-0.48	4.48
TA	-4.63	8.67	-4.92	6.74	-6.11	4.78	-1.03	6.65	-0.51	4.70
W	-4.61	9.18	-4.82	7.14	-5.83	5.07	-1.17	6.99	-0.55	4.93
RE	-4.62	9.74	-4.73	7.57	-5.58	5.37	-1.34	7.34	-0.60	5.18
OS	-4.65	10.23	-4.67	7.95	-5.39	5.64	-1.54	7.68	-0.65	5.43
IR	-4.71	10.77	-4.63	8.37	-5.22	5.94	-1.77	8.05	-0.72	5.69
PT	-4.79	11.31	-4.60	8.80	-5.08	6.24	-2.05	8.43	-0.81	5.95
AU	-4.89	12.02	-4.58	9.35	-4.93	6.63	-2.36	8.84	-0.90	6.24
HG*	-5.02	12.76	-4.57	9.92	-4.80	7.04	-2.74	9.28	-1.00	6.55
TL	-5.22	13.39	-4.62	10.41	-4.72	7.39	-3.21	9.71	-1.13	6.85
PB	-5.44	14.19	-4.66	11.03	-4.64	7.83	-3.79	10.18	-1.28	7.18
BI	-5.70	14.99	-4.73	11.65	-4.57	8.27	-4.54	10.65	-1.45	7.52
PQ*	-5.98	15.79	-4.81	12.28	-4.51	8.72	-5.70	11.16	-1.65	7.88
AT*	-6.36	16.66	-4.94	12.95	-4.47	9.19	-9.80	9.47	-1.89	8.24
RN*	-6.82	17.56	-5.11	13.65	-4.46	9.69	-9.02	9.92	-2.16	8.62
FR*	-7.38	18.56	-5.32	14.43	-4.46	10.24	-7.42	7.34	-2.49	9.03
RA	-8.14	19.50	-5.62	15.16	-4.51	10.76	-6.98	7.67	-2.87	9.42
AC*	-8.93	20.65	-5.88	16.06	-4.52	11.40	-6.89	8.04	-3.37	9.87
TH	-10.13	21.65	-6.27	16.83	-4.61	11.95	-7.18	8.38	-3.95	10.29
PA*	-11.81	22.69	-6.68	17.64	-4.70	12.52	-7.79	8.74	-4.85	10.76
U	-12.70	21.54	-7.23	18.40	-4.85	13.06	-9.19	9.09	-6.10	11.18
NP*	-14.38	22.59	-7.82	19.27	-4.99	13.68	-10.56	4.27	-7.61	9.52
PU*	-14.13	20.60	-8.57	20.04	-5.18	14.22	-8.32	4.44	-8.04	6.89
AM*	-14.16	21.49	-9.57	20.91	-5.41	14.84	-7.42	4.64	-6.71	7.16
CM*	-14.78	22.50	-11.24	21.87	-5.68	15.53	-6.84	4.85	-6.33	7.46
BK*	-15.75	23.42	-12.09	20.77	-6.00	16.17	-6.44	5.05	-6.24	7.74
CF*	-17.14	24.57	-13.68	21.62	-6.38	16.83	-6.12	5.26	-6.33	8.04

Appendix 3: Atomic Number density definition

ATOMIC NUMBER DENSITY

Number of Atoms (n) and Number Density (N)

The number of atoms or molecules (n) in a mass (m) of a pure material having atomic or molecular weight (M) is easily computed from the following equation using Avogadro's number ($N_{Av} = 6.022 \times 10^{23}$ atoms or molecules per gram-mole):

$$n = \frac{m N_{Av}}{M} \quad (1)$$

In some situations, the *atomic number density* (N), which is the concentration of atoms or molecules per unit volume (V), is an easier quantity to find when the density (ρ) is given

$$N = \frac{n}{V} = \frac{\rho N_{Av}}{M} \quad (2)$$

Number Density for Compounds

For a chemical compound (mixture) Z , which is composed of elements X and Y , the number (atom) density of the compound is calculated from

$$N_Z = N_{mix} = \frac{\rho_{mix} N_{Av}}{M_{mix}} \quad (3)$$

In some cases, the desired quantity is the number density of the compound constituents. Specifically, if $Z = X_p Y_q$, then there are p atoms of X and q atoms of Y for every molecule of Z ; hence

$$\begin{aligned} N_X &= p N_Z \\ N_Y &= q N_Z \end{aligned} \quad (4)$$

Example: Calculate the number density of natural uranium in UO_2 with $\rho_{UO_2} = 10.5 \text{ g/cm}^3$.

$$N_U = N_{UO_2} = \frac{\rho_{UO_2} N_{Av}}{M_{UO_2}} = \frac{(10.5 \text{ g/cm}^3)(6.022 \times 10^{23} \text{ atoms/mol})}{[238.0289 + 2(15.9994)] \text{ g/mol}} = 2.34 \times 10^{22} \text{ atoms/cm}^3$$

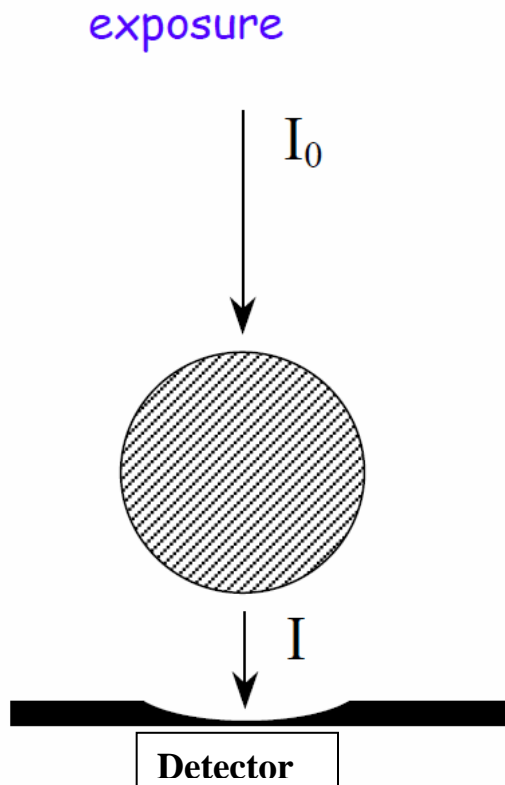
Appendix 4: Linear absorption factor μt definition

When passing through a material with a linear absorption coefficient, μ , and thickness, t , x-rays get attenuated/absorbed. The process can be quantified as follows:

$$I(\text{passed through sample}) = I_0(\text{before sample}) \cdot \exp(-\mu t)$$

By measuring I and I_0 (see below) the linear absorption factor can be obtained from

$$\mu t = -\ln(I/I_0)$$



Attachments:

VP's papers featuring RAD and examples of RAD usage illustrated in this User's manual.

Machine Computation	(a)	(b (i))	(b (ii))	(b (iii))	(c)
FMLS	2:53	1:25	4:15	4:05	12:20
BDLS	1:17	0:46	2:10	2:21	5:02
DMAP	0:55	0:43	2:17	2:10	4:52

The Weitek 3167 coprocessor is twice as fast as the 80387 and the IBM version on a 3090/200 is more than 20 times as fast as the VAX version.

References

- BROWN, I. D. (1983). *Acta Cryst.* **A39**, 216–224.
- GABE, E. J. (1988). *Crystallographic Computing* 4, edited by N. W. ISAACS & M. R. TAYLOR, pp. 381–392. Oxford Univ. Press/IUCr.
- GABE, E. J. & LEE, F. L. (1981). *Acta Cryst.* **A37**, C339.
- GABE, E. J., LEE, F. L. & LE PAGE, Y. (1985). *Crystallographic Computing* 3, edited by G. M. SHELDRICK, C. KRÜGER & R. GODDARD, pp. 167–174. Oxford: Clarendon Press.
- JOHNSON, C. K. (1971). *ORTEPII*. Report ORNL-3794, revised. Oak Ridge National Laboratory, Tennessee, USA.
- LARSON, A. C. (1969). *Acta Cryst.* **A25**, S1.
- LARSON, A. C. & GABE, E. J. (1978). *Computing in Crystallography*, edited by H. SCHENK, R. OLTHOF-HAZEKAMP, H. VAN KONINGSVELD & G. C. BASSI, pp. 81–89. Delft Univ. Press.
- LE PAGE, Y. (1982). *J. Appl. Cryst.* **15**, 255–259.
- LE PAGE, Y. (1987). *J. Appl. Cryst.* **20**, 264–269.
- LE PAGE, Y. (1988). *J. Appl. Cryst.* **21**, 983–984.
- LE PAGE, Y. & GABE, E. J. (1979). *J. Appl. Cryst.* **12**, 464–466.
- MAGUIRE, M. (1982). *Int. J. Man Mach. Stud.* **16**, 237.
- MAIN, P., FISKE, S. J., HULL, S. E., LESSINGER, L., GERMAIN, G., DECLERCQ, J.-P. & WOLFSON, M. M. (1980). *MULTAN80. A System of Computer Programs for the Automatic Solution of Crystal Structures from X-ray Diffraction Data*. Univs. of York, England, and Louvain, Belgium.
- MOTHERWELL, W. D. S. & CLEGG, W. (1978). *PLUTO*. Program for plotting molecular and crystal structures. Univ. of Cambridge, England.

J. Appl. Cryst. (1989). **22**, 387–389

RAD, a program for analysis of X-ray diffraction data from amorphous materials for personal computers. By V. PETKOV, *Sofia University, Department of Solid State Physics, Sofia-1126, Bulgaria*

(Received 21 May 1988; accepted 10 February 1989)

Abstract

RAD is an interactive computer program for radial distribution analysis of X-ray diffraction data from amorphous materials. *RAD* has been written in Fortran 77 and runs on IBM PC/XT/AT or compatible computers.

1. Introduction

The radial distribution function $4\pi r^2 \rho(r)$ (RDF) is used to characterize amorphous structures. It represents the number of atoms in a spherical shell of radius r and unit thickness. The function is zero for values of r less than the hard-sphere diameter of the atoms and modulates about $4\pi r^2 \rho_0$ for larger values of r , where ρ_0 is the average atomic density of the amorphous material. Peaks in the RDF(r) indicate frequently occurring atom–atom distances; the area under a peak is equal to the average number of atom pairs within a particular range of distances (Klug & Alexander, 1954).

The reduced RDF, $G(r) = 4\pi r[\rho(r) - \rho_0]$, is associated by a Fourier transformation with the interference function $i(s)$, which is the structure-dependent part of the experimental X-ray diffraction data. In the program *RAD* the interference function is defined, following Pings & Waser (1968), as

$$i(s) = \left[I_a^{\text{coh}}(s) - \sum_{i=1}^n x_i f_i^2(s) \right] / \left[\sum_{i=1}^n x_i f_i(s) \right]^2 \quad (1)$$

where $s = 4\pi(\sin \theta)/\lambda$, 2θ is the scattering angle, λ the

wavelength, f_i are the atomic scattering factors, x_i the molar fractions of components, n the number of atomic species, and $I_a^{\text{coh}}(s)$ is the coherently scattered intensity in electron units.

The aim of the radial distribution analysis is to evaluate the RDF(r) as the Fourier transform of the $i(s)$, which in turn can be obtained from the experimental intensities $I(s)$. The total scattered intensity $I(s)$ is related to $I_a^{\text{coh}}(s)$ (Wagner, 1969a), neglecting the small-angle and multiple scattering, by

$$I_a^{\text{coh}}(s) = \beta [I(s) - I_b(s)] / [P(s)A(s)] - M(s)I_a^{\text{inc}}(s) \quad (2)$$

where β is an unknown normalization constant, $I_b(s)$ is the background scattering (from air, substrate etc.), $P(s)$ and $A(s)$ are the appropriate polarization and absorption factors respectively, $M(s)$ is the monochromator attenuation function, and $I_a^{\text{inc}}(s)$ is the incoherent scattering in electron units scaled to one structural unit.

2. Outline of the program

The program consists of a main part and four subroutines (*SETUPD*, *DATRED*, *NORM*, *CALCRD*), where separate steps in processing the experimental intensities are performed.

The main program consists of input-output and control statements corresponding to the different options.

The subroutine *SETUPD* creates the X-ray diffraction data file, which includes scattering angles and up to 750 intensity values, and a parameter data file, supplied by the user. The parameter data file includes the number of atomic species (up to ten) constituting the sample, the corresponding molar fractions x_i and the atomic numbers Z_i , the atomic scattering-factor coefficients (Cromer & Mann, 1968), anomalous-dispersion corrections (Cromer, 1965), the wavelength λ , the linear absorption factor of the sample, the average atomic density of the amorphous material, the counter dead time, some control flags determined from the experimental configuration (geometry and monochromatization type) and the monochromator attenuation function (Ruland, 1964). Some of the numbers (density ρ_0 for instance) are not crucial in the data processing and can be neglected in the data file.

The subroutine *DATRED* uses as input data the X-ray diffraction data file and a parameter data file. The experimental data undergo the following treatments:

- (i) Subtraction of background scattering according to Warren & Mozzi (1970) and Wagner (1969b).
- (ii) Correction for counter dead time (Klug & Alexander, 1954).
- (iii) Correction for polarization (Wagner, 1978; Thijsse, 1984) depending on the type of monochromatization.
- (iv) Correction for absorption (Wagner, 1969a) depending on the geometry.
- (v) The missing values between $2\theta = 0$ and the first experimental data are derived by linear extrapolation to the origin.
- (vi) The corrected XRD data are smoothed (Savitzky & Golay, 1964), calculated in steps of $\Delta s = 0.05$ from $s = 0$ to $s_{\max} = 4\pi(\sin \theta_{\max})/\lambda$ by means of a cubic spline interpolation and stored as a new data file.

The subroutine *NORM* uses a corrected data file from *DATRED* and the parameter data file as input. The independent coherent scattering,

$$\sum_{i=1}^n x_i f_i^2(s), \quad (3)$$

the sharpening factor,

$$\left[\sum_{i=1}^n x_i f_i(s) \right]^2, \quad (4)$$

and the incoherent scattering,

$$I_a^{\text{inc}} = (\lambda/\lambda')^2 \sum_{i=1}^n x_i Z_i (b_i s)^{a_i} / [1 + (b_i s)^{a_i}], \quad (5)$$

where a_i , b_i are semi-empirical expressions (Thijsse, 1984) and λ' is a modified wavelength, are here calculated.

The corrected X-ray diffraction data are scaled into electron units by the so-called high-angle method (Wagner, 1978):

$$\beta_{\text{HA}} = \int_{s_{\min}}^{s_{\max}} \left[\sum_{i=1}^n x_i f_i^2(s) + M(s) I_a^{\text{inc}}(s) \right] ds \times \left\{ \int_{s_{\min}}^{s_{\max}} [I(s) - I_b(s)] [P(s) A(s)]^{-1} ds \right\}^{-1}; \quad (6)$$

and the interference function $i(s)$ is calculated. As an

independent check the integral

$$\int_{s_{\min}}^{s_{\max}} s^2 i(s) ds = -2\pi^2 \rho_0 \quad (7)$$

is computed according to the so-called sum rule (Wagner, 1978). When a satisfactory normalization is reached, by varying the low limit of integration s_{\min} ($s_{\max}/2 < s_{\min} < s_{\max}$), the $i(s)$ data are stored as a new file.

The subroutine *CALCRD* uses as input an interference function data file and again the parameter data file. The reduced RDF $G(r)$ is calculated, properly damped (Klug & Alexander, 1954), as a Fourier transform of the $i(s)$:

$$G(r) = (2/\pi) \int_{s=0}^{s_{\max}} si(s) \sin(sr) \exp(-bs^2) ds, \quad (8)$$

where b is the damping factor. A straight line is fitted to the $G(r)$ in the range $r = 0-1 \text{ \AA}$ to obtain an estimate for the average atomic density ρ_0 , on the basis of the expression

$$G(r) = -4\pi\rho_0 r \quad (9)$$

which holds only for small values of r . The RDF is calculated and the reduced RDF or optionally the RDF is stored as a new data file.

Residual errors in the $i(s)$, due to incorrect normalization of the data, may introduce spurious oscillations in the corresponding $G(r)$ in the region between the origin and the first peak. In order to avoid such errors a correction may be performed by means of repeated Fourier transformations (Kaplow, Strong & Averbach, 1965) and a new extended file (up to $2s_{\max}$) with corrected $i(s)$ values may be created. This file may be used as an input data file in the subroutine *CALCRD*.

RAD has been tested using published X-ray diffraction data for silica glass (Konnert & Karle, 1973). Fig. 1 shows the agreement between $si(s)$ values computed by *RAD* and by *RADILS* (Konnert & Karle, 1973). The program *RAD* proved to be useful for analysis of X-ray diffraction data from metallic glasses (Petkov, Apostolov & Skumryev, 1989).

3. Implementation of *RAD*

RAD consists of 1500 statements written in Microsoft Fortran 77 occupying about 110 Kbyte of core memory. It runs on IBM PC/XT/AT under PC-DOS 3.1. DOS utilities

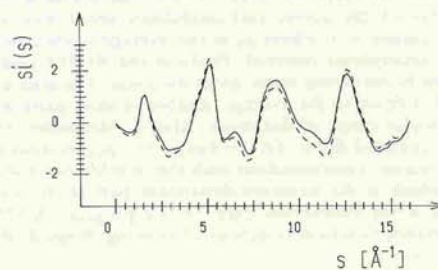


Fig. 1. Interference functions $si(s)$ for silica glass. Full line after *RAD* (multiplied by a proper constant factor because of the different sharpening factors used); broken line after *RADILS* (with permission from J. Karle).

and commands can be easily performed without leaving RAD.

During the data processing the raw data, the corrected data, the independent coherent and the incoherent scattering, the interference function $i(s)$, the reduced RDF and the RDF can be displayed by means of built-in graphic routines, if the computer is equipped with a CGA graphics card.

Fortran source code is available from the author on a floppy disk upon request.

I am indebted to Mr N. Zotov, IPM-BAN Sofia, for valuable discussions and advice.

References

- CROMER, D. T. (1965). *Acta Cryst.* **18**, 17-23.
 CROMER, D. T. & MANN, J. B. (1968). *Acta Cryst.* **A24**, 312-323.
 KAPLOW, R., STRONG, S. & AVERBACH, B. (1965). *Phys. Rev. Sect. A*, **138**, 1336-1345.
 KLUG, H. P. & ALEXANDER, L. E. (1954). *X-ray Diffraction Procedures*, p. 791. New York: Wiley.
 KONNERT, J. H. & KARLE, J. (1973). *Acta Cryst.* **A29**, 702-710.
 PETKOV, V., APOSTOLOV, A. & SKUMRYEV, V. (1989). *J. Non-Cryst. Solids*, **108**, 75-79.
 PINGS, C. J. & WASER, J. (1968). *J. Chem. Phys.* **48**, 3016-3018.
 RULAND, W. (1964). *Br. J. Appl. Phys.* **15**, 1301-1307.
 SAVITZKY, A. & GOLAY, M. J. E. (1964). *Anal. Chem.* **36**, 1627-1640.
 THIJSSSE, B. J. (1984). *J. Appl. Cryst.* **17**, 61-76.
 WAGNER, C. N. J. (1969a). *J. Vac. Sci. Tech.* **6**, 650-657.
 WAGNER, C. N. J. (1969b). *Adv. X-ray Anal.* **12**, 50-70.
 WAGNER, C. N. J. (1978). *J. Non-Cryst. Solids*, **31**, 1-40.
 WARREN, B. E. & MOZZI, R. L. (1970). *J. Appl. Cryst.* **3**, 59-65.

J. Appl. Cryst. (1989). **22**, 389-393

SIR88 – a direct-methods program for the automatic solution of crystal structures. By M. C. BURLA, Dipartimento di Scienze della Terra, Università, 06100 Perugia, Italy, M. CAMALLI, Istituto 'G. Giacomello', Area della Ricerca CNR, 00016 Montelibretti, Roma, Italy, G. CASCARANO and C. GIACOVAZZO, Dipartimento Geomineralogico, Campus Universitario, 70124 Bari, Italy, G. POLIDORI, Dipartimento di Scienze della Terra, Università, 06100 Perugia, Italy, R. SPAGNA, Istituto 'G. Giacomello', Area della Ricerca CNR, 00016 Montelibretti, Roma, Italy and D. VITERBO, Dipartimento di Chimica, Università della Calabria, 87030 Rende (Cosenza), Italy

(Received 20 January 1989; accepted 28 March 1989)

Abstract

SIR88 is an integrated package of computer programs for the solution of crystal structures. The package is based on the estimation of one- and two-phase structure seminvariants and three- and four-phase structure invariants according to the theory of representations [Giacovazzo (1977). *Acta Cryst.* **A33**, 933-944; (1980). *Acta Cryst.* **A36**, 362-372]. The program works in all the space groups and in most cases it is able to provide the correct solution without user intervention. Some prior information like the availability of a partial structure or of pseudotranslational symmetry is easily exploited to obtain the structure solution.

Introduction

The SIR (semi-invariants representations) package has been developed for solving crystal structures by direct methods. Its establishment was initiated some years ago. The present release, SIR88, is the second which we consider suitable for distribution and includes new features with respect to the previous version, SIR85. Even though SIR85 has been distributed by the authors to many laboratories worldwide over the last three years and has contributed to the determination of several difficult crystal structures, hitherto no published description of SIR has been available, except for the abstract presented at the IX ECM Meeting

(Cascarano, Giacobazzo, Burla, Nunzi, Polidori, Camalli, Spagna & Viterbo, 1985).

The theoretical basis of SIR is the theory of representations (Giacovazzo, 1977, 1980a, b) according to which, for any structure invariant or seminvariant Φ , the set of diffraction magnitudes may be arranged in a sequence of subsets in order of their expected effectiveness (in the statistical sense) for the estimation of Φ . Thus different formulas can be used for estimating a given Φ , each exploiting a different subset of diffraction magnitudes, and therefore a different amount of prior information (faster access to this subset is guaranteed by storing all the reciprocal lattice in the central memory). In SIR88 one- and two-phase seminvariants and three- and four-phase invariants are estimated according to various formulas and subsequently used in the phasing process. Symmetry is used by SIR88 in a general way, so allowing the use of phase relationships in all space groups. A further goal of SIR88 is to minimize the amount of expertise the user has to bring to solving a crystal structure. To this end all decisions concerning data manipulations or appropriate choice of parameters can be assumed by the program. Therefore scientists untrained in direct methods or experienced people prepared to trust the SIR88 default mode can often solve crystal structures without personal intervention. However a large range of options is available to experienced crystallographers for choosing their own way of solving crystal structures.

RADIAL DISTRIBUTION FUNCTIONS FOR RE_4Al_3 METALLIC GLASSES (RE = Pr, Gd, Tb, Dy)

V. PETKOV, A. APOSTOLOV and V. SKUMRYEV

Sofia University, Department of Solid State Physics, Sofia-1126, Bulgaria

Received 29 July 1988

Revised manuscript received 13 October 1988

Using X-ray diffraction the radial distribution functions for RE_4Al_3 (RE = Pr, Gd, Tb, Dy) metallic glasses have been determined. The RE-RE atomic distances and first coordination numbers have also been estimated. A structural model based on spherically arranged dense packed tetrahedra is proposed.

1. Introduction

In recent years rare earths (RE)-aluminum (Al) amorphous alloys have been of considerable interest because of their peculiar magnetic and electrical properties [1,2 and refs. therein]. For elucidation of these properties a detailed knowledge of the structure is needed as physical properties are correlated to a great extent with the local atomic arrangement. However, structure investigations have not been carried out up to now. In the present paper we report the results of a structural study of RE_4Al_3 (RE = Pr, Gd, Tb, Dy) metallic glasses.

The glassy structure is usually expressed in terms of a radial distribution function RDF (r), which represents the number of atoms in a spherical shell of radius r and unity thickness. This characterization is, however, a one-dimensional picture of the three-dimensional atomic structure. The complete structural characterization, with determination of the structural building units and their arrangement, can be derived only from a structural model with RDF (r) and average atomic density ρ in correspondence with the experimental RDF (r) and ρ .

The aim of our structural study is to obtain the RDFs for RE_4Al_3 metallic glasses by means of the X-ray diffraction (XRD) method, to analyse

them in detail and to propose an appropriate structural model on this basis. Quasi-crystalline structural models, based on randomly oriented microcrystalline regions of close-packed RE atoms, and non-crystalline structural models, based on a dense random packing of hard spheres, will be used as trial structural models since the RE_4Al_3 metallic glasses have no crystalline counterparts.

2. Experimental part

2.1. Sample preparation and characterization

The specimens were alloyed from 99.9% pure RE and Al by arc melting under an argon atmosphere. A number of ribbons - 30 μ m thick and 2 mm wide - were obtained from each master alloy through the melt-spinning technique. A number of pieces were cut from adjacent sections of the ribbons and carefully arranged onto a rectangular plastic frame using adhesive tape as a substrate to form a single layer. The layers prepared in this way were used for the XRD measurements.

The chemical composition of all samples corresponds to the overall formula $RE_{57}Al_{43}$. Electron microprobe measurements in selected areas show there are slight fluctuations in the relative RE and

Al concentration in the "wheel-quenched" and "air-quenched" ribbon sides only.

The density of the samples $\rho(\text{Pr}_4\text{Al}_3) = 5.9 \mp 0.1 \text{ g/cm}^3$, $\rho(\text{Gd}_4\text{Al}_3) = 6.6 \mp 0.1 \text{ g/cm}^3$, $\rho(\text{Tb}_4\text{Al}_3) = 6.9 \mp 0.1 \text{ g/cm}^3$, $\rho(\text{Dy}_4\text{Al}_3) = 7.1 \mp 0.1 \text{ g/cm}^3$, was measured using the Archimedes method.

2.2. X-ray diffraction measurements

The XRD data were collected by a semiautomatic powder diffractometer using filtered Mo k_α radiation and scintillation registration. Different collecting sequences were used for averaging the systematic effect of the apparatus' instability. The data were collected with the same sample several times so that at least 5000 counts were accumulated for each Bragg angle.

The linear absorption factors μt , measured by simple attenuation experiments, are of order of unity so the conditions are suitable for performing XRD measurements in symmetrical transmission geometry. As the transmission geometry has advantages in the small-angle region [3,4] but is not efficient in the high-angle region (because of the slower counting rate in comparison with the reflection) the following experimental procedure was adopted.

First, the samples were mounted in a symmetrical reflection geometry and scattered intensity collected in $\Delta 2\theta$ steps of 0.2° from $2\theta = 12^\circ$ to 60° and $\Delta 2\theta = 0.4^\circ$ from $2\theta = 60^\circ$ to 145° .

Second, the samples were positioned in symmetrical transmission geometry and measurements performed in the range from $2\theta = 7^\circ$ to 70° in steps of 0.2° .

Third, a consistency check between the transmission and the reflection data was performed [5]. If the test result were satisfactory a unique set of XRD data from $2\theta = 7^\circ$ up to 145° was composed, combining the low-angle transmission data with the high-angle reflection data, otherwise the XRD data set was rejected and the measurements repeated. This procedure ensures XRD data free from systematic errors [5,6].

The background scattering was measured with only the substrate mounted on the goniometer axis.

2.3. X-ray diffraction data processing

The raw XRD data were corrected for background scattering, counter dead time, polarization and absorption. The missing values between $2\theta = 0^\circ$ and $2\theta = 7^\circ$ have been derived by means of a linear extrapolation. The corrected data were spline smoothed, recalculated in steps of $\Delta s = 0.05$ from $s = 0$ to $s_{\text{max}} = 4\pi \sin(\theta_{\text{max}})/\lambda = 16.8 \text{ \AA}^{-1}$ and scaled into electron units by the so-called "high-angle" method. Only the coherently scattered intensity I_a^{coh} was extracted after removing the incoherent (Compton) scattering. The interference functions

$$I(s) = \left[I_a^{\text{coh}} - \sum_{i=1}^n x_i f_i^2(s) \right] / \left[\sum_{i=1}^n x_i f_i(s) \right]^2,$$

and the reduced RDFs

$$G(r) = (2/\pi) \int_{s=0}^{s_{\text{max}}} s I(s) \sin(sr) ds$$

where all symbols have the usual meaning, have been computed according to the Pings and Waser method [7].

Some residual errors in the $I(s)$, mainly occurring as a result of the incorrect normalization of the XRD data, introduce large spurious oscillations in the region between the origin and the first peak in the corresponding $G(r)$. For preventing such errors a correction was performed by means of repeated Fourier transforms in the way proposed by Kaplow, Strong and Averbach [8].

Figure 1 shows the uncorrected reduced interference function $F(s) = sI(s)$ for Gd_4Al_3 and the residual difference after the subtraction of the $F(s)$ corrected according to the method of Kaplow et al. Figure 2 shows the results of the same procedure but for the corresponding reduced RDF $G(r)$. As can be seen from these figures the change for all values of $F(s)$ is small, of the order of the data noise at high s values, but is enough to remove the ripples in the $G(r)$ at small values of r . The final interference functions $F(s)$ and the corresponding reduced RDFs $G(r)$ are shown respectively in figs. 3 and 4.

For checking the influence of the high-angle XRD data upon the final $G(r)$ values, the upper

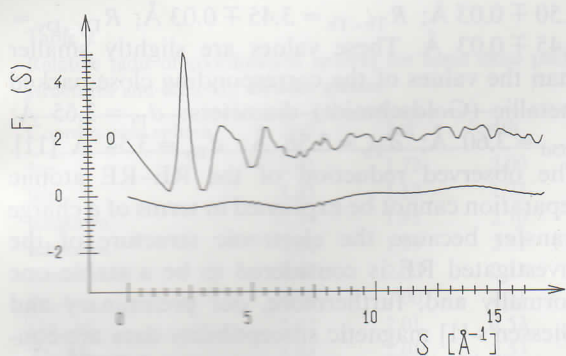


Fig. 1. The uncorrected reduced interference function $F(s)$ for Gd_4Al_3 and the residual difference after subtraction of the $F(s)$ corrected according to the method of Kaplow et al. [8].

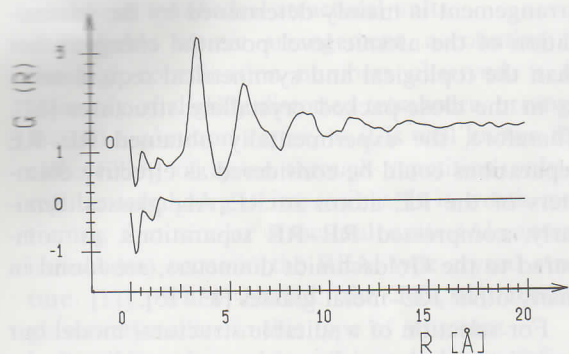


Fig. 2. The uncorrected reduced radial distribution function $G(r)$ for Gd_4Al_3 and the residual difference after the subtraction of the $G(r)$ corrected according to the method of Kaplow et al. [8].

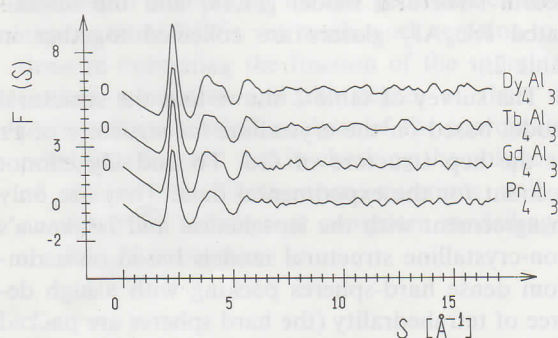


Fig. 3. Total reduced interference functions for RE_4Al_3 metallic glasses (with displaced zeroes).

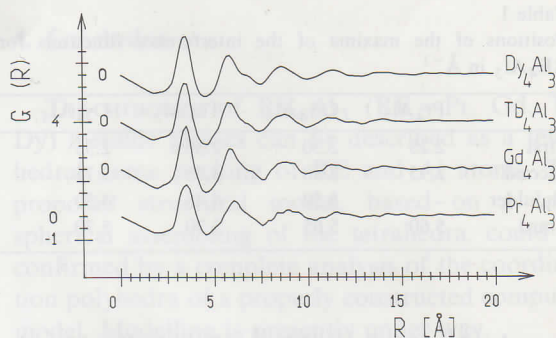


Fig. 4. Total reduced radial distribution functions for RE_4Al_3 metallic glasses (with displaced zeroes).

limit of integration s_{\max} was changed up to $s_{\max}/2$. In addition, a complementary XRD experiment was performed for the Gd_4Al_3 sample, using $Co K_{\alpha}$ radiation and Ross balanced Fe-Mn filters. However it produced no qualitative changes in the $G(r)$. Therefore, a conclusion can be drawn that all details of the $G(r)$, including the weak shoulder on the second peak near $r = 7 \text{ \AA}$ (see fig. 4), have physical meaning and the atom-atom separations and coordination numbers derived from RDFs are within the error limits stated below.

All of the above-mentioned calculations and corrections were performed on an IBM PC/XT with use of the program RAD [9].

3. Discussion

As shown in fig. 3 the $F(s)$ curves for all of the samples except Pr_4Al_3 , are composed of a sharp first maximum, second maximum with a shoulder on its large- s side and subsequent small oscillations (due to the poor XRD data statistics). The shoulder of the second $F(s)$ peak for Pr_4Al_3 is not very strong but is still clearly visible. The positions of the maxima are listed in table 1. The values obtained for Gd_4Al_3 correspond with those reported by Buschow [10].

Figure 4 shows that the features of the reduced RDFs do not vary substantially with the constituent RE elements. For all samples the correlations between the atomic positions decrease with increase of the atom-atom separations and vanish

Table 1
Positions of the maxima of the interference functions for RE₄Al₃ in Å⁻¹

	Pr ₄ Al ₃	Gd ₄ Al ₃	Tb ₄ Al ₃	Dy ₄ Al ₃
First	2.25	2.30	2.35	2.35
Second	3.95	3.80	3.75	3.75
Shoulder	–	4.50	4.45	4.50
Third	5.60	5.65	5.70	5.70

completely at about 15 Å thus indicating the existence of a short-range topological order only.

It is commonly known that for multicomponent alloys the total $G(r)$, derived from a single diffraction experiment, is a sum of the partial reduced RDFs $G_{ij}(r)$,

$$G(r) = \sum_{i,j} w_{ij} G_{ij}(r),$$

where the weighting factor w_{ij} is an appropriate average value of the weighting function $w_{ij}(s)$ which varies slowly with s [3–5].

The weighting factor of the RE–RE pairs is predominant (more than 75%) for the samples under investigation. On the contrary, the contribution of the Al–Al pairs to the experimental RDF is negligible (only about 1%). Furthermore, the individual contributions of the RE–RE and the RE–Al pairs to the first RDFs maxima are not resolved because of the insufficient resolution of the XRD experiment ($s_{\max} = 16.8 \text{ \AA}^{-1}$). Therefore, the area under the first peak of the RDFs is approximately equal to the average number of the nearest neighbours of the RE atoms, and the positions of the first maxima are strongly determined by the RE–RE separation. According to these considerations, the number of the RE nearest neighbours and the RE–RE atomic separation can be estimated on the basis of the total RDFs only.

The estimated number of RE nearest neighbours is as follows: $CN_{\text{Pr}} = 13.5 \pm 0.5$; $CN_{\text{Gd}} = 14.0 \pm 0.5$; $CN_{\text{Tb}} = 14.0 \pm 0.5$; $CN_{\text{Dy}} = 14.0 \pm 0.5$. Not surprisingly these values are high because coordination numbers higher than 12 are well known in the complex crystal structures of RE–Al alloys [11].

The estimated distances between the RE atoms are as follows: $R_{\text{Pr-Pr}} = 3.55 \pm 0.03 \text{ \AA}$; $R_{\text{Gd-Gd}} =$

$3.50 \pm 0.03 \text{ \AA}$; $R_{\text{Tb-Tb}} = 3.45 \pm 0.03 \text{ \AA}$; $R_{\text{Dy-Dy}} = 3.45 \pm 0.03 \text{ \AA}$. These values are slightly smaller than the values of the corresponding close packed metallic (Goldschmidt) diameters: $d_{\text{Pr}} = 3.65 \text{ \AA}$; $d_{\text{Gd}} = 3.60 \text{ \AA}$; $d_{\text{Tb}} = 3.56 \text{ \AA}$; $d_{\text{Dy}} = 3.54 \text{ \AA}$ [11]. The observed reduction of the RE–RE atomic separation cannot be explained in terms of a charge transfer because the electronic structure of the investigated RE is considered to be a stable one normally and, furthermore, our preliminary and Giessen's [1] magnetic susceptibility data are consistent with the magnetic moments of RE³⁺ ions only. It should be mentioned that there is a difference between the Goldschmidt diameters determined from close-packed crystalline structures and the atomic diameters determined from RDFs for metallic glasses. In the latter the local atomic arrangement is mainly determined by the minimization of the atomic level potential energy rather than the topological and symmetrical requirements as in the close-packed crystalline structures [12]. Therefore, the experimentally obtained RE–RE separations could be considered as effective diameters of the RE atoms in RE₄Al₃ glasses. Similarly, compressed RE–RE separations, as compared to the Goldschmidt diameters, are found in many other RE–metal glasses [13–15].

For selection of a suitable structural model our considerations are directed to the radii of the coordination spheres estimated by the positions of the maxima in the RDFs. In this aspect, the relative radii of the coordination spheres for hexagonal close-packed (hcp) and face-centered cubic (fcc) crystalline structures, Ichikawa's dense random packing of hard spheres [16], the icosahedral structural model [17,18] and the investigated RE₄Al₃ glasses are collected together in table 2.

The survey of table 2 shows that the structural model based on the crystalline fcc structure of Pr or the hcp structure of Gd, Tb and Dy cannot account for the experimental data. They are only in agreement with the icosahedral and Ichikawa's non-crystalline structural models based on a random dense hard-spheres packing with a high degree of tetrahedrality (the hard spheres are packed in such a way that all holes have tetrahedral symmetry). This means that the metal atoms in

Table 2
Relative radii of coordination spheres for some close packed structures and RE₄Al₃ metallic glasses

Coordination sphere	2nd	3rd	4th
fcc	1.41	1.73	2.00
hcp	1.41	1.63	1.73
Ichikawa ⁺	1.74	1.95	2.70
Ichikawa ⁺⁺	1.66	1.99	2.52
Icosahedral	1.67	2.00	2.53
Pr ₄ Al ₃	1.70	2.00	2.51
Gd ₄ Al ₃	1.67	2.01	2.53
Tb ₄ Al ₃	1.68	2.01	2.53
Dy ₄ Al ₃	1.67	2.00	2.49

⁺ With a low degree of tetrahedrality.

⁺⁺ With a high degree of tetrahedrality.

RE₄Al₃ glasses are well approximated by an assembly of tetrahedral structural units.

Probable atomic arrangement, accounting for the high coordination numbers observed, is the assembly of slightly distorted tetrahedra, arranged around a common vertex, as it is well known that close filling of space through repetition only of regular tetrahedra is impossible. It is worth mentioning that similar structural units (Al-centered icosahedra) occur in the REAl-type crystal structure [11]. When heated, the RE₄Al₃ metallic glasses crystallize in this type of structure.

A similar structural model, including a definite amount of octahedra, has been proposed for Gd–Y metallic glasses by Laridjani and Sadoc [19]. There are only a few traces of octahedral structural units on the low-*r* side of the second RDF peaks of the investigated RE₄Al₃ metallic glasses (see fig. 4).

At least qualitatively, our structural model is capable of accounting for the peculiarities of the experimental RDFs yet much work remains to be done in estimating the fraction of the spherically packed tetrahedra and the degree of their distortion, for statistical analysis of the coordination polyhedra formed, and in checking the uniqueness of the model. These open questions will be answered by subsequent computer modelling of the RE₄Al₃ structure.

4. Conclusion

The structure of RE₄Al₃ (RE = Pr, Gd, Tb, Dy) metallic glasses can be described as a tetrahedral dense packing of RE and Al atoms. The proposed structural model, based on a local spherical assembling of the tetrahedra, could be confirmed by a complete analysis of the coordination polyhedra of a properly constructed computer model. Modelling is presently under way.

The authors are indebted to Mr. L. Bozukov and Mr. V. Kostadinov for their help in producing the RE₄Al₃ samples.

References

- [1] B. Giessen, A. Hines and L. Kobacoff, IEEE Trans. Magn. 16 (1980) 1203.
- [2] K. Shirakawa, K. Aoki and T. Masumoto, J. Non-Cryst. Solids 61&62 (1984) 1371.
- [3] H. Klug and L. Alexander, in: X-ray Diffraction Procedures (Wiley, New York, 1954) p. 721.
- [4] C. Wagner, J. Non-Cryst. Solids 42 (1980) 3.
- [5] B. Thijssse, J. Appl. Cryst 17 (1984) 61.
- [6] B. Thijssse and J. Sietsma, J. Non-Cryst. Solids 61&62 (1984) 361.
- [7] C. Pings and J. Waser, J. Chem. Phys. 48 (1968) 3016.
- [8] R. Kaplow, S. Strong and B. Averbach, Phys. Rev. A138 (1965) 1336.
- [9] V. Petkov, J. Appl. Cryst., in press.
- [10] K. Buschow, Sol. St. Commun. 27 (1978) 275.
- [11] W. Pearson, in: Crystal Chemistry and Physics of Metals and Alloys (Wiley, New York, 1972).
- [12] T. Egami and Y. Waseda, J. Non-Cryst. Solids 64 (1984) 113.
- [13] M. Maurer, J. Friedt and G. Krill, J. Phys. F 13 (1983) 2389.
- [14] S. Nandra and P. Grundy, J. Phys. F 7 (1977) 207.
- [15] K. Fukuda, S. Katayama, T. Katayama, A. Nukui and A. Makisima, Jap. J. Appl. Phys. 25 (1986) 1640.
- [16] T. Ichikawa, Phys. Stat. Sol. A29 (1975) 293.
- [17] J. Sadoc, J. Dixmier and A. Guinier, J. Non-Cryst. Solids 12 (1973) 46.
- [18] C. Briant and J. Burton, Phys. Stat. Sol. B85 (1978) 393.
- [19] M. Laridjani and J. Sadoc, J. de Phys. 42 (1981) 1293.

High Real-Space Resolution Measurement of the Local Structure of $\text{Ga}_{1-x}\text{In}_x\text{As}$ Using X-Ray Diffraction

V. Petkov,¹ I-K. Jeong,¹ J. S. Chung,¹ M. F. Thorpe,¹ S. Kycia,² and S. J. L. Billinge¹

¹*Department of Physics and Astronomy and Center for Fundamental Materials Research, Michigan State University, East Lansing, Michigan 48824-1116*

²*Cornell High Energy Synchrotron Source, Cornell University, Ithaca, New York 14853*

(Received 7 June 1999)

High real-space resolution atomic pair distribution functions PDFs from the alloy series $\text{Ga}_{1-x}\text{In}_x\text{As}$ have been obtained using high-energy x-ray diffraction. The first peak in the PDF is resolved as a doublet due to the presence of two nearest neighbor bond lengths, Ga-As and In-As, as previously observed using x-ray absorption fine structure. The widths of nearest, and higher, neighbor PDF peaks are analyzed by separating the broadening due to static atom displacements from the thermal motion. The PDF peak width is 5 times larger for distant atomic neighbors than for nearest neighbors. The results are in agreement with model calculations.

PACS numbers: 61.66.Dk, 61.43.Dq, 61.72.Dd

The average atomic arrangement of crystalline semiconductor alloys is usually obtained from the position and intensities of the Bragg peaks in a diffraction experiment [1], and the actual nearest neighbor and sometimes next nearest neighbor distances for various pairs of atoms by XAFS measurements [2]. In this Letter, we show how high-energy x-ray diffraction and the resulting high-resolution atomic pair distribution functions PDFs can be used for studying the local atomic arrangements in $\text{Ga}_{1-x}\text{In}_x\text{As}$ alloys. We show that the first peak in the PDFs can be resolved as a doublet and, hence, the mean position and also the widths of the Ga-As and In-As bond length distributions determined. The detailed structure in the PDF can be followed out to very large distances and the widths of the various peaks obtained. We use the concentration dependence of the peak widths to separate the broadening due to static atom displacements from the thermal broadening. At large distances the static part of the broadening is shown to be up to 5 times larger than it is for nearest neighbor pairs. Using a simple valence force field model, we get good agreement with the experimental results.

Ternary semiconductor alloys, in particular $\text{Ga}_{1-x}\text{In}_x\text{As}$, have technological significance because they allow important properties, such as band gaps, to be tuned continuously between the two end points by varying the composition x . Surprisingly, there is no complete experimental determination of the microscopic structure of these alloys. On average, both GaAs and InAs form in the zinc-blende structure where Ga or In and As atoms occupy two interpenetrating face-centered-cubic lattices and are tetrahedrally coordinated to each other [1]. However, both extended x-ray absorption fine structure (XAFS) experiments [2] and theory [3] have shown that Ga-As and In-As bonds do not take some average value but remain close to their *natural* lengths of $L_{\text{Ga-As}}^0 = 2.437 \text{ \AA}$ and $L_{\text{In-As}}^0 = 2.610 \text{ \AA}$ in the alloy. Because of the two different bond lengths present, the zinc-blende structure of $\text{Ga}_{1-x}\text{In}_x\text{As}$ alloys becomes locally distorted. A number

of authors [2–5] have proposed distorted local structures, but there have been limited experimental data available to date. The fully distorted structure is a prerequisite as an input for accurate band structure and phonon dispersion calculations [6].

The technique of choice for studying the local structure of semiconductor alloys has been XAFS [2,5]. However, XAFS provides information only about the immediate atomic ordering (first and sometimes second coordination shells) and all longer-ranged structural features remain hidden. To remedy this shortcoming, we have taken the alternative experimental approach of obtaining high-resolution PDFs of these alloys from high-energy x-ray diffraction data.

The PDF is the instantaneous atomic density-density correlation function which describes the local arrangement of atoms in a material [7]. The PDF, $G(r)$, is the sine Fourier transform of the experimentally observable total structure factor, $S(Q)$, where Q is the magnitude of the wave vector, given by

$$G(r) = \frac{2}{\pi} \int_0^{Q_{\max}} F(Q) \sin Qr dQ, \quad (1)$$

with $F(Q) = Q[S(Q) - 1]$. The total structure factor, $S(Q)$, is the normalized scattered intensity from the powder sample.

PDF analysis yields the real local structure, whereas an analysis of the Bragg scattering alone yields the average crystal structure. Determining the PDF has been the approach of choice for characterizing glasses, liquids, and amorphous materials for a long time [8]. However, its widespread application to study *crystalline* materials has been relatively recent [9]. Very high real-space resolution is required to differentiate the distinct Ga-As and In-As bond lengths present in $\text{Ga}_{1-x}\text{In}_x\text{As}$. High real-space resolution is obtained by measuring $S(Q)$ to a very high value of Q ($Q_{\max} \geq 40 \text{ \AA}^{-1}$). An indium neutron absorption resonance rules out neutron measurements in the

$\text{Ga}_{1-x}\text{In}_x\text{As}$ system. We therefore carried out x-ray powder diffraction measurements. To access Q values in the vicinity of $40\text{--}50 \text{ \AA}^{-1}$ it is necessary to use x rays with energies $\geq 50 \text{ keV}$. The experiments were carried out at the A2 24 pole wiggler beam line at Cornell High Energy Synchrotron Source (CHESS), which is capable of delivering intense x rays of energy 60 keV . Six powder samples of $\text{Ga}_{1-x}\text{In}_x\text{As}$, with $x = 0.0, 0.17, 0.5, 0.67, 0.83,$ and 1.0 , were measured. The samples were made by standard methods and the details of the sample preparation will be reported elsewhere [10]. All measurements were done in symmetric transmission geometry at 10 K . The relative intensities of the Bragg peaks compare well with those expected from the crystal structure, suggesting that the samples are free of any significant texture. Low temperature was used to minimize thermal vibration in the samples, and hence to increase the sensitivity to static atomic displacements. A double crystal Si(111) monochromator was used. Scattered radiation was collected with an intrinsic germanium detector connected to a multichannel analyzer. The elastic component was separated from the incoherent Compton scattering before data analysis [10]. Several diffraction runs were conducted with each sample, and the resulting spectra averaged to improve the statistical accuracy. The data were normalized for flux, corrected for background scattering, detector deadtime and absorption, and divided by the average form factor to obtain the total structure factor, $S(Q)$ [7,8,11], using the program RAD [10,12]. Experimental reduced structure factors, $F(Q)$, are shown in Fig. 1. The corresponding reduced PDFs, $G(r)$, are shown in Fig. 2. The data for the Fourier transform were terminated at $Q_{\text{max}} = 45 \text{ \AA}^{-1}$ beyond which the signal to noise ratio became unfavorable. This is a very high momentum transfer for x-ray diffraction measurements. For comparison, Q_{max} from a Cu K_α x-ray tube is less than 8 \AA^{-1} .

Significant Bragg scattering (well-defined peaks) are immediately evident in Fig. 1 up to $Q \sim 35 \text{ \AA}^{-1}$ in the end members, GaAs and InAs. This implies that the samples have long range order and that there is little positional disorder (dynamic or static) on the atomic scale. The Bragg peaks disappear at much lower Q values in the alloy data: the samples are still long-range ordered but they have significant local positional disorder. At high- Q values, oscillating diffuse scattering is evident. This has a period of $2\pi/2.5 \text{ \AA}^{-1}$ and contains information about the shortest atomic distances in $\text{Ga}_{1-x}\text{In}_x\text{As}$ alloys seen as a sharp first peak in $G(r)$ at 2.5 \AA (see Fig. 2). In the alloys, this peak is split into a doublet as is clearly evident in Fig. 2; with a shorter Ga-As bond and a longer In-As bond. This peak is shown on an expanded scale in the inset to Fig. 3 for all the compositions measured. We determined the positions of the two subcomponents of the first PDF peak, i.e., the mean Ga-As and In-As bond lengths, and the results are shown in Fig. 3. Also shown is the room temperature result previously obtained in the XAFS study of Mikkelsen and Boyce [2]. There is clearly good agree-

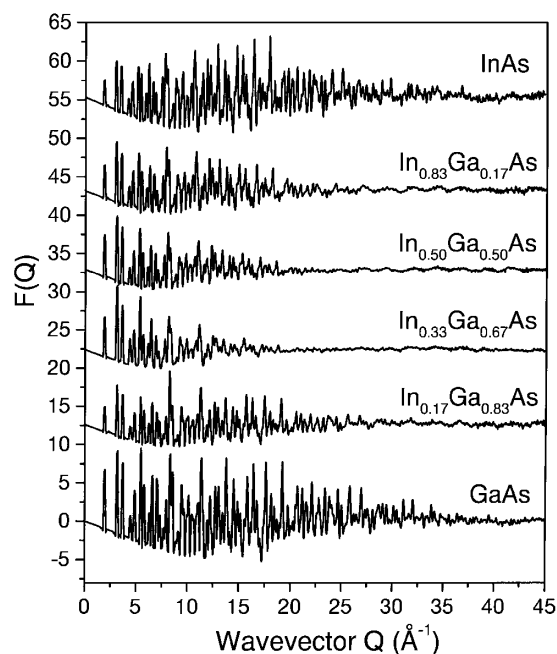


FIG. 1. The reduced structure factor, $F(Q)$, for $\text{Ga}_{1-x}\text{In}_x\text{As}$ measured at 10 K for various concentrations.

ment. The PDF-based bond lengths are shifted to smaller lengths by about 0.012 \AA since our data were measured at 10 K , whereas the XAFS experiments were at room temperature. The nearest neighbor peak is the only peak which is sharp in the experimental PDFs, as can be seen in Fig. 2. From the second-neighbor onwards the significant atomic displacements in the alloy samples result in broad atom-pair distributions without any resolvable splitting. Model calculations show that this broadening is intrinsic and not due to any experimental limitations. The PDF peak widths in $\text{Ga}_{1-x}\text{In}_x\text{As}$ were quantified by fitting individual peaks using Gaussians convoluted with sinc functions with FWHM 0.086 \AA to account for the experimental resolution coming from the finite Q_{max} . At low r this was accomplished by fitting individual peaks. At high r where there is significant peak overlap a profile fitting regression program was used [13]. The resulting mean-square Gaussian standard deviations are shown in Fig. 4. One can see that the static contribution to the PDF peak width on 2nd and higher neighbors is up to 5 times larger than on the near neighbors. The peak width has a maximum at a composition $x = 0.5$ and affects the common (As) more than the mixed (metal) sublattice.

In order to better understand these results, we have modeled to the static and thermal disorder in the alloy by using a Kirkwood potential [14]. The potential contains nearest neighbor bond stretching force constants α and force constants β that couple to the change in the angle between adjacent nearest neighbor bonds. We choose these parameters to fit the end members [3] with $\alpha_{\text{Ga-As}} = 96 \text{ N/m}$, $\alpha_{\text{In-As}} = 97 \text{ N/m}$, $\beta_{\text{Ga-As-Ga}} = \beta_{\text{As-Ga-As}} = 10 \text{ N/m}$, and

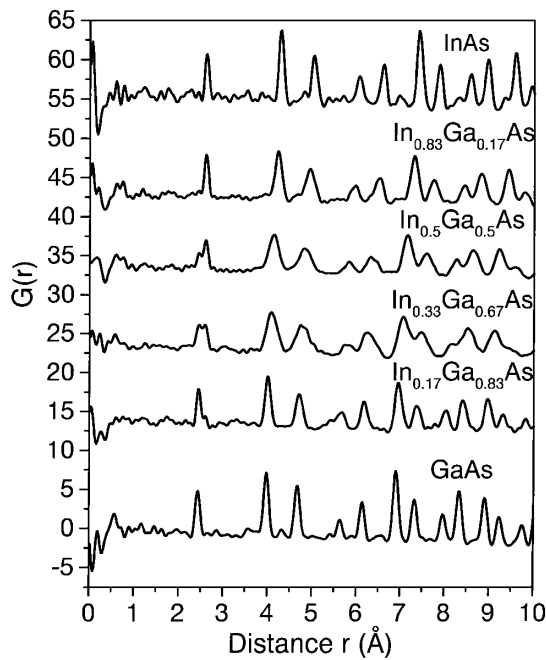


FIG. 2. The reduced PDF, $G(r)$, for $\text{Ga}_{1-x}\text{In}_x\text{As}$ measured at 10 K for various concentrations.

$\beta_{\text{In-As-In}} = \beta_{\text{As-In-As}} = 6 \text{ N/m}$. The additional angular force constant required in the alloy is taken to be the geometrical mean, so that $\beta_{\text{Ga-As-In}} = \sqrt{(\beta_{\text{Ga-As-Ga}}\beta_{\text{In-As-In}})}$. We have constructed a series of cubic 512 atom periodic supercells in which the Ga and In atoms are distributed randomly according to the composition x . The system is relaxed using the Kirkwood potential to find the displacements from the virtual crystal positions. The volume of the supercell is also adjusted to find the minimum energy. Using this strained static structure, a dynamical matrix has been constructed, and the eigenvalues and eigenvectors found numerically. From this the Debye-Waller factors for all the individual atoms in the supercell can be found and hence the PDF of the model by including the Gaussian broadening of all the subpeaks, which is the correct procedure within the harmonic approximation [15]. The model PDF is plotted with the data in the inset to Fig. 3 and in Fig. 5. The agreement at higher r is comparable to that in the r range shown. All the individual peaks shown in the figures consist of many Gaussian subpeaks. The overall fit to the experimental $G(r)$ is excellent, and the small discrepancies in Fig. 5 between theory and experiment are probably due to small residual experimental errors. Note that in comparing with experiment, the theoretical PDF has been convoluted with a sinc function to incorporate the truncation of the experimental data at $Q_{\text{max}} = 45 \text{ \AA}$. The technique discussed above could be extended using a better force constant model with more parameters, but does not seem necessary at this time.

The contributions from static displacements and thermal motion to the widths of the individual peaks in

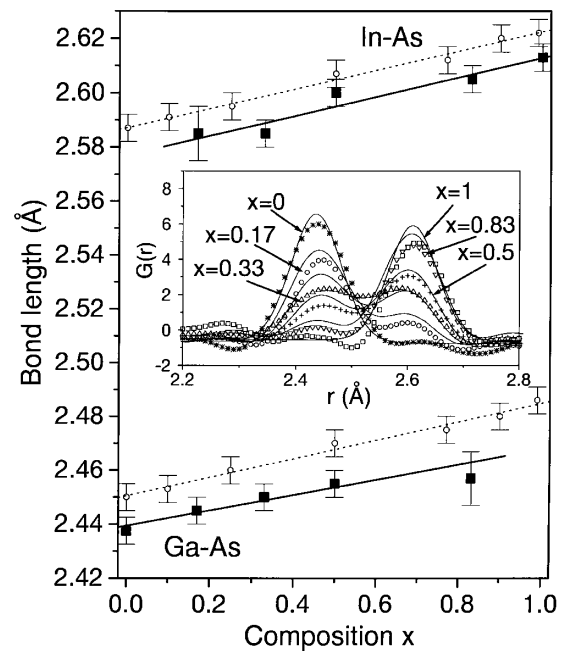


FIG. 3. Solid symbols: Ga-As and In-As bond lengths vs composition as extracted from the present PDFs. Open symbols: room-temperature XAFS results from Ref. 2. Inset: Split nearest neighbor PDF peak from the data (symbols) and the model (solid lines).

the reduced PDF act independently as expected and as confirmed by our supercell calculations described in the

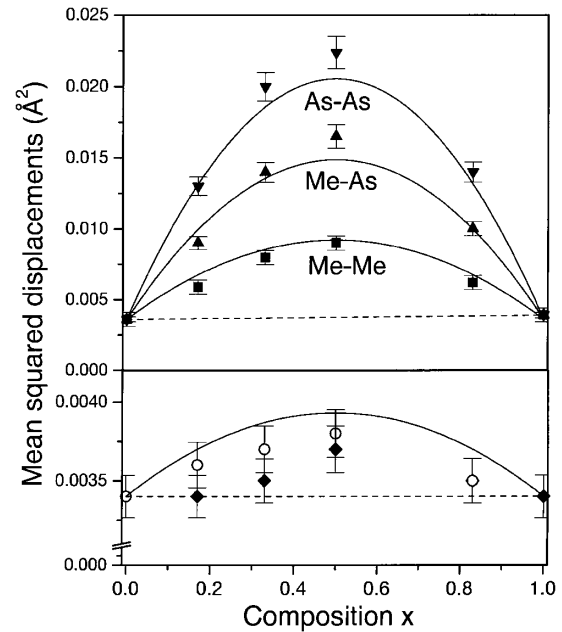


FIG. 4. Square of the PDF peak widths for far neighbors (top panel) and nearest neighbors (lower panel) separated by sublattice type. Symbols: values from the data. In the lower panel the open symbols are for the Ga-As bond and the closed symbols for the In-As bond. Solid lines: theory. See text for details. The mean-square static and thermal distortions are added. Here Me represents both the metals Ga and In, which behave in the same way. Note that the scale in the lower panel is expanded by a factor of 10 compared to the upper panel.

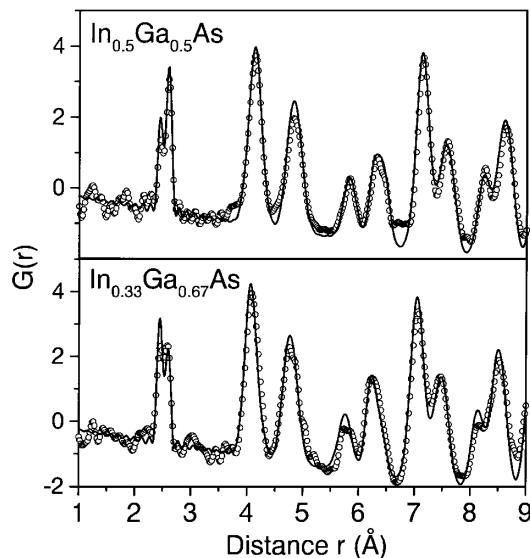


FIG. 5. Experimental (open circles) and theoretical (solid line) PDFs for $\text{Ga}_{1-x}\text{In}_x\text{As}$ for concentrations $x = 0.5$ and $x = 0.33$.

previous paragraph. We therefore expect the squared width Δ to be a sum of the two parts. The thermal part σ is almost independent of the concentration, and we fit σ^2 by a linear function of the composition x between the two end points in Fig. 4. To better understand the strain, it is convenient to assume that all the force constants are the same and independent of chemical species. Then it can be shown [16] for any such model that

$$\Delta_{ij}^2 = \sigma_{ij}^2 + A_{ij}x(1-x)(L_{\text{In-As}}^0 - L_{\text{Ga-As}}^0)^2, \quad (2)$$

where the subscripts ij refer to the two atoms that lead to a given peak in the reduced PDF. For the Kirkwood model the A_{ij} are functions of the ratio of force constants β/α only. It further turns out that the A_{ij} are independent of whether a site in one sublattice is Ga or In, so we will just refer to that as the metal site. By taking mean values from the force constants used in the simulation we find that $\beta/\alpha = 0.83$, and that for nearest neighbor pairs $A_{ij} = 0.0712$. For more distant pairs the motion of the two atoms becomes uncoupled so that $A_{ij} = A_i + A_j$, and we find that for the metal site $A_i = 0.375$ and for the As site $A_i = 1.134$. The validity of the approximation of using mean values for the force constants was shown to be accurate by calculating the model PDF for all compositions as described above and comparing to the prediction of Eq. (2) [16]. Equation (2) shows good agreement with the data for near and far neighbor PDF peaks, and for the different sublattices, over the whole alloy range, as shown in Fig. 4, using only parameters taken from fits to the end members. There

is a considerably larger width associated with the As-As peak in Fig. 4 when compared to the Me-Me peak, because the As atom is surrounded by four metal cations, providing five distinct first-neighbor environments [4,5]. The theoretical curve in the lower panel of Fig. 4 is predicted to be the same for the Ga-As and the In-As bond length distribution, using the simplified approach. The Kirkwood model seems adequate to describe the experimental data at this time, although further refinement of the error bars may require the use of a better potential containing more parameters.

We would like to thank Rosa Barabash for discussions and help with the analysis of the static atom displacements, and Andrea Perez and the support staff at CHESS for help with data collection and analysis. This work was supported by DOE through Grant No. DE FG02 97ER45651. CHESS is operated by NSF through Grant No. DMR97-13424.

- [1] R. W. G. Wyckoff, *Crystal Structures* (Wiley, New York, 1967), Vol. 1, 2nd ed.
- [2] J. C. Mikkelsen and J. B. Boyce, *Phys. Rev. Lett.* **49**, 1412 (1982); J. C. Mikkelsen and J. B. Boyce, *Phys. Rev. B* **28**, 7130 (1983).
- [3] Y. Cai and M. F. Thorpe, *Phys. Rev. B* **46**, 15 879 (1992).
- [4] J. L. Martins and A. Zunger, *Phys. Rev. B* **30**, 6217 (1984); M. C. Schabel and J. L. Martins, *Phys. Rev. B* **43**, 11 873 (1991).
- [5] A. Balzarotti *et al.*, *Phys. Rev. B* **31**, 7526 (1985); H. Oyanagi *et al.*, *Solid State Commun.* **67**, 453 (1988).
- [6] A. Zunger *et al.*, *Phys. Rev. Lett.* **65**, 353 (1990).
- [7] B. E. Warren, *X-Ray Diffraction* (Dover, New York, 1990).
- [8] Y. Waseda, *The Structure of Non-Crystalline Materials* (McGraw-Hill, New York, 1980).
- [9] T. Egami, *Mater. Trans.* **31**, 163 (1990); T. Egami, in *Local Structure from Diffraction*, edited by S. J. L. Billinge and M. F. Thorpe (Plenum, New York, 1998), p. 1.
- [10] I-K. Jeong, F. Mohiuddin-Jacobs, V. Petkov, and S. J. L. Billinge (unpublished).
- [11] H. P. Klug and L. E. Alexander, *X-ray Diffraction Procedures for Polycrystalline Materials* (Wiley, New York, 1974), 2nd ed.
- [12] V. Petkov, *J. Appl. Crystallogr.* **22**, 387 (1989).
- [13] Th. Proffen and S. J. L. Billinge, *J. Appl. Crystallogr.* **32**, 572 (1999).
- [14] J. G. Kirkwood, *J. Chem. Phys.* **7**, 506 (1939).
- [15] Jean S. Chung and M. F. Thorpe, *Phys. Rev. B* **55**, 1545 (1997); **59**, 4807 (1999); M. F. Thorpe *et al.*, in *Local Structure from Diffraction*, edited by S. J. L. Billinge and M. F. Thorpe (Plenum, New York, 1998), p. 157.
- [16] J. S. Chung, R. I. Barabash, and M. F. Thorpe (unpublished).

Atomic-Scale Structure of Nanocrystalline $\text{Ba}_x\text{Sr}_{1-x}\text{TiO}_3$ ($x = 1, 0.5, 0$) by X-ray Diffraction and the Atomic Pair Distribution Function Technique

Valeri Petkov,^{*,†} Milen Gateshki,[†] Markus Niederberger,[‡] and Yang Ren[§]

Department of Physics, Central Michigan University, Mt. Pleasant, Michigan 48859, Max-Planck Institute of Colloids and Interfaces, Potsdam D-14424, Germany, and Advanced Photon Source, Argonne National Laboratory, Argonne, Illinois 60439

Received September 23, 2005. Revised Manuscript Received November 13, 2005

The atomic-scale structure of nanocrystalline $\text{Ba}_x\text{Sr}_{1-x}\text{TiO}_3$ ($x = 1, 0.5, 0$) powders has been studied using high-energy X-ray diffraction, Rietveld refinement, and the atomic pair distribution function technique. The studies show that the materials are well-ordered at nanometer length distances. The three-dimensional atomic ordering in $\text{Ba}_{0.5}\text{Sr}_{0.5}\text{TiO}_3$ and SrTiO_3 nanopowders may well be described by a cubic structure of the perovskite type, similar to that occurring in the corresponding bulk crystals. The three-dimensional atomic ordering in BaTiO_3 is more complex. It is cubic-like on average, but locally shows slight distortions of a tetragonal-type. The new structural information helps one to understand better the dielectric properties of these nanomaterials.

1. Introduction

Crystalline perovskite-type oxides show many useful properties and are widely used as catalysts and in piezoelectrics and ferroelectrics.^{1,2} A prime example is the family of $\text{Ba}_x\text{Sr}_{1-x}\text{TiO}_3$ oxides, in particular, BaTiO_3 . The material exists in several crystallographic modifications, each showing a particular dielectric behavior. At high temperature BaTiO_3 has a centrosymmetric cubic structure and is paraelectric. Between room temperature and 393 K the material possesses a tetragonal-type structure, below 278 K the structure is orthorhombic, and below 183 K it is rhombohedral.³ Fragments of the four polymorphs occurring with BaTiO_3 are presented in Figure 1. The picture is characteristic of perovskites: all crystalline modifications of $(\text{Ba}/\text{Sr})\text{TiO}_3$ feature a three-dimensional network of $\text{Ti}-\text{O}_6$ octahedra with Ba/Sr atoms occupying the network channels. The asymmetry of the low-temperature crystallographic modifications arises from a displacement of the Ti cations with respect to the oxygen octahedra (as depicted in Figures 1b–1d) and gives rise to spontaneous polarization. As a result, BaTiO_3 becomes ferroelectric below 393 K. The high permittivity of the tetragonal modification of BaTiO_3 and the ability to switch the direction of polarization in response to external electric fields have found application in commercially available devices such as thin film and multilayer capacitors.^{4,5}

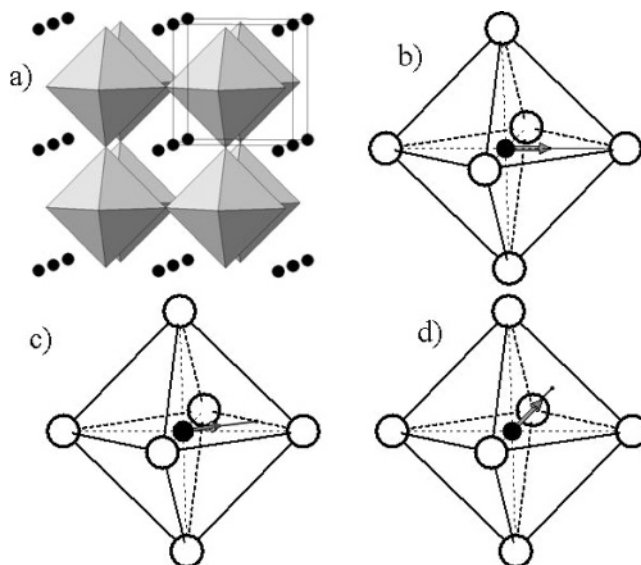


Figure 1. Fragments of the cubic- (a), tetragonal- (b), orthorhombic- (c), and rhombohedral-type (d) structures occurring with bulk BaTiO_3 crystals. All structure types feature a 3D network of corner-sharing $\text{Ti}-\text{O}_6$ octahedra with Ba atoms (solid circles) occupying the open space between them as shown in (a). Note the octahedral units are perfect in the cubic-type structure. The $\text{Ti}-\text{O}_6$ octahedra shown are somewhat distorted with the non-cubic-type structure types due to the off-center displacement (directions shown with arrows) of Ti atoms (solid circles at the center of the octahedra) as depicted in (b), (c), and (d). The octahedra are centered by Ti atoms (small solid circles) and coordinated by oxygens (open circles). The unit cell in the case of the cubic-type perovskite structure is outlined with thin solid lines.

SrTiO_3 is a typical perovskite possessing a cubic structure (see Figure 1a) at room temperature. Although BaTiO_3 and SrTiO_3 have structures of a similar (perovskite) type, they show very different transition behavior. It is not until SrTiO_3 is cooled to 110 K when its cubic structure distorts and

* To whom correspondence should be addressed. E-mail: petkov@phy.cmich.edu.

[†] Central Michigan University.

[‡] Max-Planck Institute of Colloids and Interfaces.

[§] Argonne National Laboratory.

(1) Chandler, C. D.; Roger C.; Hampden-Smith, M. J. *Chem. Rev.* **1993**, *93*, 1205.

(2) Bhalla, A. S.; Gou, R.; Roy, R. *Mater. Res. Innovations* **2000**, *4*, 3.

(3) Kwei, G.; Billinge, S. J. L.; Cheong, S.-W.; Saxton, J. G. *Ferroelectrics* **1995**, *164*, 57.

(4) Hennings, D.; Klee, M.; Waser, R. *Adv. Mater.* **1991**, *3*, 334.

(5) Frey, M. H.; Payne, D. A. *Appl. Phys. Lett.* **1993**, *63*, 2753.

becomes tetragonal.^{6,7} Thus, $SrTiO_3$ exhibits paraelectric behavior at room temperature, although recent studies suggest that the material is indeed an incipient ferroelectric whose ferroelectricity is suppressed by quantum fluctuations.⁸

Barium-based mixed oxides have also attracted much attention.⁹ In particular, $Ba_xSr_{1-x}TiO_3$ has shown excellent dielectric properties, especially as thin films. At room temperature and low concentrations of Sr ($x < 0.5$) these mixed oxides adopt a tetragonal-type structure¹⁰ featuring slightly distorted $Ti-O_6$ octahedra (see Figure 1b). At higher concentrations of Sr the structure is of the cubic type shown in Figure 1a.¹¹

It has been discovered that many of the useful properties of perovskite materials are critically dependent on the crystallite size. For example, it has been found that at room temperature the structure of $BaTiO_3$ transforms to cubic-like when the crystallite size becomes smaller than 100 nm.^{12,13} On the other hand, high-resolution synchrotron radiation studies and Raman scattering experiments have shown that fine $BaTiO_3$ powders with crystallite size as small as 40 nm show a structure with tetragonal distortions and exhibit somewhat reduced but still measurable spontaneous polarization.¹⁴ Recently, the attention has shifted to even finer powders with crystallites as small as only a few nanometers. The reason is that having $Ba_xSr_{1-x}TiO_3$ in a nanocrystalline state is a key requirement for producing defect-free thin films.^{15,16} Furthermore, nanosize powders provide good sinterability, which is an essential property for the fabrication of advanced ceramic materials.^{2,4}

When in a nanocrystalline state $Ba_xSr_{1-x}TiO_3$ ceramics are non-ferroelectric, resulting in stable dielectric properties.^{17,18} Several explanations for the disappearance of ferroelectricity have been put forward. They point to the absence of long-range cooperative structural distortions as one of the main reasons that could lead to a suppression of the thermodynamically stable tetragonal phase and the related to it ferroelectric behavior in nanostructured $Ba_xSr_{1-x}TiO_3$.¹⁹ A thorough understanding of this so-called size effect and the properties of nanocrystalline barium/strontium-based materials obviously requires a detailed knowledge of their atomic-

scale structure. Usually the structure of materials is determined from the Bragg peaks in their diffraction patterns. However, nanocrystalline materials lack the extended order of the usual crystals and show diffraction patterns with a pronounced diffuse component and a few broad Bragg-like features. This renders the traditional diffraction techniques for structure determination very difficult to apply. That is why structural studies on nanocrystals are scarce and the atomic arrangement in $Ba_xSr_{1-x}TiO_3$ nanopowders has not been determined in detail yet. Recently, it has been shown that the three-dimensional (3D) structure of materials with reduced structural coherence, including nanocrystals, can be determined using the so-called atomic pair distribution function (PDF) technique.^{20–23} Here, we employ the traditional Rietveld and the nontraditional PDF technique to determine the 3D structure of $Ba_xSr_{1-x}TiO_3$ ($x = 1, 0.5, 0$) nanoparticles with crystallites having size as small as 5 nm. We find that these nanostructured materials possess a well-defined atomic arrangement that may be described in terms of the perovskite-type structure depicted in Figure 1. The new structural information helps one understand better the dielectric properties of the nanomaterials.

2. Experimental Section

2.1. Sample Preparation. Nanocrystalline $Ba_xSr_{1-x}TiO_3$ samples were obtained through a recently discovered approach employing a nonhydrolytic and halide-free procedure.²⁴ In the first step of the procedure metallic barium and/or strontium were dissolved in anhydrous benzyl alcohol at elevated temperatures (343–373 K). Generally, Sr needed a higher temperature to dissolve than Ba. The resulted solutions were mixed with 1 molar equiv of titanium isopropoxide, and the reaction mixture was transferred to a steel autoclave and heated at 574 K for 48 h. The heating took place under subsolvothermal conditions since the boiling point of benzyl alcohol is about 478 K. Representative TEM images of thus-obtained nanocrystalline materials are shown in Figures 2, 3, and 4 in ref 24. The TEM images reveal that the samples consist of individual particles with an average size of about 5 nm. Analyses based on the width of the peaks in the X-ray diffraction patterns of $Ba_xSr_{1-x}TiO_3$ performed by us yielded very similar estimates for the average nanocrystallites' size. The TEM studies also show that the nanocrystals are uniform in size and mostly spherical. No large particles or agglomerates are observed. Thus-obtained nanocrystalline $Ba_xSr_{1-x}TiO_3$ ($x = 1, 0.5, 0$) powders were loaded into glass capillaries and subjected to synchrotron radiation scattering experiments.

2.2. Synchrotron Radiation Scattering Experiments. Synchrotron radiation scattering experiments were carried out at the beamline 11-ID-C (Advanced Photon Source, Argonne National Laboratory) using X-rays of energy 115.232 keV ($\lambda = 0.1076 \text{ \AA}$) at room temperature. X-rays of higher energy were used to obtain diffraction data to higher values of the wave vector, Q , which is important for the success of PDF analysis ($Q_{\max} = 28 \text{ \AA}^{-1}$ with

-
- (6) Lytle, F. W. *J. Appl. Phys.* **1964**, *35*, 2212.
 (7) Salje, E. K.; Gallardo, M. C.; Jimenes, J.; Cerro, J. *J. Phys.: Condens. Matter* **1998**, *10*, 5535.
 (8) Wang, Y. X. *Solid State Commun.* **2005**, *135*, 290.
 (9) Thongrueng, J.; Nishio, K.; Watanabe, Y.; Nagata, K.; Tsuchiya, T. *J. Aust. Ceram. Soc.* **2001**, *37*, 51.
 (10) Josef, J.; Vimala, T. M.; Raju, J.; Murthy, V. R. K. *J. Appl. Phys.* **1999**, *32*, 1049.
 (11) Liu, R. S.; Cheng, Y. C.; Chen, J. M.; Liu, R. G.; Wang, J. L.; Tsai, J. C.; Hsu, M. Y. *Mater. Lett.* **1998**, *37*, 285.
 (12) Uchino, K.; Sadanaga, E.; Hirose, T. *J. Am. Ceram. Soc.* **1989**, *72*, 1151.
 (13) Begg, B. D.; Vance, E. R.; Nowotny, J. *J. Am. Ceram. Soc.* **1994**, *77*, 3186.
 (14) Yashimura, M.; Hoshina, T.; Ishimura, D.; Kobayashi, S.; Nakamura, W.; Tsurumi, T.; Wada, S. *J. Appl. Phys.* **2005**, *98*, 014313.
 (15) Matsuda, H.; Kobayashi, N.; Kobayashi, T.; Miyazawa, K.; Kuwabara, N. *J. Non-Cryst. Solids* **2000**, *271*, 162.
 (16) Zhang, J.; Yin, Z.; Zhang, M.-S. *Phys. Lett. A* **2003**, *310*, 479.
 (17) Takeuchi, T.; Tabuchi, M.; Ado, K.; Honjo, K.; Nakamura, O.; Kageyama, H.; Suyama, Y.; Ohtori, N.; Nagasawa, M. *J. Mater. Sci.* **1997**, *32*, 4053.
 (18) Soten, I.; Miguez, H.; Yang, S. M.; Petrov, S.; Coombs, N.; Tetreault, N.; Matsuura, N.; Ruda, H. E.; Ozin, G. *Adv. Funct. Mater.* **2002**, *12*, 1997.
 (19) Frey, M. H.; Payne, D. A. *Phys. Rev. B* **1996**, *54*, 3158.

-
- (20) Toby, B. H.; Egami T. *Acta Crystallogr. A* **1992**, *48*, 336.
 (21) Gateshki, M.; Hwang, S.-J.; Park, D. H.; Ren, Y.; Petkov, V. *J. Phys. Chem. B* **2004**, *108*, 14956.
 (22) Billinge, S. J. L.; Kanatzidis, M. G. *Chem. Commun.* **2004**, *7*, 749.
 (23) Petkov, V.; Trikalitis, P. N.; Bozin, E. S.; Billinge, S. J. L.; Vogt, T.; Kanatzidis, M. G. *J. Am. Chem. Soc.* **2002**, *124*, 10157.
 (24) (a) Niederberger, M.; Pinna, N.; Polleux, J.; Antonietti, M. *Angew. Chem., Int. Ed.* **2004**, *43*, 2270. (b) Niederberger, M.; Garnweitner, G.; Pinna, N.; Antonietti, M. *J. Am. Chem. Soc.* **2004**, *126*, 9120.

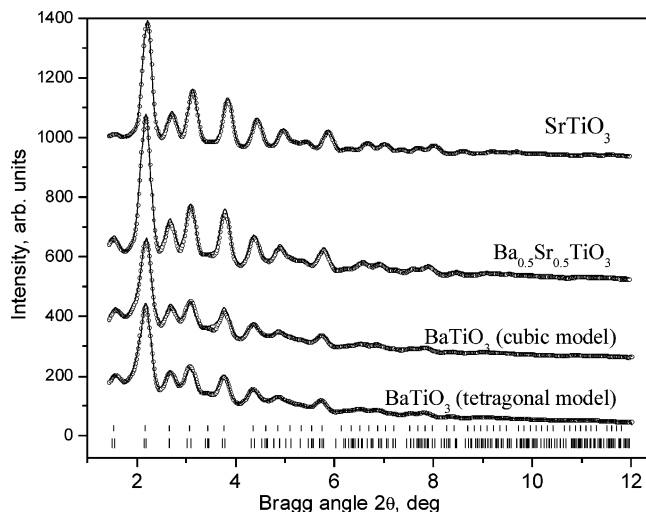


Figure 2. Experimental powder diffraction patterns for nanocrystalline $\text{Ba}_x\text{Sr}_{1-x}\text{TiO}_3$ (symbols) and calculated patterns (solid lines) obtained through Rietveld refinements. The positions of the Bragg peaks of the cubic (upper set of bars) and tetragonal (lower set of bars) structures that were fitted to the diffraction pattern of BaTiO_3 are given in the lower part of the plot. Note the diffraction data for SrTiO_3 and $\text{Ba}_{0.5}\text{Sr}_{0.5}\text{TiO}_3$ are approximated with a cubic-type structure only. The corresponding goodness-of-fit factors, R_w , for each of the refinements are reported in Table 1.

the present experiments). The scattered radiation was collected with an imaging plate detector (mar345). The use of an imaging plate detector greatly reduces the data collection time and improves the statistical accuracy of the diffraction data as demonstrated by recent experiments on materials with reduced structural coherence.²⁵ Up to 10 images were taken for each of the samples. The exposure time was 10 s/image. The corresponding images were combined, subjected to geometrical corrections, integrated, and reduced to one-dimensional X-ray diffraction (XRD) patterns using the computer program FIT2D.²⁶ Thus-obtained XRD patterns for the three samples studied are presented in Figure 2.

3. Results

As can be seen in Figure 2, the experimental XRD patterns of nanocrystalline $\text{Ba}_x\text{Sr}_{1-x}\text{TiO}_3$ powders show only a few broad, Bragg-like peaks that merge into a slowly oscillating diffuse component already at Bragg angles as low as 6° . As our subsequent analyses show, the diffraction patterns of SrTiO_3 and $\text{Ba}_{0.5}\text{Sr}_{0.5}\text{TiO}_3$ can be indexed in a cubic unit cell while that of BaTiO_3 can be indexed in both cubic and tetragonal unit cells of the perovskite-type structure type shown in Figure 1. Such diffraction patterns are typical for materials of limited structural coherence and are obviously difficult to be tackled by traditional techniques for structure determination. However, when reduced to the corresponding atomic PDFs, they become a structure-sensitive quantity lending itself to structure determination.

The frequently used atomic Pair Distribution Function, $G(r)$, is defined as

$$G(r) = 4\pi r[\rho(r) - \rho_0] \quad (1)$$

where $\rho(r)$ and ρ_0 are the local and average atomic number densities, respectively, and r is the radial distance. It peaks at characteristic distances separating pairs of atoms and thus reflects the atomic-scale structure. The PDF $G(r)$ is the Fourier transform of the experimentally observable total structure function, $S(Q)$, i.e.,

$$G(r) = (2/\pi) \int_{Q=0}^{Q_{\max}} Q[S(Q) - 1] \sin(Qr) dQ \quad (2)$$

where Q is the magnitude of the wave vector ($Q = 4\pi \sin \theta/\lambda$), 2θ is the angle between the incoming and outgoing radiation beams, and λ is the wavelength of the radiation used. The structure function is related to the coherent part of the total scattered intensity as

$$S(Q) = 1 + [I^{\text{coh}}(Q) - \sum c_i |f_i(Q)|^2] / \sum c_i |f_i(Q)|^2 \quad (3)$$

where $I^{\text{coh}}(Q)$ is the coherent scattering intensity per atom in electron units and c_i and f_i are the atomic concentration and X-ray scattering factor, respectively, for the atomic species of type i .²⁷ As can be seen from eqs 1–3, the PDF is simply another representation of the powder XRD data. However, exploring the diffraction data in real space is advantageous, especially in the case of materials of limited structural coherence. First, as eqs 2 and 3 imply, the total scattering, including Bragg scattering as well as diffuse scattering, contributes to the PDF. In this way both the average, longer range atomic structure, manifested in the Bragg peaks, and the local structural distortions, manifested in the diffuse component of the diffraction pattern, are reflected in the PDF. And second, the atomic PDFs do not imply any periodicity and can be used to study the atomic ordering in materials showing any degree of structural coherence, ranging from crystals²⁸ to glasses²⁹ and even liquids.³⁰ Recently, the atomic PDF approach has been successfully applied to nanocrystalline materials^{31–33} as well.

Experimental PDFs for the samples studied were obtained as follows. First, the coherently scattered intensities were extracted from the corresponding XRD patterns by applying appropriate corrections for flux, background, Compton scattering, and sample absorption. The intensities were normalized in absolute electron units, reduced to structure functions $Q[S(Q) - 1]$, and Fourier-transformed to atomic PDFs. Thus-obtained experimental atomic PDFs are shown in Figure 3. All data processing was done with the help of the program RAD.³⁴ As can be seen in Figure 3, the experimental PDFs are rich in structural features but they vanish at interatomic distances of 2–2.5 nm which are much shorter than the average size of the nanocrystals (~ 5 nm).

(27) Klug, H. P.; Alexander, L. E. In *X-ray Diffraction Procedures for Polycrystalline Materials*; Wiley: New York, 1974.

(28) Petkov, V.; Jeong, I.-K.; Chung, J. S.; Thorpe, M. F.; Kycia, S.; Billinge, S. J. L. *Phys. Rev. Lett.* **1999**, *83*, 4089.

(29) Petkov, V.; Billinge, S. J. L.; Sashtri, S. D.; Himmel, B. *Phys. Rev. Lett.* **2000**, *85*, 3436.

(30) Petkov, V.; Yunchov, G. *J. Phys.: Condens. Matter* **1996**, *8*, 6145.

(31) Petkov, V.; Zavalij, P. Y.; Lutta, S.; Whittingham, M. S.; Parvanov, V.; Sashtri, S. D. *Phys. Rev. B* **2004**, *69*, 085410.

(32) Dmowski, W.; Egami, T.; Swider-Lyons, K. E.; Love, C. T.; Rollison, D. R. *J. Phys. Chem. B* **2002**, *106*, 12677.

(33) Gateshki, M.; Petkov, V.; Williams, G.; Pradhan, S. K.; Ren, Y. *Phys. Rev. B* **2005**, *71*, 224107.

(34) Petkov, V. *J. Appl. Crystallogr.* **1989**, *22*, 387.

(25) (a) Chupas, P. J.; Qiu, X.; Lee, P.; Grey, C. P.; Billinge, S. J. L. *J. Appl. Crystallogr.* **2003**, *36*, 1342. (b) Petkov, V.; Qadir, D.; Sashtri, S. D. *Solid State Commun.* **2004**, *129*, 239.

(26) Hammersley, A. P.; Hanfland, M.; Hausermann, D. *High-Pressure Res.* **1996**, *14*, 235.

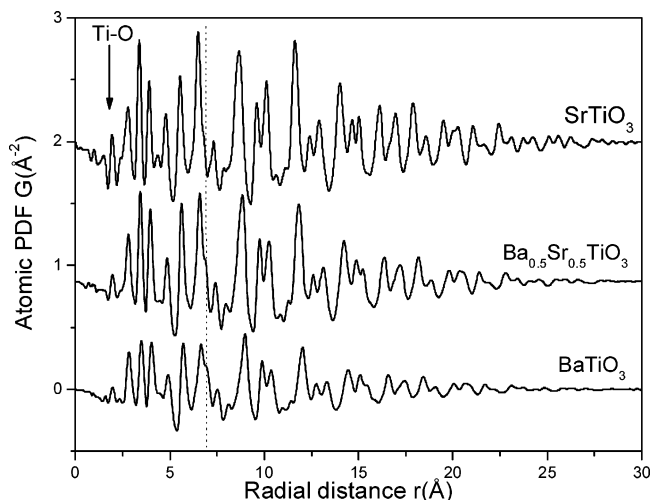


Figure 3. Experimental PDFs for nanocrystalline $Ba_xSr_{1-x}TiO_3$ extracted from the corresponding powder diffraction patterns using data extending to wave vectors as high as 28 \AA^{-1} . The position of the first PDF peak, reflecting Ti–O first neighbor atomic pairs, is marked with an arrow. Note the intensity of the first PDF peak changes with the relative Sr/Ba content due to the different scattering power for X-rays of Ba and Sr. A broken line runs, as a guide to the eye, through the shoulder of the PDF peak centered at approximately 6.7 \AA . The shoulder diminishes with Sr content.

This observation shows that the nanocrystalline $Ba_xSr_{1-x}TiO_3$ not only lacks the extended order of usual crystals but shows some structural distortions that further reduce their structural coherence. Such structural distortions are frequently observed with nanoparticles of sizes from $5\text{--}10 \text{ nm}$ and are often ascribed to surface relaxation effects.³⁵ The distortions are more pronounced with nanocrystalline $BaTiO_3$ than with the samples containing Sr since its PDF decays to zero faster than those of the other two materials (see Figure 3). The first peak in the three experimental PDFs shown in Figure 3 is positioned at approximately $1.98(2) \text{ \AA}$, which is close to the average Ti–O first neighbor distance observed in the corresponding crystalline bulk perovskites. The area under the peak yields $5.8(2)$ oxygen neighbors for each titanium atom, reflecting the presence of Ti–O₆ octahedral units in the nanomaterials. The peak is quite sharp and appears with almost the same shape and full-width at half-maximum ($\sim 0.18 \text{ \AA}$) in the PDFs for the three samples showing that they all are built of well-defined Ti–O₆ octahedra. Also, the three experimental PDFs exhibit a similar oscillatory behavior at longer interatomic distances, indicating that nanocrystalline $Ba_xSr_{1-x}TiO_3$ ($x = 1, 0.5, 0$) share common structural features, those of an extended network of Ti–O₆ octahedra. However, some fine but clearly noticeable differences in the experimental PDFs are also observed. For example, the peak at approximately 6.7 \AA appears with a well-pronounced shoulder in the PDF for $BaTiO_3$. The same peak in the PDF for $SrTiO_3$ has no such pronounced shoulder. In general, the initial analysis of the experimental PDFs suggests that the atomic ordering in $Ba_xSr_{1-x}TiO_3$ nanopowders is likely to be of the same type but differ in some fine details for different concentrations of Ba and Sr. To reveal the fine features in the atomic ordering in nanocrystalline $Ba_xSr_{1-x}TiO_3$, we tested several structural models

Table 1. Structure Data for Nanocrystalline $Ba_xSr_{1-x}TiO_3$ ($x = 1, 0.5, 0$) as Obtained by the Present Rietveld and PDF Refinements^a

	$BaTiO_3$		$Ba_{0.5}Sr_{0.5}TiO_3$		$SrTiO_3$	
	Rietveld	PDF	Rietveld	PDF	Rietveld	PDF
$a, \text{ \AA}$	4.016(6)	4.021(5)	3.985(4)	3.979(6)	3.930(3)	3.927(5)
$U_{Ba/Sr} (\text{ \AA}^2)$	0.022(2)	0.009(2)	0.014(2)	0.016(2)	0.013(2)	0.009(2)
$U_{Ti} (\text{ \AA}^2)$	0.016(2)	0.015(2)	0.013(2)	0.006(2)	0.008(2)	0.010(2)
$U_O (\text{ \AA}^2)$	−0.001(2)	0.022(2)	0.001(2)	0.030(2)	0.012(2)	0.031(2)
Rw, %	2.81	25	2.37	19	2.34	18

^a The refinements are based on the cubic-type structure presented in Figure 1a. The goodness-of-fit (Rietveld, see eq 4) and reliability (PDF, see eq 5) factors R_w are reported for each of the refinements.

analyzing the experimental diffraction data both in reciprocal and real space employing the Rietveld and PDF techniques, respectively.

4. Discussion

At first, we approached the experimental XRD patterns with the widely employed Rietveld technique. The Rietveld technique³⁶ is used for crystal structure determination and refinement from powder diffraction data. The method employs a least-squares procedure to compare experimental Bragg intensities with those calculated from a plausible structural model. The parameters of the model are then adjusted until the best fit to the experimental diffraction data is achieved. The progress of the fit is assessed by computing various goodness-of-fit factors with the most frequently used being³⁷

$$R_w = \left\{ \frac{\sum w_i (y_i^{\text{obs}} - y_i^{\text{calc}})^2}{\sum w_i (y_i^{\text{obs}})^2} \right\}^{1/2} \quad (4)$$

where y_i^{obs} and y_i^{calc} are the observed and calculated data points and w_i are weighting factors taking into account the statistical accuracy of the diffraction experiment. The Rietveld analyses were carried out with the help of the program FullProf.³⁸ The XRD patterns of nanocrystalline $SrTiO_3$ and $Ba_{0.5}Sr_{0.5}TiO_3$ were fit with a cubic structure of a perovskite type^{39,11} that is found with the corresponding bulk crystals at room temperature. The XRD pattern of $BaTiO_3$ was approached with both the cubic and tetragonal structures (see Figures 1a and 1b) occurring with the corresponding bulk crystal. Results from the Rietveld refinements are presented in Figure 2 and the values of the refined structural parameters in Tables 1 and 2. As can be seen in Figure 2, the XRD pattern of $SrTiO_3$ and $Ba_{0.5}Sr_{0.5}TiO_3$ are very well reproduced by a model based on the cubic structure of a perovskite type shown in Figure 1a. The results show that even when in the nanocrystalline state, $SrTiO_3$ and $Ba_{0.5}Sr_{0.5}TiO_3$ adopt the structure type of the corresponding bulk crystals. The XRD pattern for nanocrystalline $BaTiO_3$ is almost equally well reproduced by the cubic and tetragonal perovskite-type structure as the data presented in Figure 2 shows. The values of the corresponding goodness-of-fit factors R_w , see Tables

(36) Rietveld, H. M. *J Appl. Crystallogr.* **1969**, 2, 65.

(37) Young, R. A. In *The Rietveld Method*; Oxford University Press: New York, 1996.

(38) Rodríguez-Carvajal, J. *Physica B* **1993**, 192, 55.

(39) Abramov, Y. A.; Tsirel'son, V. G.; Zavodnik, V. E.; Ivanov, S. A.; Brown, I. D. *Acta Crystallogr. B* **1983**, 39, 942.

(35) Gilbert, B.; Huang, F.; Zhang, H. Z.; Waychunas G. A.; Banfield, J. F. *Science* **2004**, 305, 65.

Table 2. Structure Data for Nanocrystalline BaTiO₃ as Obtained by the Present Rietveld and PDF Refinements^a

	Rietveld	PDF
<i>a</i> , Å	3.987(6)	3.997(6)
<i>c</i> , Å	4.091(7)	4.0851(7)
<i>z</i> (Ti)	0.467(5)	0.470(3)
<i>z</i> (O1)	-0.138(5)	-0.130(7)
<i>z</i> (O2)	0.495(6)	0.490(3)
<i>U</i> _{Ba} (Å ²)	0.027(2)	0.010(2)
<i>U</i> _{Ti} (Å ²)	0.006(2)	0.018(2)
<i>U</i> _O (Å ²)	-0.020(2)	0.021(2)
<i>R</i> _w , %	2.47	21

^a The refinements are based on the tetragonal-type structure presented in Figure 1b. The goodness-of-fit (Rietveld, see eq 4) and reliability (PDF, see eq 5) factors *R*_w are reported for each of the refinements.

1 and 2, does not allow one to draw a definitive conclusion in favor of either of the two different structure models attempted either. Moreover, the Rietveld analysis of the XRD data for the nanocrystalline BaTiO₃ yielded negative values for the mean-square atomic displacements of oxygen atoms (also known as thermal factors; see Tables 1 and 2). Such unphysical results are often obtained with Rietveld analyses of powder diffraction patterns for materials with considerably reduced structural coherence. The problems stem from the inability of the Rietveld analysis to handle properly diffraction patterns showing both broad Bragg peaks and pronounced diffuse scattering. As we demonstrate below, the difficulties are greatly reduced when the diffraction data are analyzed in terms of the corresponding atomic PDFs. Similarly to the Rietveld technique, the PDF technique employs a least-squares procedure to compare experimental and model data (PDF) calculated from a plausible structural model. The structural parameters of the model (unit cell constants, atomic coordinates, and thermal factors) are adjusted until the best possible fit to the experimental data is achieved. The progress of the refinement is assessed by computing a reliability factor, *R*_w:

$$R_w = \left\{ \frac{\sum w_i (G_i^{\text{exp.}} - G_i^{\text{calc.}})^2}{\sum w_i (G_i^{\text{exp.}})^2} \right\}^{1/2} \quad (5)$$

where *G*^{exp.} and *G*^{calc.} are the experimental and calculated PDFs, respectively, and *w*_{*i*} are weighting factors reflecting the statistical quality of the individual data points.

Results from the PDF analyses of the experimental data for Ba_{*x*}Sr_{1-*x*}TiO₃ (*x* = 1, 0.5, 0) in terms of the cubic structure are presented in Figures 4, 5, and 6. Structure data from literature sources^{3,40-42} were used as initial values in the PDF refinements. The PDF refinements were done with the help of the program PDFFIT.⁴³ To mimic the presence of limited structural disorder in the nanocrystalline materials, we multiplied the model PDF data with a decaying exponent of the type exp(-α*r*) as originally suggested by Ergun and later on implemented in a similar manner by Gilbert et al.⁴⁴ Typical values for α used were of the order of 0.1 Å⁻¹. The

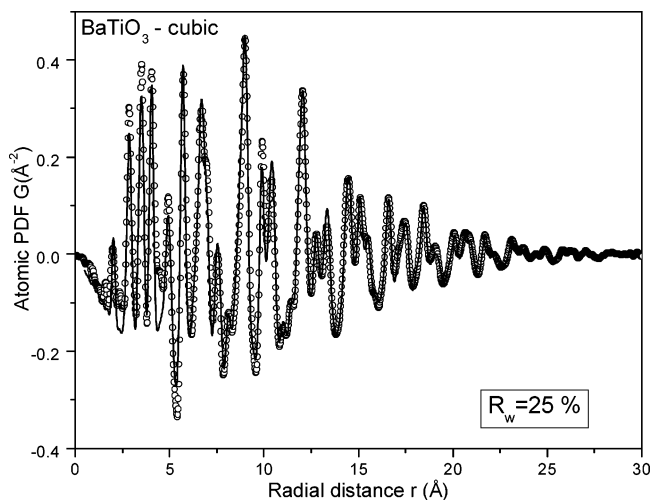


Figure 4. Experimental (symbols) and model (solid line) PDFs for BaTiO₃. The model PDF is based on the cubic-type structure shown in Figure 1a. The parameters of the model are given in Table 1. The reliability factor *R*_w is reported in the lower part of the figure.

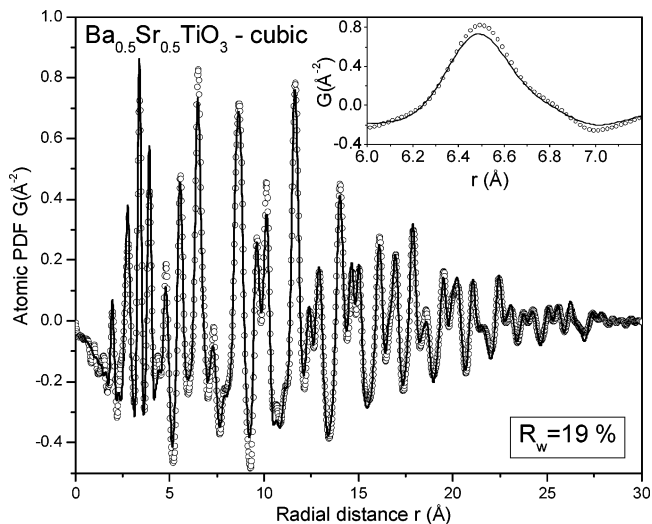


Figure 5. Experimental (symbols) and model (solid line) PDFs for Ba_{0.5}Sr_{0.5}TiO₃. The model PDF is based on a structure of the cubic type shown in Figure 1a. The parameters of the model are given in Table 1. The reliability factor *R*_w is reported in the lower part of the figure. The peak at 6.7 Å is given an enlarged scale in the inset. Its shape is well-reproduced by a cubic-type model.

refined values of the structural parameters from the analysis are summarized in Table 1. In the case of SrTiO₃ and Ba_{0.5}Sr_{0.5}TiO₃ the PDF-based fit yielded structural parameters that are in good agreement with the present Rietveld results (see Table 1). The agreement documents well the fact that the atomic PDF provides a firm quantitative basis for structure determination. The reliability factors (defined by eq 5) also reported in Table 1 are as low (~18%) as could be achieved with a PDF refinement.⁴⁵ These results support the findings of the Rietveld refinements that the atomic ordering in nanocrystalline SrTiO₃ and Ba_{0.5}Sr_{0.5}TiO₃ can be well-described in terms of the perovskite, cubic-type structure (space group *Pm* $\bar{3}$ *m*) depicted in Figure 1a. Models based on the perovskite, tetragonal-type structure (space group *P4mm*) were also attempted with the PDF data for SrTiO₃ and Ba_{0.5}Sr_{0.5}TiO₃. These models, although having more internal degrees of freedom, did not give any significant

(40) Buttner, R. H.; Maslen, E. N. *Acta Crystallogr.* **1983**, *39*, 7764.

(41) Evans, H. T. *Acta Crystallogr.* **1967**, *1*, 1948.

(42) Hewat, A. W. *Ferroelectrics* **1974**, *6*, 215.

(43) Proffen, T.; Billinge, S. J. L. *J. Appl. Crystallogr.* **1999**, *32*, 572.

(44) Ergun, S.; Schehl, R. R. *Carbon* **1973**, *11*, 127. Gilbert, B.; Huang, F.; Zhang, H. Z.; Waychunas, G. A.; Banfield, J. F. *Science* **2004**, *305*, 65.

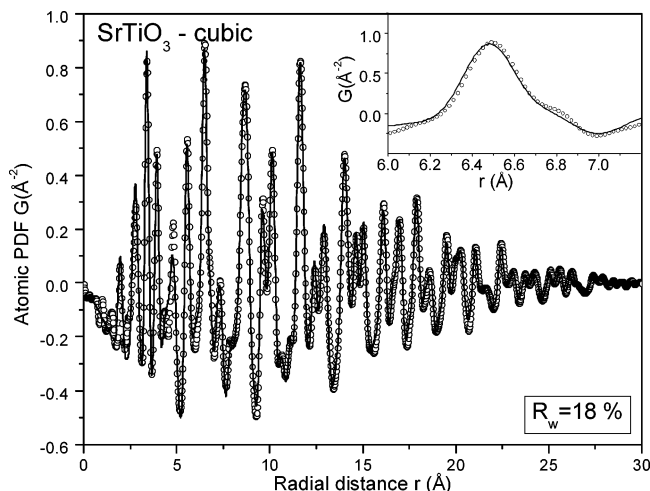


Figure 6. Experimental (symbols) and model (solid line) PDFs for $SrTiO_3$. The model PDF is based on a structure of the cubic type shown in Figure 1a. The parameters of the model are given in Table 1. The reliability factor R_w is reported in the lower part of the figure. The peak at 6.7 Å is given an enlarged scale in the inset. Its shape is well-reproduced by a cubic-type model.

improvement in the reliability factors nor in reproducing the important details in the experimental data. This observation reinforced our conclusion that nanocrystalline $SrTiO_3$ and $Ba_{0.5}Sr_{0.5}TiO_3$ studied by us possess a cubic-type structure at room temperature as their crystalline analogues do.

The atomic ordering in $BaTiO_3$, however, is not so well-described in terms of the perovskite, cubic-type structure as the relatively high value ($\sim 25\%$, see Table 1) of the corresponding reliability factor R_w shows. That is why we attempted three more structural models based on the other three structural modifications: tetragonal (space group $P4mm$), orthorhombic (space group $Amm2$), and rhombohedral (space group $R3m$), occurring with bulk crystalline $BaTiO_3$. Results from PDF analyses of the experimental data in terms of these three structural models are presented in Figures 7, 8, and 9, respectively. As the results in Figures 8 and 9 show, the orthorhombic- and rhombohedral-type models (see Figures 1c and 1d) may be unambiguously ruled out because they feature substantially distorted $Ti-O_6$ octahedral units, i.e., a broad distribution of first neighbor $Ti-O$ distances (2 $Ti-O$ distances at 1.86 Å, two $Ti-O$

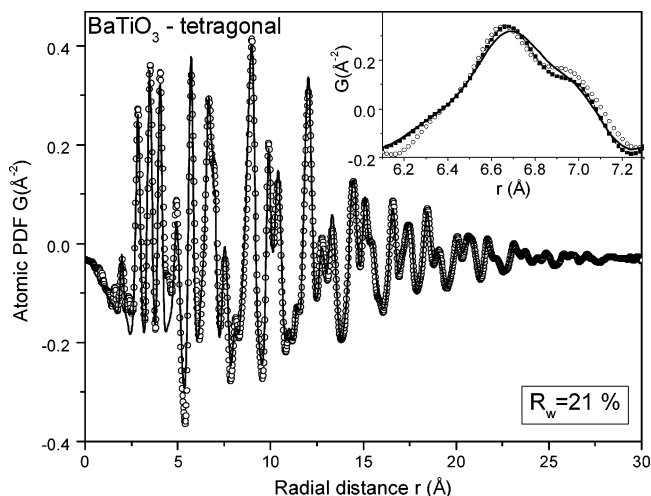


Figure 7. Experimental (symbols) and model (solid line) PDFs for $BaTiO_3$. The model PDF is based on the tetragonal-type structure shown in Figure 1b. The parameters of the model are given in Table 2. The reliability factor R_w is reported in the lower part of the figure. A portion of the experimental data (open circles) is compared to model ones based on cubic-type (solid line) and tetragonal-type structures (solid symbols) in the inset on an enlarged scale. The experimental data are better reproduced by the tetragonal-type model.

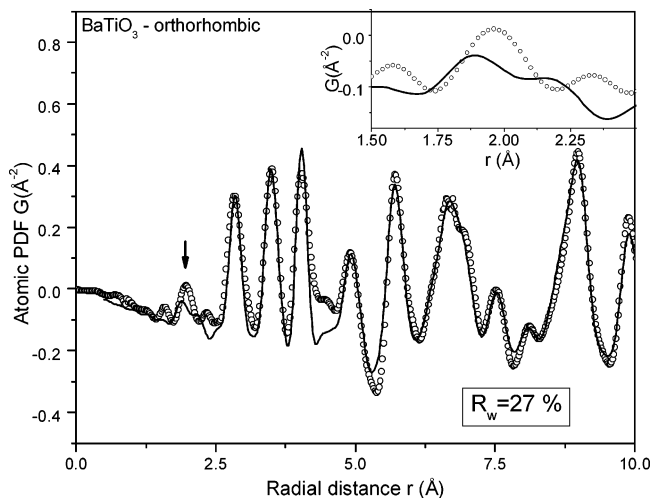


Figure 8. Experimental (symbols) and model (solid line) PDFs for $BaTiO_3$. The model PDF is based on the orthorhombic-type structure shown in Figure 1c. The reliability factor R_w is reported in the lower part of the figure. An arrow marks the position of the first PDF peak where the model and experimental data show a strong disagreement. The same peak is given in the inset on an enlarged scale.

(45) Here it may be noted that the agreement factors achieved with the PDF refinements appear somewhat higher when compared to those resulted from the Rietveld refinement of diffraction data in reciprocal space (see Tables 1 and 2). This reflects the fact that an atomic PDF differs from the corresponding XRD pattern and is a quantity much more sensitive to the local atomic ordering in materials. Furthermore, the PDF $G(r)$ is very sensitive to the effects of imperfect data correction and systematic errors. As a result, R_w 's close to 20% are common for PDF refinements even of well-crystallized materials.^{21,23,31} The inherently higher absolute value of the reliability factors resulting from PDF-based refinements does not affect their functional purpose as a residuals quantity that must be minimized to find the best fit and as a quantity allowing differentiation between competing structural models. It may also be noted that when the atomic pair correlation function, $g(r)$, defined as $g(r) = \rho(r)/\rho_0$, is used to guide a refinement of a structural model, the resulting reliability factors R_w are significantly lower than those reported from a refinement based on the corresponding PDF $G(r)$, and very close to the values of the goodness-of-fit indicators reported from Rietveld analyses. We, however, prefer to work with the PDF $G(r)$ and not $g(r)$ since the former scales with the radial distance r (see the multiplicative factor in the definition of $G(r)$; eq 1) and is thus more sensitive to the longer range atomic correlations.

distances of 2.0 Å, and two $Ti-O$ distances of 2.16 Å with the orthorhombic model; three $Ti-O$ distances of 1.87 Å and three $Ti-O$ distances of 2.13 Å with the rhombohedral model) resulting in a split first PDF peak, a feature the experimental data do not show. On the other hand, the model based on the tetragonal-type structure considerably improves the reliability factor (compare the PDF-based R_w values reported in Tables 1 and 2 calculated over the whole range of PDF data from 1 to 28 Å) and better describes the fine features in the experimental PDF data appearing at low- r values, in particular, the intensity distribution of the two subcomponents of the split PDF peak at 10 Å and the position and intensity of the shoulder of the peak at 6.9 Å (see the inset in Figure 7). The shoulder reflects mostly correlations between oxygen atoms from neighboring $Ti-O_6$ octahedra and its pronounced presence in the PDF for $BaTiO_3$ and

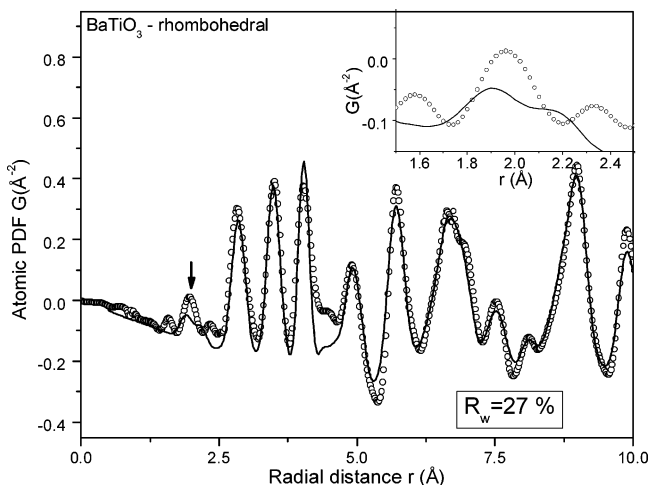


Figure 9. Experimental (symbols) and model (solid line) PDFs for BaTiO_3 . The model PDF is based on the rhombohedral-type structure shown in Figure 1d. The reliability factor R_w is reported in the lower part of the figure. An arrow marks the position of the first PDF peak where the model and experimental data show a strong disagreement. The same peak is given in the inset on an enlarged scale.

almost disappearance in the PDFs for SrTiO_3 and $\text{Ba}_{0.5}\text{Sr}_{0.5}\text{TiO}_3$ (see Figure 3) indicates that those octahedral units are somewhat distorted/rotated in the former material and almost perfectly lined up in the materials containing Sr. The results suggest that the atomic ordering in nanocrystalline BaTiO_3 studied by us is likely to exhibit slight distortions similar to those occurring in bulk tetragonal BaTiO_3 crystal.

The tetragonal structure too features somewhat distorted $\text{Ti}-\text{O}_6$ octahedra (one $\text{Ti}-\text{O}$ distance of approximately 1.9 Å, four $\text{Ti}-\text{O}$ distances of 2.0 Å, and one $\text{Ti}-\text{O}$ distance of 2.15 Å). The first peak in the PDF for nanocrystalline BaTiO_3 , however, is very well reproduced by the tetragonal-based model, indicating that a model featuring slightly distorted $\text{Ti}-\text{O}_6$ octahedra is compatible with the experimental diffraction data. Interestingly, the tetragonal-based model is superior over the cubic one mostly at low- r distances (0–15 Å) as the data in Figure 10a show. It also agrees reasonably well with the PDF data at higher r distances and yields a better overall reliability factor R_w (see Figure 7). A closer look at the behavior of the model data at higher r distances, however, shows (see Figure 10b) that the cubic-based model somewhat outperforms the tetragonal-based one as the corresponding reliability factors R_w (this time calculated over a range of real space distances from 15 to 28 Å) shows. For longer range distances the tetragonal-structure-based model does not reproduce the intensities of the experimental PDF peaks as good as the cubic-type models do and, furthermore, seems to produce a PDF that is not perfectly lined up with the experimental data for distances longer than 24 Å. The fact that the tetragonal-type model is superior over the cubic-type one mostly at distances shorter than 10–15 Å shows that the fine tetragonal distortions in nanocrystalline BaTiO_3 are very likely to be local in nature (up to 10–15 Å) and coexist with a cubic-type arrangement at longer range interatomic distances. The coexistence of a lower symmetry local and a higher symmetry average atomic arrangements is not an unusual picture and has even been observed with perfectly crystalline materials such as In–Ga–As semiconductors for example. These are single-phase

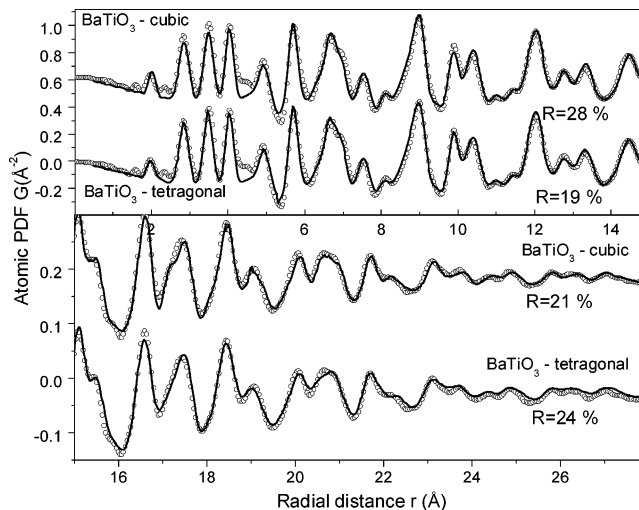


Figure 10. Low r (0–15 Å; upper panel) and higher r part (15–28 Å; lower panel) of the experimental (symbols) and model (solid line) PDFs for BaTiO_3 . The model PDFs are based on the cubic- and tetragonal-type structures shown in Figure 1a and 1b, respectively. The corresponding structural parameters are summarized in Table 1 and Table 2, respectively. The reported in the figure reliability factors R_w are calculated over the corresponding range of distances.

materials possessing a long-range cubic structure and substantially distorted local atomic ordering.²⁹ Nanocrystalline ZrO_2 has also shown a distorted local and cubic-type, longer range atomic structure.³³ Furthermore, recent NMR studies⁴⁶ have suggested that even bulk cubic BaTiO_3 crystal may be viewed as an assembly of a large number of small and randomly oriented “tetragonal” nanosize domains with dynamically elongated unit cells which transform into a phase with macroscopic tetragonal structure only when cooled below 393 K. With nanocrystalline BaTiO_3 such a transformation of the local tetragonal-type distortions into a macroscopic tetragonal-type structure that is thermodynamically stable at room temperature may not occur because of the very limited structural coherence length (~ 2 nm) in the material.

In summary, the results of our structural studies show that nanocrystalline SrTiO_3 and $\text{Ba}_{0.5}\text{Sr}_{0.5}\text{TiO}_3$ possess a structure of a perovskite type exhibiting almost perfect $\text{Ti}-\text{O}_6$ units arranged in a long-range pattern with cubic symmetry. The atomic arrangement in nanocrystalline BaTiO_3 is also of a perovskite type but exhibits slight tetragonal distortions that show up at short-range interatomic distances only.

This new structural information helps one understand the dielectric properties of $\text{Ba}_x\text{Sr}_{1-x}\text{TiO}_3$ ($x = 1, 0.5, 0$) nanoceramics as follows: The longer range cubic (centrosymmetric structures) of SrTiO_3 and $\text{Ba}_{0.5}\text{Sr}_{0.5}\text{TiO}_3$ are incompatible with the appearance of ferroelectricity and the materials do not show spontaneous polarization as experimentally observed.^{12–16} The situation with BaTiO_3 is more complex. The material shows local tetragonal distortions but they seem to be confined to distances as short as 10–15 Å only. As the theoretical estimates of Lines and Glass suggest,⁴⁷ the correlation length between polar units in

(46) Zalar, B.; Lebar, A.; Selinger, J.; Blinc, R. *Phys. Rev. B* **2005**, *71*, 064107.

(47) Lines, M. E.; Glass, A. M. In *Principles and Applications of Ferroelectrics and Related Materials*; Clarendon: Oxford, 1977.

ferroelectric materials are of the order of at least 10 and 2 nm in directions parallel and perpendicular to the polarization vector, respectively. With nanocrystalline $BaTiO_3$ the polar units (slightly distorted/rotated $Ti-O_6$ octahedra) are correlated over distances of about 1.5 nm only and may not become a driving force strong enough to transform the longer range structure into an asymmetric (tetragonal) one even at room temperature. As a result, the material does not show macroscopic spontaneous polarization as observed in practice.¹²⁻¹⁶

5. Conclusions

The atomic arrangement in nanocrystalline $Ba_xSr_{1-x}TiO_3$ ($x = 1, 0.5, 0$) has been studied by synchrotron radiation scattering experiments and Rietveld and atomic PDF techniques. The materials have been found to possess an atomic arrangement well-defined over 2–2.5 nm distances and resembling the one occurring in the crystalline perovskites. Although the structural coherence length in the nanostructured materials is greatly reduced, their structure still may be described in terms of a repetitive unit cell containing only a few atoms as the data summarized in Tables 1 and 2 show. $SrTiO_3$ and $Ba_{0.5}Sr_{0.5}TiO_3$ possess an atomic arrangement that

is cubic type at both short and longer range interatomic distances. The local symmetry with nanocrystalline $BaTiO_3$ is tetragonal but the slight tetragonal distortions seem to average out and the structure of the material is better described in terms of a cubic-like ordering at longer range distances. That is presumably the reason nanocrystalline $BaTiO_3$, similarly to $SrTiO_3$ and $Ba_{0.5}Sr_{0.5}TiO_3$, does not show spontaneous polarization at room temperature.

This study is another demonstration of the ability of the PDF technique to yield three-dimensional structural information for materials of limited structural coherence, including nanocrystalline materials. The technique succeeds because it relies on total scattering data obtained from the material and, as a result, is sensitive to its essential structural features regardless of crystalline periodicity and size.

Acknowledgment. Thanks are due to M. Beno from APS, Argonne National Laboratory, for the help with the synchrotron experiments. The work was supported by NSF through grant DMR 0304391(NIRT). The Advanced Photon Source is supported by DOE under Contract W-31-109-Eng-38.

CM052145G